Ultra-high-resolution small-animal SPECT imaging

Frans van der Have

Colophon

This book was typeset in LaTeX 2_ε by the author.

The printing of this thesis was financially supported by MILabs B.V., Utrecht.

Cover image: B. Vastenhouw
Print: Gildeprint, Enschede
ISBN: 978-90-3934698-3

Ultra-high-resolution small-animal SPECT imaging

SPECT-beeldvorming met ultrahoge resolutie bij kleine dieren

(met een samenvatting in het Nederlands)

Proefschrift

ter verkrijging van de graad van doctor aan de Universiteit Utrecht op gezag van de rector magnificus, prof.dr. J.C. Stoof, ingevolge het besluit van het college voor promoties in het openbaar te verdedigen op donderdag 22 november 2007 des middags te 4.15 uur

door

Frans van der Have

geboren op 13 december 1977 te Ede

Promotores:

prof.dr. F.J. Beekman

prof.dr.ir. M.A. Viergever

Het onderzoek werd mede mogelijk gemaakt met de financiële steun van de Nederlandse Organisatie voor Wetenschappelijk Onderzoek (NWO) (project 917.036.335).

Contents

Chapter 1

Introduction and thesis outline

Single Photon Emission Computed Tomography (SPECT) is the most applied clinical imaging technique to image functions of organs and tissues *in vivo* with the aid of tracer molecules. Imaging with tracer molecules offers the possibility to characterize functional and pathological properties of tissue in living beings with a higher sensitivity than other imaging techniques such as X-ray Computed Tomography (CT) and Magnetic Resonance Imaging (MRI). Molecular imaging with SPECT in small animals such as mice and rats is of tremendous importance for drug discovery, the unraveling of molecular aspects of disease and the development of new tracer molecules for clinical SPECT. The development of a dedicated ultra-high-resolution SPECT imaging system for small laboratory animals, and especially its instrumentation and image reconstruction, is the main subject of this thesis.

Before a SPECT scan can be performed, radioactively labeled molecules emitting gamma photons are introduced into the patient or animal under investigation. Due to the extremely high energy of gamma photons (compared to visible light photons) they can be detected outside the body with a special camera (gamma camera). A gamma camera consists of a position-sensitive detector for gamma photons and a collimator that has a function that is similar to that of a lens used in an optical camera, namely to form an image of the object. The collimator of choice used in small-animal SPECT is the pinhole collimator that is based on the same principle as the pinhole in early optical cameras (*i.e.* camera obscura). From a number of gamma-camera images ("projections") obtained at different angles around the object a 3D volume image can be reconstructed that represents the 3D concentration distribution of radioactive molecules in the body. Slices of the volume image can be viewed and are often called tomographic images (the Greek word *tomos* means slice). In the next chapter the basics of pinhole SPECT instrumentation and reconstruction are explained and put into perspective

with respect to past, present, and future clinical and pre-clinical pinhole SPECT applications in biomedicine.

The ability to map molecular tracer distributions with very low concentrations distinguishes SPECT — and also Positron Emission Tomography (PET) — from other clinical imaging modalities such as CT, MRI and Ultrasound. Since different imaging modalities are complementary it is often beneficial to combine them. For example, a tumor detected in a SPECT scan may lack sufficient anatomical reference, but a spatially registered CT or MRI allows an exact localization of the tumor in an anatomical/molecular overlay image. One of the reasons that SPECT and PET are currently the clinical molecular imaging modalities of choice is that they are able to image tiny amounts of tracers, often with a concentration that is 10^6 times lower than has been imaged with MRI. In this way the tracer principle (G. de Hevesy: a radioactive isotope behaves chemically the same as a stable isotope of the same element) can be exploited; it allows biological pathways to be investigated using amounts of tracer substance small enough to not disturb the system under study.

A novel pinhole SPECT system called U-SPECT was developed for imaging small animals. This thesis is associated with the development and initial applications of U-SPECT. The first chapters cover physical and design aspects, and chapters 7 and 8 are about the first and second generation U-SPECT systems as a whole. Like most other small-animal SPECT devices, U-SPECT systems use pinhole collimation. However, U-SPECT systems have a higher number of pinholes and a more strongly focused geometry. The high number of pinholes allows U-SPECT to be stationary, *i.e.*, U-SPECT does not require rotation of the collimator or detectors with respect to the animal for sufficient angular sampling, unlike other systems. Other distinguishing features of U-SPECT are that the projections on the detector from different pinholes are made non-overlapping and are obtained with high magnification to achieve a high image resolution.

Chapter 2 serves as a primer to pinhole SPECT. It contains a historical perspective to pinhole radio-nuclide imaging. Different methods of image reconstruction are explained, including statistical algorithms like those used with the U-SPECT systems. A discussion of the possible use of pinhole collimation in clinical SPECT-imaging, and a design of a pinhole-based human cardiac scanner is presented.

In imaging gamma radiation, the radiation will not be completely stopped by the material that forms the collimator, *i.e.* the material surrounding the pinhole aperture in pinhole SPECT. The radiation will not only pass through the hole, but also through the edge surrounding it (edge penetration). Gamma photons can also scatter within this material, and this can result in one or more photons emerging with a direction and energy which differ from that of the original incoming photon. Both edge penetration and scatter degrade the quality of the image,

since they add uncertainty to the direction from which photons originate. When the project to build the first U-SPECT system was started, it was not known to what extent penetration and scatter would affect the projection images, since the designs assumed a larger number of pinholes with a smaller diameter than had been used in any other system before. Because one can expect more penetration and scatter effects if the pinhole diameter is made smaller, simulation studies were performed that are presented in chapters 3 and 4.

An important part of the design of a small-animal SPECT system is the imaging geometry: how many pinholes will be used, and what is their placement with respect to the animal and the detector. It is not straight forward to create an "optimal" system, since there are many parameters that need to be considered, and most, if not all, are interrelated. Chapter 5 presents a mathematical model that can be used to quickly compare the projected performance in terms of resolution or sensitivity (the fraction of emitted photons that can be detected) of systems with varying design parameters.

The image reconstruction software of U-SPECT is based on iterative statistical algorithms. Apart from the data from the detector, these algorithms require a so-called "system matrix". That system matrix describes the detector response, *i.e.*, what the measured image on a detector would look like given a distribution of radio-active tracer in the animal. Chapter 6 presents a method that was developed to obtain the system matrix, and it shows the influence of changing certain parameters in the creation of the system matrix on the resulting reconstructed images.

The first prototype small-animal SPECT system that was built in Utrecht was called U-SPECT-I. It used a clinical 3-headed SPECT system as its detector. After removal of the clinical collimators, a frame with a cylindrical pinhole collimator tube, various shielding parts, as well as an xyz robotic stage, were mounted onto the SPECT system. This temporarily transformed the clinical system into the hardware part of U-SPECT-I. Chapter 7 presents U-SPECT-I as a complete system. The performance in terms of achievable resolution and sensitivity is characterized by means of phantom experiments. The chapter also includes results from measurements with mice.

A next generation system was designed and developed, called U-SPECT-II. U-SPECT-II can be used for imaging of both mice and rats. It has a significantly larger detector surface than U-SPECT-I and its detectors have fully digital electronics. The data is read out in list mode, which provides more flexibility in choosing energy windows and doing multi-isotope imaging, and allows to do gated imaging. Furthermore it has an automated method to expand the field-of-view up to total body imaging using a specially designed graphical user interface. The design, development, initial measurements to characterize the performance, and a demonstration of some of its capabilities are described in chapter 8.

In conclusion, this thesis describes the development and initial deployment of U-SPECT. On the physical aspects of multi-pinhole SPECT, the foundation is laid for a series of high-resolution U-SPECT systems. The capabilities of the first two of these have been demonstrated and promising first studies in animals have been conducted. The U-SPECT systems can now start to be used for answering biological questions and will hopefully contribute to progress in molecular imaging.

Chapter 2

The pinhole: gateway to ultra-high-resolution three-dimensional radionuclide imaging

F J Beekman and F van der Have
Eur J Nucl Med Mol Imaging 2007; 34(2): 151–161.

Abstract

Today the majority of clinical molecular imaging procedures are carried out with single photon emitters and gamma cameras, in planar mode and Single Photon Emission Computed Tomography (SPECT) mode. Thanks to the development of advanced multi-pinhole collimation technologies, SPECT imaging of small experimental animals is rapidly gaining in popularity. Whereas resolutions in routine clinical SPECT are typically larger than one cm (corresponding to $>$1000 μl), it has recently proved possible to obtain spatial resolutions of about 0.35 mm ($\approx$ 0.04 μl) in the mouse. Meanwhile, SPECT systems that promise an even better performance are under construction. The new systems are able to monitor functions in even smaller structures of the mouse than was possible with dedicated small-animal Positron Emission Tomography ($\approx$ 1 mm resolution corresponding to one μl). This paper provides a

brief history of image formation with pinholes and explains the principles of pinhole imaging, pinhole tomography and the basics of modern image reconstruction methods required for such systems. Some recently introduced ultra-high resolution small animal SPECT instruments will be discussed and new avenues for improving system performance will be explored. This may lead to many completely new biomedical applications. We also demonstrate that clinical SPECT systems with focusing pinhole gamma cameras will be able to produce images with a resolution that may become superior to that of PET for major clinical applications. A design study of a cardiac pinhole SPECT system indicates that the heart can be imaged an order of magnitude faster or with much more detail than is possible with currently used parallel hole SPECT (e.g., 3–4 mm instead of $\approx$ 8 mm system resolution).

2.1 Introduction

Today, the majority of clinical procedures using tracers to visualize specific tissue binding sites are carried out with planar gamma-camera imaging, Single Photon Emission Computed Tomography (SPECT) and Positron Emission Tomography (PET). Imaging of single-photon emitting radio-pharmaceuticals with gamma cameras, in planar or SPECT mode, makes up the largest fraction of these molecular imaging procedures. In addition to clinical SPECT, SPECT imaging with pinholes of experimental animals is currently growing rapidly. The main reason for this is that it allows for both the visualisation and the accurate quantification of molecule concentrations in small animals like rodents with resolutions down to subcompartments of mouse organs. This impacts most pre-clinical imaging procedures since rats and mice form the largest part of the experimental animal population. The spatial resolution and signal strength of pinhole-collimated gamma cameras are often superior compared to these features with other types of SPECT collimation. The combination of multiple focusing pinhole collimators and advanced software provides even higher resolutions than can be obtained with dedicated small animal PET for many rodent imaging procedures: some novel SPECT systems produce images even at sub-half-mm scales. The growing number of experimental small animal models of human physiology and disease will benefit from this development because they require very accurate and non-invasive longitudinal monitoring of molecule dynamics.

Many SPECT tracers are now commercially available that have sufficiently long half-life times to allow for long-distance transportation. Therefore no expensive infrastructure with cyclotrons is required. At least eight companies are already manufacturing small animal SPECT devices, with a wide range of pricing and system performance. Many biomedical research institutes will be equipped with pinhole SPECT in the near future. As a result, non-

invasive first line screening for experimental drugs with radiotracers is expected to become extremely popular.

A primer on the physics of small animal radionuclide imaging (PET and SPECT) was published by King et al. [1], and two overviews of small animal SPECT systems and their place in the matrix of molecular imaging modalities (PET, Fluorescence, Bioluminescence, Magnetic Resonance Imaging and Magnetic Resonance Spectrometry) were published recently by Meikle et al.[2,3]. The goal of the present paper is to acquaint a broad readership with the history, physics and mathematics of pinhole SPECT. In addition, we will attempt to place modern pinhole SPECT in the perspective of past and future SPECT instrumentation and its biomedical applications.

2.2 A brief history of pinhole imaging

Since photons travel in straight lines, an inverted image of the illuminated field-of-view is produced when passing through a pinhole. The size of the projected image depends on the relative distance between object and pinhole versus pinhole and the surface where the image is projected. This natural phenomenon of pinhole image formation predates the existence of man: For hundreds of millions of years living creatures have existed that are able to see or sense through holes located in front of a layer of photo-sensitive tissue such as a retina. A contemporary animal with pinhole eyes is the "living fossil" *Nautilus Pompilius* (figure 2.1): it has existed in seas and oceans for about one hundred million years. Another example is the Giant Clam which has multiple-pinhole eyes, see [4].

We will never know when and how humans first devised pinhole imaging but situations may have occurred where sun-illuminated scenes were projected upside down through a hole onto the opposite wall of a cave (figure 2.2a). The resulting "movies" may well have astonished primitive man, possibly as long as hundreds of thousands of years ago. What is certain is that several hundreds of years ago pinhole "cameras" as large as complete living rooms were exploited by artists, for example by Leonardo da Vinci (1452–1519). Da Vinci, and later on artists like Johannes Vermeer (1632–1675) used pinhole projections on the wall of such a dark room (figure 2.2b), to trace and draw lines that formed the basis for their paintings and enabled them to obtain an almost perfect perspective. Such devices and their successors are often called "Camera Obscura" (Dark Chamber) a term which, according to some historians, was first used by the astronomer Johannes Kepler. Much later, Joseph Nicéphore Niépce built the first pinhole camera with a storage medium (film!) which produced the first photographs. This occurred about a hundred and eighty years ago [5,6].

In clinical radio-nuclide imaging, the pinhole has served as a means to collimate gamma

rays since the earliest gamma cameras [7–9]. Up till now the pinhole gamma-camera has been used mainly for the imaging of small volumes such as the human thyroid (e.g. [10]). Pinhole imaging involving the use of more than one pinhole simultaneously (multi-pinhole imaging, its nuclear application already described in 1973 [11]) was used to image relatively small organs such as the human thyroid [12], shoulder [13,14], hip [15,16], the neck [17] and the heart [18]. So far however, multi-pinhole imaging has not yet achieved broad clinical application. Nevertheless, it can be said that (multi) pinhole-like imaging was "invented" by nature and through the ages has been re-invented over and over again, which applies to many principles of engineering.

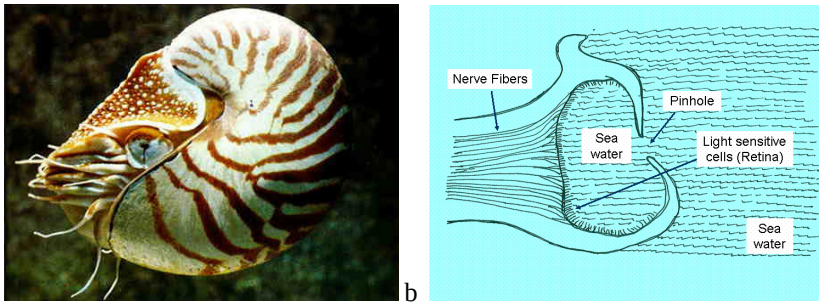

Figure 2.1: The *Nautilus Pompilius* (a, image courtesy of Artis Zoo, Amsterdam) with pinhole eyes (b). In color print in the appendix.

2.3 Principles of planar radio-nuclide pinhole imaging

Pinhole imaging with gamma rays is based on the same geometric principle as the optical pinhole camera. A scintillation crystal is used for determining the gamma ray intensity projection: the scintillation light pattern is read out with a position-sensitive light detector, instead of a film. In optical cameras, pinholes have been replaced by lenses, since this allows for more light photons to be captured. Since there are no practical methods for diffracting or reflecting gamma rays for SPECT, today collimators are used for imaging single-photon emitting radio-nuclides, although these transmit only a tiny fraction of the gamma quanta emitted by tracers in the animal or patient. Most collimators consist of a radiation-absorbing wall with one or more narrow holes. While for animals pinhole collimators are popular, the parallel-hole collimator is the clinical work horse. It consists of a slab of lead with a thickness of a couple of centimetres, with many narrow parallel holes very close to each other (figure

a 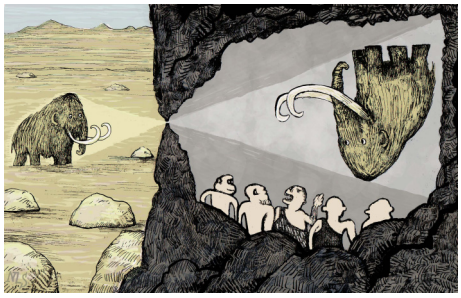 b 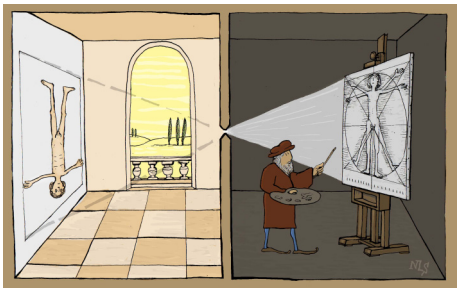

Figure 2.2: a) An artist's impression of possible early pinhole imaging: the film-less movie theatre was born when surrealistic "upside down movies" were displayed on the wall of a cave. b) Was this how Leonardo painted the Vitruvian Man? A trade-off between "patient" discomfort and artist discomfort could be found by changing the angular position of the model. Illustrations by Niels de Hoog. In color print in the appendix.

2.3, left). Today, these collimators are relatively easy to produce, and are suitable for imaging large areas of the body. SPECT images can be reconstructed rapidly and simply from parallel-hole projections.

Why do pinhole collimators produce images with a much higher resolution than parallel-hole collimators when used to image small animals or small organs? And why can this resolution be even better than the amount of blurring due to the detector-properties themselves (already a few mm)? This is explained in figures 2.3 and 2.4. Figure 2.3 shows a mouse of size T that is projected through a parallel-hole collimator (left side) and through a pinhole (right side). In the case of an "ideal" parallel-hole collimator the projection of the object is blurred only by the intrinsic gamma camera resolution. The blurring is caused by (i) scintillation light that spreads out in the crystal, (ii) the limited number of light photons generated per gamma-interaction in the crystal that results in position uncertainty of the detected scintillation light flash, and (iii) the limited positioning abilities of the position-sensitive light detector behind the crystal. The intrinsic camera resolution is characterized by a value R_{i} which describes the width of the blob that appears when a pencil gamma-beam is used to irradiate the crystal. For most clinical gamma cameras R_{i} is about 3.5 mm Full Width of Half Maximum (FWHM). With pinholes we have a different situation: when the distance between the mouse and the pinhole is L and between the pinhole and the detector is $5\times L$, the size of the mouse projection is $5\times T$. Therefore, when the mouse is de-magnified to its original size, it is not smoothed with an amount corresponding to R_{i}, but it is smoothed only with $R_{\mathrm{i}}/5$. The smaller the object, the closer it can be placed to the pinhole without protruding out of the field-of-view,

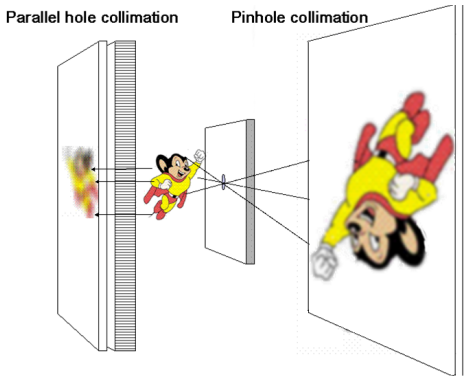

Figure 2.3: With parallel hole collimation (*left*) image resolution can be degraded significantly due to intrinsic camera blurring. With pinhole imaging (*right side of the mouse*), magnification of the projection suppresses information loss that is due to intrinsic camera blurring. In color print in the appendix.

and therefore the higher the magnification factor and the resolution can be. A pleasant side effect of using pinholes for small animals is that the fraction of detected photons (the so called sensitivity, here denoted by S) in the field-of-view increases spectacularly when the object is closer to the pinhole. This is because the solid angle at which photons from each point in the object are able to pass through the pinhole increases tremendously for points closer to the pinhole. This relationship can be approximated by $S = D_{\text{eff}}^2/(16z^2)$where D_{eff} is the effective hole diameter (accounting for penetration of rays through the aperture edges) and z the object-to-pinhole distance. With parallel holes the fraction of detected photons from a small source in air is almost independent of the camera distance. Experimental data acquired at Duke University (figure 2.4, from [19]) clearly demonstrate this effect: both sensitivity and resolution obtained with pinholes beat those of a parallel-hole collimator when the object is close to the pinhole opening. Extreme exploitation of this magnification and sensitivity-increasing effect is shown during imaging of the tiny thyroid of a mouse (figure 2.5); despite the fact that R_{i} of the camera was 3.1 mm for this particular example, details such as the parathyroid glands could still be visualized.

The resolution of a pinhole system for an "ideal" detector (with $R_{\text{i}} = 0$) is described in equation 2.1, and is also called the geometric resolution R_{g} of the pinhole device:

$$R_{\text{g}} \approx D(l+z)/l \tag{2.1}$$

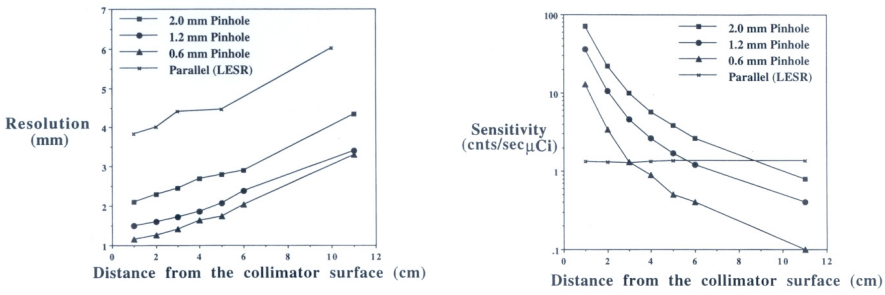

Figure 2.4: Advantages of a pinhole system over parallel-hole collimation. When an object is imaged from a short distance, a better image resolution can be obtained, and at the same time the detected fraction of photons (sensitivity) can be much higher (Source: R.J. Jaszczak et al. [19], with permission of *Physics in Medicine and Biology*).

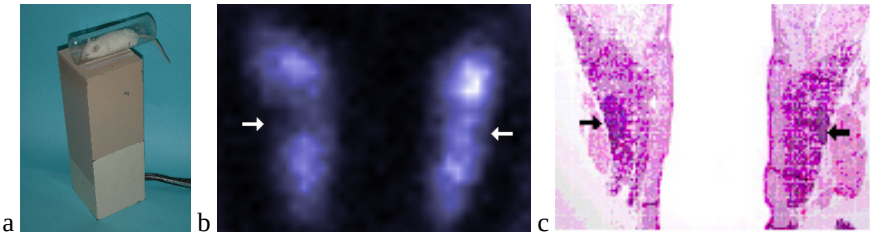

Figure 2.5: a) Desktop mouse pinhole imaging system. b) I-125 scan of a mouse thyroid provides details of a few hundred micrometers such as the parathyroid gland which does not take up any iodine (arrows, also shown in frame c). From [20]. In color print in the appendix.

Here, l is the distance between the pinhole and the detector. This equation shows that the effect of the pinhole diameter dramatically affects the resolution, particularly when pinhole-to-object distance increases. The effects of a limited detector resolution are taken into account in equation 2.2. Here the total system resolution R_{t} is approximated by:

$$R_{\mathrm{t}} \approx \sqrt{(\frac{z}{l}R_{\mathrm{i}})^2 + R_{\mathrm{g}}^2} \tag{2.2}$$

Equation 2 shows that limited intrinsic resolution can degrade the total system resolution dramatically. Note that penetration of rays along the pinhole edge can be accounted for by using effective diameters rather than physical diameters. Accurate mathematical descriptions of effective hole diameters, both in terms of resolution or sensitivity can be found in [21] and [22].

2.4 Pinhole SPECT devices and image reconstruction.

With the development of advanced algorithms that are currently available to reconstruct images from complex pinhole geometries, images of superior resolution and quantitative accuracy can be produced. Consequently almost all dedicated small animal SPECT systems are presently fitted with pinholes. Usually one rotates either the animal or the detectors with collimators to acquire a sufficient number of angular views ("projections") to enable reconstruction of 3D volume images. SPECT systems can be fitted with one [e.g.,23-25], two [e.g., 26], three [e.g. 19,27], four [28], six [e.g. 29], or even more pinholes. In some cases the use of many pinholes will produce overlapping projections (often referred to as multiplexed projections) [30,31]. In addition to rotation-based systems, there are stationary systems: these often have many pinholes and are able to deliver excellent spatial and temporal resolution. Two types of stationary systems with many non-overlapping projections will be discussed in a following section.

The issue of overlapping versus non-overlapping projections is food for many scientific discussions and ongoing research. Overlap increases system sensitivity but one has too keep in mind that this increase is at least partly artificial, since a significant amount of information per photon can be lost due to the overlap. Therefore, sensitivity of systems based on overlapping projections cannot be compared to systems with non-overlapping projections. The comparison is complicated since information loss due to overlap strongly depends on the distribution that is imaged. For example, the image degradation gets stronger with higher background activity and with extended tracer distributions. The latter are much more common than distributions of tracers that accumulate in small areas. In some cases overlapping

projections can be used to increase the field-of-view. In addition, allowing overlap is a way to increase the number of viewing angles of a volume of interest. Research on the extent, if any, to which overlap is beneficial for specific tasks and distributions is ongoing in several imaging laboratories.

In principle, image reconstruction from pinhole SPECT projection images can be performed analytically, using filtered back-projection-like algorithms (e.g. the Feldkamp algorithm [32]). These algorithms are also used in other cone-like radiation-transport geometries such as X-ray CT systems and cone-beam collimated SPECT systems (cone-beam collimators, just like parallel-hole collimators, have long holes but these holes are directed to a focal point). The advantage of these analytical methods is their computational speed, but (i) they have limited robustness to quantum noise that is present in projections, (ii) they do not compensate for image blurring effects and (iii) they are not really flexible enough to handle the complicated pinhole and detector placements needed to extract the maximum amount of information from the object being imaged. Therefore, at present with most pinhole systems iterative methods of reconstruction are used, such as the Maximum Likelihood Expectation Maximization (ML-EM, [33]). The ML-EM algorithm is a statistical algorithm which takes into account the characteristics of the noise in gamma camera pixels. In addition, these algorithms can incorporate models of image degradation such as non-uniformities, and distance dependent sensitivity. Other factors, such as spatial variant resolution and radiation penetration along the pinhole edges can also be included [30,34,35] in order to correct for these image degrading effects. As a result statistical algorithms produce images with less noise, better resolution and higher quantitative accuracy than many other algorithms.

2.5 A simple explanation of image reconstruction

Although sometimes complicated to implement in a real pinhole system, the basics of iterative reconstruction can be explained quite simply to those who remember simple high school algebra. The task in iterative reconstruction in emission tomography is to attempt to solve a linear set of hundreds of thousands equations with typically hundreds of thousands of unknowns. Such a set of equations is shown in figure 2.6a: the unknown numbers A_i (together forming a so called "vector" **A**, with element indexes i ranging from 1 to V) are the amounts of radioactive tracer present in each tiny volume element (voxel) within the object. The process of '*iterative reconstruction*' involves the repeated application of a set of operations that progressively gets closer to a correct estimate of the unknown activity distribution. Figure 2.6b shows the concept of this iterative updating. At the end of a reconstruction each of the estimated numbers can be transformed to colour- or grey-scale pixels for visualization.

Before the iterative calculations can start one needs a set of numbers (matrix elements) in which each of the elements M_{ji} represents a probability that gamma-quanta emitted by an amount of tracer A_i present in a voxel i will be detected in a pixel j at one of the detectors. These elements need to be known for each individual voxel-pixel combination. The entire set of measured projection pixels is represented by a vector **P**. The numbers M_{ji} together with **P** determine the set of equations from which the activity distribution **A** has to be solved. For example, during an iteration of the ML-EM algorithm, the actual estimate of **A** (which we call $\mathbf{A}^{e}$) is used to generate an estimate of the projection, denoted with vector $\mathbf{P}^{e}$, simply by carrying out the summations, like presented in figure 2.7a, but with $\mathbf{A}^{e}$ instead of **A**. Next, ML-EM uses the relative differences between **P** and $\mathbf{P}^{e}$, to calculate an object error map. The error map is used to update $\mathbf{A}^{e}$ with a simple equation. The basic idea behind all iterative methods is that when $\mathbf{P}^{e}$ is very close to **P**, $\mathbf{A}^{e}$ must be close to the reality **A** because it produces almost the same projection as does **A**. The generation of a new $\mathbf{P}^{e}$ and the updating of $\mathbf{A}^{e}$ often need to be repeated hundreds of times to obtain a good solution. Because of the many iterations required, acceleration methods to speed up the algorithms have been developed. The Ordered Subset Expectation Maximization (OS-EM, [36]) is currently the most popular method.

Simple introductions to the subject of iterative SPECT image reconstruction, and information on how to carry out comparisons and update steps during reconstruction, can be found in [37,38]. The accurate determination of the matrix elements of M is difficult, often requiring complex calculations and/or measurements that are specific to each different pinhole SPECT device. An accurate match of the matrix elements and real detection probabilities has a critically important influence on the reconstructed image; the number of iterations and quality of image smoothing for noise suppression are also important.

2.6 Stationary SPECT systems

Some pinhole systems require rotation of either the detector or the animal, others are stationary pinhole systems. Early clinical stationary pinhole systems were developed and clinically tested in the 1970's by Wouters et al.[11], Chang et al.[12] and Vogel et al.[18]. The systems in [11] and [18] were based on only seven pinholes. Various shapes of apertures other than pinholes, some of which were time coded, were also investigated at that time, see [39]. Later, several papers about exciting stationary pinhole SPECT system designs were published by the University of Arizona [e.g. 40]. In addition a modular stationary SPECT device was tested and presented in 1993 [41]. Later on systems with 24 pinholes (FastSPECT I) and 16 pinholes (FastSPECT II) were constructed [e.g. 42,43]. Resolutions better than 2 mm

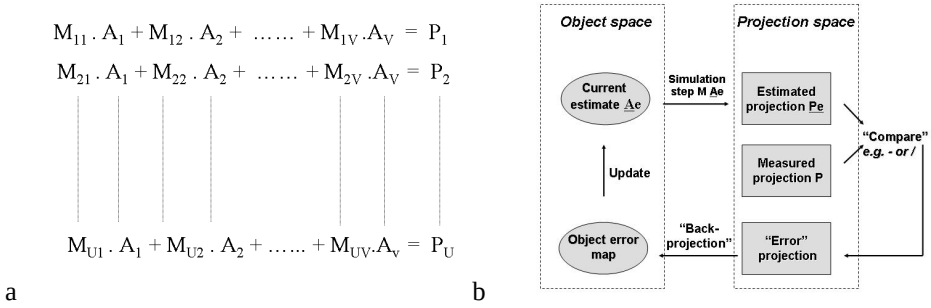

Figure 2.6: Frame a: Set of linear equations describing how activity in the object is mapped onto the projection images. This set is used in iterative methods to obtain the reconstructed volume image (with a total of V different elements of vector A) from the pinhole camera projection pixel contents **P** with a total of U pixels. U and V are numbers in the order of a couple of hundreds of thousands. The iterative scheme is shown in frame b.

were reported already in 1998 with FastSPECT [44]. As resolution improved over the years, FastSPECT produced impressive myocardial images of rats [45] and was also used for other biological studies.

An advantage of stationary SPECT systems is that they can perform arbitrarily short data acquisitions that contain all the viewing angles required to reconstruct a tomographic image, which is similar to the situation in most PET systems. Because of the high number of pinholes that provide a high sensitivity, stationary systems are ideal for dynamic imaging and assessing tracer and pharmaceutical kinetics. In addition these stationary systems are inherently very stable over time.

In 2004 the University Medical Centre Utrecht completed the construction of a stationary ultra-high resolution system (U-SPECT-I [35]). A tube with 75 focussed gold pinholes was put inside a set of three detectors borrowed from a clinical system. A robot was used for calibration and for total body imaging protocols. An improved stand alone version ("U-SPECT-II", figure 2.7) was recently launched based on three large field-of-view detectors that allow for an even better sensitivity and resolution than U-SPECT-I. Prototypes of future U-SPECT devices with CCD-based detectors are currently under development (e.g. the U-SPECT-III, [46]). In all U-SPECT systems the animal is surrounded by many pinholes placed in rings. This large set of pinholes allows us to obtain a sufficient number of different angular views for reconstructing cross-sectional images of the object, without having to change the position of the detectors, the pinholes, or the animal. We used U-SPECT-I to scan the first liv-

ing animals in the spring of 2004, and immediately obtained images with sub-mm resolution: 0.45 mm along all axes could be achieved with 0.6 mm pinholes, and currently, with pinholes of 0.3 mm a resolution of 0.35 mm (0.04 micro-litre) has been achieved ([35,47], figure 2.8). U-SPECT-I is equipped with a large number of pinholes, namely 75, and also differs in several other respects from FastSPECT: in U-SPECT the pinholes are much more focussed as a result of a novel two-stage collimation method that prevents projection overlap and allows for close packing of projections on the detector surface. Furthermore, the geometry chosen uses three large detectors and results in a high magnification factor which helps to improve resolution. Instead of using relatively expensive modular gamma cameras that contain a large amount of dead area at the edges, our system creates separated but closely packed projections on large-area detectors. The large number of independent pinhole cameras created in this way facilitates the detection of a large number of gamma quanta from the volume that one really wants to scan (e.g. the heart or brain); as a result hardly any detector area is wasted by projecting irrelevant parts of the animal. We have also found that it is very easy to image large volumes with U-SPECT, up to entire animals. For example, using the same focussing collimator we were able to obtain total body scans of mice at approx. 0.5 mm resolution [48]. To this end the bed can be shifted in x,y, and z direction, in order to acquire gamma-radiation from an arbitrarily large part of the animal.

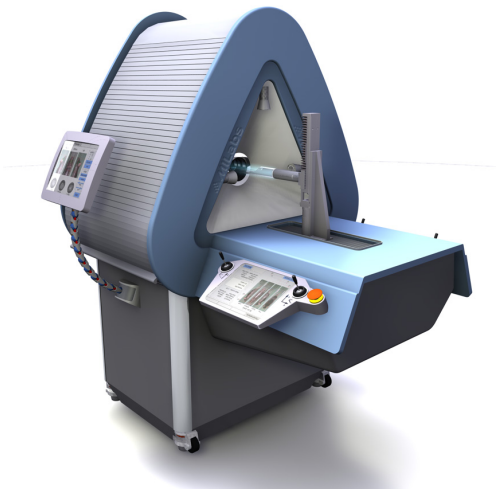

Figure 2.7: The U-SPECT-II system based on ultra-large NaI detectors and interchangeable collimator tubes. In color print in the appendix.

a 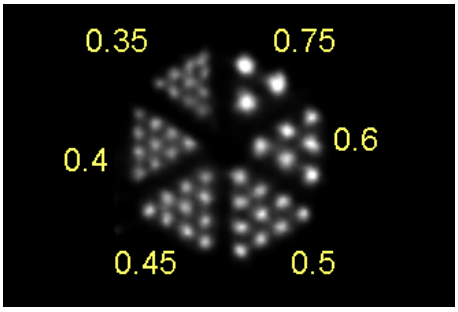

b 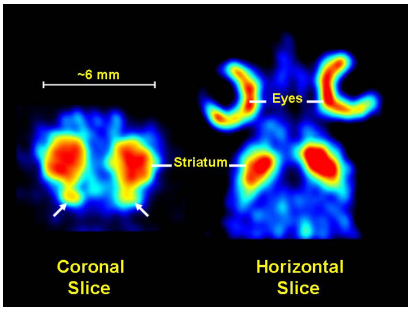

Figure 2.8: U-SPECT images; Frame a) Derenzo resolution phantom image obtained with U-SPECT (0.3 mm pinholes) shows a section with 0.35 mm capillaries clearly separated. Frame b) Two mutual perpendicular cross-sections of a 3D sub-mm resolution FP-CIT image of the distribution of dopamine transporters in a mouse head obtained with U-SPECT-I fitted with 0.6 mm pinholes. Dynamics of tracer concentrations in tiny structures in sub-compartments of mouse organs such as the Olfactory Tubercle (arrows) and the retina can be monitored. In color print in the appendix.

2.7 Further improvement of small animal SPECT instruments

There are several ways to improve imaging characteristics of small animal SPECT devices. These include the development of better algorithms and software for image reconstruction, optimised collimators and better detectors. Some systems are already equipped with close to optimal image reconstruction methods which perform accurate resolution recovery and which result in good quantitative accuracy. In these systems the match between the calculated/measured reconstruction matrix elements and the physical detection likelihoods has to be very accurate and sufficiently stable over time. Therefore, one needs very good system calibration which can be carried out with point source measurements. Much important information about pinhole SPECT reconstruction and the associated estimation of the matrix elements has already been published [e.g. 21,35,47,49–52]

Mathematical investigations are in progress to improve pinhole system geometries [e.g., 53,54]. These investigations can be highly complex due to the many degrees of freedom in system geometry. Candidates for future systems include systems that have a huge number of tiny pinholes; in some designs pinholes with a diameter of close to zero, and therefore transmission of gamma quanta is mainly based on material penetration effects [53].

The position-sensitive gamma ray detector of a SPECT pinhole camera module is in many respects like the retina of the eye since, for example, its quality strongly influences overall system performance. If possible, the detector should have such a high resolution that the system resolution is not affected much by detector blur, but this is not the case yet for any commercial pinhole SPECT system. So far, high resolution detectors have been used only in mini-scale toy systems. The development of affordable high resolution radiation detectors is very important to improve SPECT systems, and also for other biomedical applications. Many successful attempts have been made to manufacture high resolution detectors [e.g., 55–66]. However, these are almost all at the prototype stage, to some extent due to the high costs of obtaining a surface area large enough to serve a large number of pinholes. Efforts are being made to simulate and construct compact high-resolution systems based on CCD's or other detectors [41,46,49,67–70].

For gamma-quanta that travel along exactly the same line towards the detector interaction can take place at different depths in the detector material (e.g. the scintillation crystal). Gamma-detectors as currently in use for pinhole SPECT will attribute these gamma rays to a different ray direction, which will result in parallax errors and therefore in a blurred reconstruction. This is called the depth-of-interaction (DOI) problem. An ideal gamma camera should have high resolution not only for radiation that enters the detector from a direction perpendicular to the detector surface but also for gamma rays that enter the crystal at any angle. So ideally a ray entering a crystal at a certain point and at a certain angle should always provide the same 2D coordinate, independent of the depth at which the interaction in the crystal occurred. One way to achieve this is to use a thin crystal, but then only a small fraction of gamma-quanta can be detected. Another method is to use a curved detector surface like those present in biological systems, but these can be hard to produce. With scintillation detectors it is also possible to use optical techniques to avoid the DOI problem (e.g. [46,49,71]), or to use depth encoding methods in order to derive the exact point at which the gamma ray entered the crystal surface. Also, direct conversion detectors (which are not based on scintillation but convert gamma rays directly into an electrical signal) have been proposed that allow DOI to be corrected by using a 3D read out [57].

As an alternative to pinholes, collimators based on slits have been proposed for small animal SPECT. Some have a single-stage slit collimation [72] followed by collimation with a stack of slats. A drawback of such a slit collimation is that magnification effect that has been shown to be very beneficial to pinhole imaging is only present in the trans-axial direction, which leads to a poor image resolution in the axial direction. The slats effectively result in parallel-hole collimation including its associated blurring effects in the axial direction. As an alternative Huang and Zeng from Utah recently proposed two-stage slit collimation with

crossed slits, where each crossing of two perpendicular slits forms a kind of generalized pinhole collimator [73]. The system with crossed slits can have adjustable sensitivity and independent magnification factors in different directions, and could form the basis of a flexible high-resolution system.

Collimators only allow the detection of photons that have travelled in narrowly selected directions towards the detector, and therefore only a small fraction of all gamma rays can be used with collimated systems. This is a major drawback of SPECT compared to PET. If SPECT evolves along similar directions as eyes have evolved, pinholes will no longer be required. Indeed, some developments are directed towards the replacement of collimators. For example, lens-based systems [e.g.,74,75] and gamma ray mirrors [76-78] have been proposed. However, it remains to be seen whether gamma-lens or gamma-mirror based gamma cameras will ever be able to compete with collimation-based systems, because there are many complications. For example, the space required for a gamma lens is currently of the order of several meters [75] which will be generally too large for practical purposes. An overview of alternatives to collimators is given in [34].

2.8 Some applications of ultra-high resolution SPECT

Major tools for unravelling the function of genes and identifying physiological and pathophysiological mechanisms underlying diseases currently include mouse models and a variety of evaluation methods, including histological/biochemical techniques. Standard histology, immuno-protein staining, *in-situ* hybridisation, and autoradiography techniques can all be used to show the spatial distribution of tissue, cells, proteins or mRNA. However, these methods are extremely laborious and carry the methodological risk associated with working *ex vivo*. As a result the current practice of phenotyping mouse strains is quite limited. In addition, there is a strong societal pressure to refine first line screening of experimental drugs, thereby reducing animal discomfort and the required number of animals used. High-resolution animal SPECT will be a good alternative for part of this work, particularly when these systems become more affordable. SPECT and other molecular imaging devices are causing a revolution in fast functional analysis of mouse models since they enable one to look inside a living animal, and facilitate dynamic and follow-up studies. Moreover a tremendous acceleration and refinement in the testing of experimental drugs can be expected. SPECT may also become more and more important as a pre-selection tool for timing of *ex vivo* methods such as autoradiography. In addition, the dynamic capabilities of new SPECT devices indicate that dynamic and kinetic pharmacologic studies may become an important new application area of SPECT. Furthermore, tools are under development that will enable us to

perform emission tomography on freely moving animals instead of anesthetized animals [e.g. 79]. This will provide unique and new opportunities, particularly with regard to the study of brain function and will facilitate continuous monitoring of molecule distributions *in vivo*.

2.9 High-resolution pinhole SPECT for clinical imaging

The recent introduction of ultra-high resolution pinhole SPECT systems for animals has raised the question of whether it may soon be possible to develop very high resolution clinical pinhole systems for important application areas such as heart or brain imaging. As mentioned in the course of this paper, pinholes have been used for clinical radio-nuclide imaging for many years, including the imaging of small organs like the thyroid, but they are still used in only a small fraction of all SPECT procedures. So far it seems that the advantages of pinholes are smaller when large body areas have to be imaged and when one is confined to scintillation gamma cameras with 3- to 4-mm intrinsic resolution. On the other hand, if one can focus enough pinholes on the organ of interest, the distance related sensitivity drop that hampers non-focussing pinhole designs can be prevented. In addition, a stationary pinhole set-up can be created with focussing pinholes which can be advantageous for dynamic cardiac imaging. Figure 2.9 shows an artist's impression of a focusing cardiac pinhole "toy model" that will be analysed below. This C-shaped detector set-up consists of five large detector blocks that each consist of three standard gamma cameras (R_{i}=3 mm, size 46 $\times$ 27 cm) with a radius of about 0.4 m and with a total of effectively 30 independent sub-detectors. The required field-of-view to project a large heart is assumed to be approx. 18 cm $\times$ 15 cm, when the pinhole magnification is set to 1.5, which corresponds to two projections per camera. With this system set-up in mind we now can complete some rough calculations to compare standard clinical SPECT with this pinhole system:

The sensitivity of a dual head parallel-hole SPECT system (ParHole system) , with low-energy high-resolution (LEHR, hole diameter 1.4 mm and hole length 33 mm) parallel hole collimators is about 146 cpm/μCi per detector head, which is equivalent to a total geometric sensitivity of 0.017%. In the centre of the heart a resolution of about 8.7 mm is reached at 15.5 cm, which is assumed to be the average distance between the collimator and the centre of the left-ventricle centre in the comparison we do here between a stationary pinhole and the ParHole system. In order to achieve an equal system resolution at 15.5 cm with a pinhole camera, the pinhole diameter needs to be 4.9 mm, corresponding to a sensitivity of approx. 0.006 %. The pinhole set-up in figure 2.9, with 30 independent pinhole cameras has a sensitivity of 0.15 %, which is almost one order of magnitude higher than the sensitivity of the ParHole system. This indicates that one can make a scan with approximately the same reso-

lution but almost ten times faster than with a ParHole system. Alternatively, one can reduce the pinhole diameter to increase resolution. When we choose 1.63 mm, the efficiency is decreased to 0.017 %, which is equal to the ParHole system. However, now the pinhole system has a 2.1 times higher system resolution than the ParHole system (4.1 mm instead of 8.7 mm). If, in addition the intrinsic resolution of the detectors were to be 1.0 mm instead of 3.0 mm, it would be possible to achieve a system resolution better than 3 mm. This could mean an improvement over clinical PET systems. Note that the improvements over ParHole SPECT calculated here are based on projecting a large heart without projection overlap. With normal hearts significantly larger improvements can be obtained since more focussing pinholes can be used. Then however, a strategy is required to extend the field-of-view for imaging larger hearts. Finally, when large detector areas are available for the construction of clinical SPECT systems, pinholes will not be the only gateway to significantly improved performance: other focusing collimators (cone beam, multiple parallel hole collimators, crossed slits, slit-slat collimators, rotating mini-cameras etc.), will certainly be worth considering too.

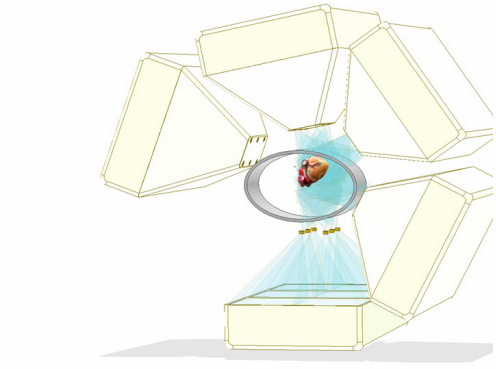

Figure 2.9: Cardiac SPECT system model with pinholes focusing to the heart. In the picture the shielding was removed from one multi-pinhole collimator to show how the heart is projected onto the detector without overlap. Means to avoid projection overlap (baffles) are not shown. This system has a significantly better resolution-sensitivity trade-off than a dual head parallel-hole SPECT system. In color print in the appendix.

2.10 Concluding remarks

Pinhole collimated imaging systems have been around for millions of years, for example in primitive eyes. Despite that collimation is inherently inefficient, its basic principles have been very useful for the construction of SPECT devices. The many kinds of eyes that have evolved from pinhole eyes [80] can be a source of inspiration to engineers in searching for alternatives to traditional gamma ray collimators and the currently used sub-optimal gamma ray detectors.

In recent years, significant progress has been made with the construction of small animal SPECT imaging. Even if developments are initially confined to the straightforward evolution of proven and readily available building blocks in concert with pinhole-like collimators, significant further improvements in both pre-clinical and clinical SPECT instruments can be expected. To further improve SPECT devices we need to direct our efforts to the production of low-cost high-resolution radiation detectors. Many other interesting developments are ongoing in SPECT system engineering. The many new and unforeseen applications that will spin off from-high resolution and flexible SPECT technology, together with new tracers and biological models are expected to contribute to a revolution in biomedical research.

Acknowledgements

The authors thank Dr. Cynthia Jongen, Dr. Steven Staelens, Dr Mart Rentmeester, Dr. Wojtek Zbijewski, Dr. Julia Huijbregts, Dr. Jeroen Pasterkamp, Brendan Vastenhouw (University Medical Centre Utrecht) and Prof. Brian Hutton (University College London) for many constructive comments. Dr. Freek Beekman is a board member and share holder of Molecular Imaging Laboratories, The Netherlands.

References

1. King MA, Pretorius PH, Farncombe T, Beekman FJ. Introduction to the physics of molecular imaging with radioactive tracers in small animals. J Cell Biochem 2002; suppl. 39: 221–30.

2. Meikle SR, Kench P, Kassiou M, Banati RB. Small animal SPECT and its place in the matrix of molecular imaging technologies. Phys Med Biol 2005; 50(22): R45–61.

3. Meikle S.R., Beekman F.J. and Rose S.E. “Complementary Molecular Imaging Technologies: High resolution SPECT, PET and MRI” (review). Drug Discovery Today

200; 3(2): 187–94.

4. Land MF. The spatial resolution of the pinhole eyes of giant clams (*Tridacna maxima*). Proc Biol Sci 2003; 270(1511): 185–8.

5. Hammond JH. The Camera Obscura, A Chronicle. Bristol: Adam Hilger Ltd; 1981.

6. Marignier JL. Historical light on photography. Nature 1990; 346: 115.

7. Copeland DE, Benjamin EW. Pinhole camera for gamma-ray sources. Nucleonics 1949; 5: 45–9

8. Anger HO. Scintillation Camera. Rev Sci Instr 1958; 27-33.

9. Mallard JR and Myers MJ. The performance of a gamma camera for the visualization of radioactive isotopes in vivo. Phys Med Biol 1963; 8: 165–82.

10. Wanet PM, Sand A, Abramovici J. Physical and clinical evaluation of high-resolution thyroid pinhole tomography. J Nucl Med 1996; 37: 2017–20.

11. Wouters A, Simon KM, Hirschberg JG. Direct method of decoding multiple images. Appl Opt 1973; 12: 1871.

12. Chang LT, Kaplan SN, Macdonald B, Perez-Mendez V, Shiraishi L. A method of tomographic imaging using a multiple pinhole coded aperture. J Nucl Med 1974; 15: 1063–5.

13. Seret A, Defrise M, Blocklet D. 180˚ Pinhole SPET with a tilted detector and OS-EM reconstruction: phantom studies and potential clinical applications. Eur J Nucl Med Mol Imaging 2001; 28(12): 1836–41.

14. Seret A, Flérès D, Firket O, Defrise M. Body contour 180˚ pinhole SPET with or without tilted detector: a phantom study. Eur J Nucl Med Mol Imaging 2003; 30(9): 1205–10.

15. Maillefert JF, Toubeau M, Piroth C, Piroth L, Brunotte F, Tavernier C. Bone scintigraphy equipped with a pinhole collimator for diagnosis of avascular necrosis of the femoral head. Clin Rheumatol 1997; 16(4): 372–7.

16. Pak Y-H, Bahk Y-W. Combined Scintigraphic and Radiographic Diagnosis of Bone and Joint Diseases. Berlin: Springer, 2004.

17. Spanu A, Falchi A, Manca A, Marongiu P, Cossu A, Pisu N et al. The Usefulness of Neck Pinhole SPECT as a Complementary Tool to Planar Scintigraphy in Primary and Secondary Hyperparathyroidism. J Nucl Med 2004; 45(1): 40–8.

18. Vogel RA, Kirch D, LeFree M, Steele P. A New Method of Multiplanar Emission Tomography Using a Seven Pinhole Collimator and an Anger Scintillation Camera. J Nucl Med 1978; 19: 648–54.

19. Jaszczak RJ, Li J, Wang H, Zalutsky MR, Coleman RE. Pinhole collimation for ultra-high-resolution small-field-of-view SPECT. Phys Med Biol 1994; 39: 425–37.

20. Beekman FJ, McElroy DP, Berger F, Gambhir SS, Hoffman EJ, Cherry SR. Towards in vivo nuclear microscopy: I-125 imaging in mice using micro-pinholes. Eur J Nucl Med Mol Imaging 2002; 29(7): 933–38.

21. Metzler SD, Bowsher JE, Greer KL, Jaszczak RJ. Analytic determination of the pinhole collimator's point-spread function and RMS resolution with penetration. IEEE Trans Med Imaging 2002; 21(8): 878–87.

22. Accorsi R, and Metzler SD, Analytic Determination of the Resolution-Equivalent Effective Diameter of a Pinhole Collimator, IEEE Trans. Med. Imaging 2004; 23(6): 750–63.

23. Palmer J and Wollmer P. Pinhole emission computed tomography: method and experimental evaluation. Phys Med Biol 1990; 35: 339–50.

24. Habraken JBA, de Bruin K, Shehata M, Booij J, Bennink R, van Eck Smit BL, et al. Evaluation of high-resolution pinhole SPECT using a small rotating animal. J Nucl Med 2001; 42: 1863–69.

25. Wu MC, Tang HR, Gao DW, Ido A, O'Connell JW, Hasegawa BH, et al. ECG gated pinhole SPECT in mice with millimeter resolution. IEEE Trans Nucl Sci 2000; 47: 1218–27.

26. McElroy DP, MacDonald LR, Beekman FJ, Wang YC, Patt BE, Iwanczyk JS, et al. Performance evaluation of A-SPECT: A high resolution desktop pinhole SPECT system for imaging small animals. IEEE Trans Nucl Sci 2002; 49: 2139–47.

27. Acton PD, Choi SR, Plossl K, Kung H F. Quantification of dopamine transporters in the mouse brain using ultra-high resolution single-photon emission tomography. Eur J Nucl Med Mol Imaging 2002; 29: 691–99.

28. Ishizu K, Mukai T, Yonekura Y, Pagani M, Fujita T, Magata Y, et al. Ultra-high-resolution SPECT system using four pinhole collimators for small animal studies. J Nucl Med 1995; 26: 2282–89.

29. Moore SC, Zimmerman RE, Mahmood A, Mellen R, Lim CB. A triple-detector multi-pinhole system for SPECT imaging of rodents. J Nucl Med 2005; 45(5): 97P.

30. Schramm NU, Ebel G, Engeland U, Schurrat T, Béhé M, Behr TM. High-Resolution SPECT using Multipinhole Collimation, IEEE Trans Nucl Sci 2003; 50(3): 315–20.

31. Meikle SR, Fulton RR, Eberl S, Dahlbom M, Wong K. P, Fulham MJ. An investigation of coded aperture imaging for small animal SPECT. IEEE Trans Nucl Sci 2001; 48: 816–21.

32. Feldkamp LA, Davis LC, Kress JW. Practical Cone-beam algorithm. J Opt Soc Am 1984; A1: 612–19.

33. Lange K, Carson REM. Reconstruction algorithms for emission and transmission tomography. J Comput Assist Tomogr 1984; 8: 306–16.

34. Furenlid LR, Chen Y, Kim, H. SPECT Imager design and data acquisition systems. In: Kupinski MA, Barrett HH, editors. Small animal SPECT imaging. New York: Springer Science+Business Media Inc. 2005, p.115–38.

35. Beekman FJ, van der Have F, Vastenhouw B, van der Linden AJA, van Rijk PP, Burbach JPH, Smidt MP. U-SPECT-I: A novel system for sub-millimeter resolution tomography of radiolabeled molecules in mice. J Nucl Med 2005; 46:1194–200.

36. Hudson HM and Larkin RS. Accelerated image reconstruction using ordered subsets of projection data. IEEE Trans Med Imaging 1994; 13: 601–9.

37. Hutton BF, Hudson HM, Beekman FJ. A clinical perspective of accelerated statistical reconstruction. Eur J Nucl Med 1997; 24: 797–808.

38. Lalush DS, Wernick MN. Iterative Image reconstruction. In: Wernick MN, Aarsvold JN, editors. Emission Tomography: The Fundamentals of PET and SPECT. San Diego: Academic Press, 2004

39. Barrett HH, Swindell W. Radiological Imaging. The theory of Image Formation, Detection, and Processing. New York: Academic Press, 1981.

40. Rogulski MM, Barber HB, Barrett HH, Shoemaker RL, Woolfenden JM. Ultra-high-resolution brain SPECT: simulation results. IEEE Trans Nucl Sci 1993; 40: 1123–29.

41. Rowe RK, Aarsvold JN, Barrett HH, Chen JC, Klein WP, Moore BA, et al. A stationary hemispherical SPECT imager for three-dimensional brain imaging. J Nucl Med 1993; 34: 474–80.

42. Patton DD, Barrett HH, Chen JC, Klein WP, Pang I, Richards D, et al. FASTSPECT – A 4-dimensional brain imager. J Nucl Med 1994; 35 (5): P93-P93 Suppl. S

43. Furenlid LR, Wilson DW, Chen Y, Kim H, Pietrski PJ, Crawford MJ, et al. FastSPECT II: a second-generation high-resolution dynamic SPECT imager. IEEE Trans Nucl Sci 2004; 51: 631–5.

44. Kastis GK, Barber HB, Barrett HH, Gifford HC, Pang IW, Patton DD, et al. High resolution SPECT imager for three-dimensional imaging of small animals (abstract). J Nucl Med 1998; 39(5): 25 Suppl S 9P.

45. Liu Z, Kastis GA, Stevenson GD, Barrett HH, Furenlid LR, Kupinski MA, et al. Quantitative analysis of acute myocardial infarct in rat hearts with ischemia-reperfusion using a high-resolution stationary SPECT system. J Nucl Med 2002; 43(7): 933–9.

46. Beekman FJ, Vastenhouw B. Design and simulation of a high-resolution stationary SPECT system for small animals. Phys Med Biol 2004; 49: 4579–92.

47. van der Have F, Vastenhouw B, Rentmeester MCM, Beekman FJ. System Calibration and Statistical Image Reconstruction for Sub-mm Stationary Pinhole SPECT. Conference Record of the 2005 Nuclear Science Symposium and Medical Imaging Conference, Puerto Rico, M11-291, 2005.

48. Vastenhouw B, Beekman FJ. Sub-mm Total Body Mouse Imaging with U-SPECT-I. J Nucl Med 2006 (in press).

49. Kupinski MA and Barrett HH, editors. Small-Animal SPECT imaging. New York: Springer Science+Business Media Inc., 2005.

50. Zeniya T, Watabe H, Aoi T, Kyeong MK, Teramoto N, Hayashi T, et al. A new reconstruction strategy for image improvement in pinhole SPECT, Eur J Nucl Med Mol Imaging 2004; 31(8): 1166–72.

51. Beque D, Nuyts J, Suetens P, Bormans G. IEEE Trans Med Imaging 2003; 22 (5): 599–612.

52. Metzler SD, Greer KL, Jaszczak RJ. Determination of mechanical and electronic shifts for pinhole SPECT using a single point source. IEEE Trans Med Imaging 2005; 24(3): 361–70.

53. Rentmeester MCM, van der Have F, Beekman FJ. Continuous model of Multi-Pinhole SPECT Devices. Conference Record of the 2005 IEEE Nuclear Science Symposium and Medical Imaging Conference, Puerto Rico. IEEE 2005; M03-283.

54. Cao ZX, Bal G, Accorsi R, Acton PD. Optimal number of pinholes in multi-pinhole SPECT for mouse brain imaging - a simulation study. Phys Med Biol 2005; 50(19): 4609–24.

55. Barber HB. Applications of semiconductor detectors to nuclear medicine. Nucl Instrum Methods Phys Res A 1999; 436: 102–10.

56. Fiorini C, Longoni A, Perotti F, Labanti C, Rossi E, Lechner P, Soltau H, Struder L. A monolithic array of silicon drift detectors coupled to a single scintillator for gamma-ray imaging with sub-millimeter position resolution. Nucl Instrum Methods Phys Res A 2003; 512: 265–71.

57. He Z, Li W, Knoll GF, Wehe DK, Berry J, Stahle CM. 3-D position sensitive CdZnTe gamma-ray spectrometers. Nucl Instrum Methods Phys Res A 1999; A422: 173–8.

58. Lees JE, Fraser GW, Keay A, Bassford D, Ott R, Ryder W. The high resolution gamma imager (HRGI): a CCD based camera for medical imaging. Nucl Instrum Methods Phys Res A 2003; 513(1-2): 23–6.

59. Llopart X, Campbell M, Dinapoli R, Segundo DS, Pemigotti E. Medipix2: a 64-k pixel readout chip with 55-μm square elements working in single photon counting mode. IEEE Trans Nucl Sci 2002; 49(5): 2279–83.

60. Matherson KJ, Barber HB, Barrett HH, Eskin JD, Dereniak EL, Marks DG, et al. Progress in the development of larger-area modular 64x64 CdZnTe imaging arrays for nuclear medicine. IEEE Trans Nucl Sci 1998; 45: 354–58.

61. Miyaata E, Tamur K. Novel Photon-Counting Detector for 0.1–100 keV X-Ray Imaging Possessing High Spatial Resolution. Jpn J Appl Phys 2003; 42: L1201–04, Part 2 No 10A.

62. Miyataa E, Mikia M, Tawaa N, Kamiyamaa D and Miyaguchi K. , Development of new X-ray imaging device sensitive to 0.1–100 keV. Nucl Instrum Methods Phys Res A 2004; 525: 122–5.

63. Nagarkar VV, Shestakova I, Gaysinskiy V, Tipnis SV, Singh B, Barber W, et al. A CCD-based detector for SPECT. IEEE Trans Nucl Sci 2006; 53(1): 54–8.

64. Vavrik D, Jakubek J, Visschers J, Pospisil S, Ponchut C, Zemankova J. First tests of a Medipix-1 pixel detector for X-ray dynamic defectoscopy. Nucl Instrum Methods Phys Res A 2002; 487(1-2): 216–23.

65. de Vree GA, Westra AH, van der Have F, Moody I, Ligtvoet CM, Beekman FJ. Photon Counting Gamma Camera based on an Electron-multiplying CCD, IEEE Trans Nucl Sci 2005; 52(3): 580–88.

66. Beekman FJ, de Vree GA. Photon-counting versus an integrating CCD-based gamma camera: important consequences for spatial resolution. Phys Med Biol 2005; 50(12): N109-19.

67. Kim H, Furenlid LR, Crawford MJ, Wilson DW, Barber HB, Peterson TE, et al. SemiSPECT: A small-animal single-photon emission computed tomography (SPECT) imager based on eight cadmium zinc telluride (CZT) detector arrays. Med Phys 2006; 33(2): 465–74.

68. Kastis GA, Wu MC, Balzer SJ, Wilson DW, Furenlid LR, Stevenson G, et al. Tomographic small-animal imaging using a high-resolution semiconductor camera. IEEE Trans Nucl Sci 2002; 49(1): 172–5.

69. Meng LJ, Clinthorne NH, Skinner S, Hay RV, Gross M. Design and Feasibility Study of a Single Photon Emission Microscope System for Small Animal I-125 Imaging. IEEE Trans Nucl Sci 2006; accepted for publication.

70. Funk T, Després P, Barber WC, Shah KS, Hasegawa BH. A multipinhole small animal SPECT system with submillimeter spatial resolution. Med Phys 2006; 33(5): 1259–67.

71. Beekman FJ. Stralingsdetectieinrichting. Dutch patent application, NL-1029558, July 2005.

72. Walrand S, Jamar F, de Jong M, Pauwels S. Evaluation of novel whole-body high-resolution rodent SPECT (Linoview) based on direct acquisition of linogram projections. J Nucl Med 2005; 46(11): 1872–80.

73. Huang Q, Zeng GL. An analytical algorithm for skew-slit imaging geometry with nonuniform attenuation correction. Med Phys 2006; 33(4): 997–1004.

74. Snigirev A, Kohn V, Snigireva I, Lengeler B. A compound refractive lens for focusing high-energy X-rays. Nature 1996; 384: 49-51.

75. Pivovaroff MJ, Barber WB, Christensen FE, Craig WW, Decker T, Epstein M, et al. Small-animal radionuclide imaging with focusing gamma-ray optics. Proc SPIE Int Soc Opt Eng 2004; 5199: 147.

76. Serlemitsos PJ. Conical foil X-ray mirrors: Performance and projections. Appl Opt 1988; 27 (8): 1447–52.

77. Serlemitsos PJ, Soong Y. Foil X-ray mirrors. Astrophys Space Sci 1996; 239: 177–96.

78. Hildebrandt G, Bradazek H. Approaching real X-ray optics. The Rigaku Journal 2000; 17: 13–22.

79. Weisenberger AG, Gleason SS, Goddard J, Kross B, Majewski S, Meikle SR, et al. A restraint-free small animal SPECT imaging system with motion tracking. IEEE Trans Nucl Sci 2005; 638-44.

80. Land MF. The optical structures of animal eyes. Curr Biol 2005; 15(9): R319–23.

Chapter 3

Photon penetration and scatter in micro-pinhole imaging: a Monte Carlo investigation

F van der Have and F J Beekman
Phys Med Biol 2004; 49: 1369–1386.

Abstract

Pinhole SPECT is rapidly gaining popularity for imaging laboratory animals using gamma-emitting molecules. Penetration and scattering of gamma radiation in the pinhole edge material can account for a significant fraction of the total number of photons detected, particularly if the pinholes have small diameters. This study characterises the effects of penetration and scatter with micro-pinholes made of lead, tungsten, gold and platinum. Monte Carlo simulations are performed for I-125 (27–35 keV) and Tc-99m (140 keV) point sources with pinhole diameters ranging from 50 to 500 μm. The simulations account for the effects of photo-electric interaction, Rayleigh scattering, Compton scattering, ionisation, bremsstrahlung and electron multiple scattering. As a typical example, in the case of a Tc-99m point source and pinholes with a diameter of 300 microns in gold or platinum, approx. 55 % of the photons detected resulted from penetration and approx. 3 % from scatter. For pinhole diameters ranging from 100 to 500 microns the penetration fraction for tungsten and lead was approx. a factor of 1.0 to 1.6 higher and the scatter fraction was 1.0 to 1.8 times higher than in case of gold

or platinum. Using I-125 instead of Tc-99m decreases the penetration fraction by a factor ranging from 3 to 11 and the scatter fraction by a factor ranging from 12 to 40. For all materials studied, the total amounts of penetrated and scattered photons changed approximately linearly with respect to the pinhole diameter.

3.1 Introduction

SPECT permits *in vivo* cross-sectional imaging of radio-labelled molecules. Pinhole SPECT is particularly suitable for small animals, because it can achieve an excellent resolution sensitivity tradeoff in small objects. Several SPECT systems using pinholes have been developed [1–9] for use with small animals. It has been shown, for example, that in small organs like the thyroid of a mouse, a resolution of as good as 200 microns can be obtained with planar imaging [10]. In SPECT a resolution of about 500 microns can be achieved [6], if micro-pinholes are used in conjunction with I-125. The majority of pinhole SPECT systems are based on scintillation cameras with an intrinsic detector resolution of approx. 2–3 mm. In order to obtain sufficient resolution, strong projection magnification is required to avoid blurring effects due to the intrinsic camera resolution; this requires a large camera size. As a result, only very few cameras can be placed around a small animal to collect photons simultaneously; consequently counting sensitivity will be limited. High-resolution detectors, on the other hand, require less image magnification. This means that more pinhole cameras can be placed around the object, leading to an increase in sensitivity; systems with ten up to hundreds of pinholes have been proposed [7, 11, 12]. Simulations have shown that the use of micro-pinholes can lead to a substantial increase of resolution, while the loss of sensitivity due to the smaller pinhole diameter can be compensated by the high number of pinholes [13, 14]. However, the use of smaller pinholes brings disadvantages: the fraction of penetrated and scattered photons increases, and this may have a detrimental effect on the quality of the reconstructed image. The fraction of photons that penetrates the edge of the aperture is known to be an important factor determining the image resolution and sensitivity *e.g.* [15–19]

Deloar *et al.* [20] investigated the combined effect of object and collimator scatter for the clinically used isotopes Tl-201, Tc-99m, I-123, and I-131, for pinhole diameters ranging from one to five mm. The effects of scattering around micro-pinholes have not yet been well characterised. The research presented here investigates scatter from micro-pinholes (50–500 μm) at energies ranging from 27 keV to 140 keV.

The general purpose of this paper is, to quantify effects of aperture penetration and scatter in micro-pinhole SPECT. Monte-Carlo simulations are performed to determine the spatial distribution and relative contributions of photons that have penetrated the pinhole material or

have scattered in the pinhole material. Four different pinhole materials (lead, tungsten, gold and platinum) are studied with the isotopes I-125 and Tc-99m. The dependency of penetration and aperture scatter on the pinhole diameter is investigated and a parametric model for this dependency is derived. Such knowledge will be useful for: (i) simulating SPECT systems; (ii) for optimising and designing SPECT systems, and (iii) for modelling photon transport during iterative reconstruction in order to improve the quality of reconstructed images.

3.2 Materials and methods

In pinhole gamma camera imaging, three different classes of photons can reach the detector: 'direct' photons, 'penetrated' photons and 'scattered' photons. Direct photons are those photons that have moved through the pinhole aperture to the detector. Penetrated photons are defined here as photons that have moved through the pinhole edge material without interacting with the pinhole material. Scattered photons are photons that have had an interaction with the pinhole material and are nevertheless detected. In this paper, photons created as secondary particles (e.g. as a result of bremsstrahlung from an electron that was itself created from a primary photon by photoelectric absorption or ionisation) are also considered to be scattered photons. Scattered photons often have a lower energy than the photons emitted by the source, and therefore they can be partly rejected from the image by energy discrimination. This section first describes basic models for the numbers of detected photons for each of the three types. Subsequently, details of the Monte-Carlo simulations are discussed.

3.2.1 Pinhole diameter

When the distance from the point source to the pinhole along the pinhole axis (r) is much larger than the pinhole diameter (d_{p}), the number of direct photons (N_{d}) can be approximated by the Anger formula:

$$N_{\mathrm{d}} = \frac{d_{\mathrm{p}}^2}{16r^2} N_0 \triangleq A \times d_{\mathrm{p}}^2 \tag{3.1}$$

where N_0 is the number of photons emitted by the source, and A is a parameter that is determined from the simulations and checked against the model.

For both penetration and scatter the relevant part of the pinhole is the material close to the rim/edge of the aperture. The volume of this material is a constant cross-section times the perimeter. Therefore, the amounts of both penetrated and scattered photons detected can be expected to be roughly linearly related to the pinhole diameter. If the pinhole diameter is reduced to zero, a finite amount of penetration and scatter will remain. When a constant

describing the latter effect is added, the parametric linear model for the quantity of penetrated photons (N_p) reads:

$$N_\mathrm{p} = B \times d_\mathrm{p} + C \tag{3.2}$$

and for the amount of detected scattered photons (N_s):

$$N_\mathrm{s} = D \times d_\mathrm{p} + E \tag{3.3}$$

where B, C, D, and E, just like A, are model parameters.

An "effective diameter" (d_e) formula, such as introduced by Anger [21] and Paix [22] can be used to predict the amount of penetration. The formulation of the effective diameter as reported by Paix [22] and later by Smith [16] can be used to estimate both B/A and C/A using the linear attenuation coefficient μ and the pinhole opening angle α:

$$d_\mathrm{e} = \sqrt{d_\mathrm{p}^2 + d_\mathrm{p}\frac{2}{\mu}\tan\left(\frac{\alpha}{2}\right) + \frac{2}{\mu^2}\tan^2\left(\frac{\alpha}{2}\right)} \tag{3.4}$$

$$\frac{B}{A} = \frac{2}{\mu}\tan\left(\frac{\alpha}{2}\right) \qquad \frac{C}{A} = \frac{2}{\mu^2}\tan^2\left(\frac{\alpha}{2}\right) \tag{3.5}$$

The formulation of Paix [22], equivalent to equation 3.4 and hereafter referred to as the Paix model, has been extended to describe cases where the point source is not located on the pinhole axis by Metzler [17].

3.2.2 Monte-Carlo simulation

Monte-Carlo simulation (MCS) is a very suitable technique for studying particle transport since the underlying physics is well known. The results are calculated from the first principles of physics. Therefore MCS is an accurate and general tool in such simulations. In nuclear medicine, MCS is a well established technique for simulating photon transport. A disadvantage of MCS are the long computations that may be required: often many millions of random events have to be simulated to obtain results with a sufficiently low noise level.

The MCS software used in this paper is Geant version 4.5.0. Geant is an acronym for "GEometry ANd Tracking", and has been developed by CERN and its collaborators [23, 24]. The program is used in particle physics, dosimetry and radiotherapy *e.g.* [25–28] Geant is being introduced to nuclear medicine and with the development of a project called GATE (Geant4 application for tomographic emission) it will become more user-friendly specifically for SPECT and PET [29, 30]. For the simulations in this study, plain Geant was used, with the low-energy extensions for the photoelectric effect, the Compton effect, Rayleigh scattering, ionisation and bremsstrahlung, which are available in recent versions of Geant.

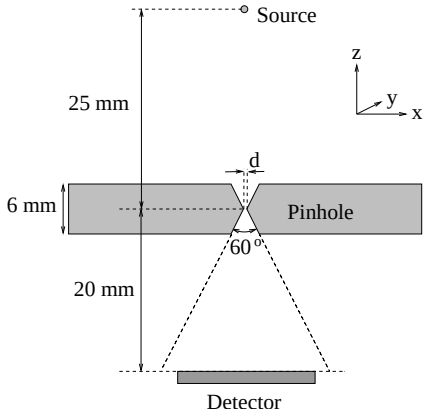

Figure 3.1: The geometry of the system with a point source, a pinhole and a detector.

The pinhole and detector geometry is shown in figure 3.1. An isotropic point source, which in most simulations is located on the pinhole central axis, emits mono-energetic gamma photons for Tc-99m (140 keV) or a combined X-ray and gamma spectrum in the case of I-125 (27–35 keV). The pinhole is rotationally symmetric and has a knife-edge. The acceptance angle is $60\,^{\circ}$. The collimator material (6 mm) is taken thick enough to prevent appreciable collimator penetration outside the edge area of the aperture. The distance from the source to the pinhole is 25 mm, from the pinhole to the detector 20 mm. The detector is a square measuring 16.3×16.3 mm. This is the largest inscribed square in the illumination circle (where "direct" photons could hit the detector) defined by the acceptance angle and the distance from the pinhole to the detector. These dimensions were chosen because they would be appropriate for a small-animal SPECT system that incorporates many micro-pinholes in conjunction with high resolution mini gamma-cameras [13, 14].

The simulation stores the location of the hit, the type of particle (direct, penetrated or scattered), and the energy for all gamma photons that reach the detector. MCS gives the physical energy of the photons. The effect of a gamma camera's energy resolution is simulated by drawing the energy as a random number from a normal (Gaussian) distribution with the physical energy as mean. The Full Width of Half Maximum was chosen to be 14 keV or 10 % for Tc-99m and also 14 keV for I-125.

The photons emitted from the source were confined to a cone with a half top angle of $\approx 6\,^{\circ}$, in such a way that the conical part of the pinhole is always fully illuminated. This increases the sensitivity by a factor of more than 300. No other methods to speed up the computations (such as forced detection) were used. The simulations were run on Intel Xeon

2.4 GHz processors. Typically, the simulation takes 1.5 hours per 10 million photons emitted by the source.

Two systems have been simulated: a photon counting system and an energy weighting system. For simulations representing a photon counting detector, an energy window was used, with limits 140 $\pm$14 keV (126–154 keV) for Tc-99m and 30 $\pm$14 keV (16–44 keV) for I-125. An energy integrating detector was also simulated in such a way that the contribution of photons was proportional to their detected energy. Both an energy window (rejecting photons with an energy not in range) and weighting according to energy have little effect on the contribution of direct and penetrated photons, but can significantly reduce the amount of scatter detected since a significant fraction of the scattered photons has a much lower energy than the primary photons.

3.3 Results

This section first shows examples of the distribution of photons detected on the detector plane. Next, total fractions of direct, penetrated and scattered photons are shown with photon counting and integrating detectors. We also present the energy distribution of the scattered photons and calculate the dependency of the numbers of direct, penetrated and scattered photons on the pinhole diameter. The penetration component of the simulation results is compared to the values predicted by equation 3.4 (Paix model).

3.3.1 Distribution on the detector

Figures 3.2, 3.3, and 3.4 show grey value images representing the spatial distribution of the different types of detected photons as well as associated image profiles for a Tc-99m source on the pinhole axis, a Tc-99m source that is 23.3 $^\circ$ off the pinhole axis and an I-125 source on the pinhole axis, respectively. Energy windows of 126–154 keV (Tc-99m) and 16–44 keV (I-125) are used. Approximately 12, 17 and 36 billion photons emitted by the source were simulated. The images of the direct photons resemble discs with a sharp edge; these discs correspond to the geometrical shape of the projection of the aperture on the detector. The penetration component is ring-shaped, sharp-edged on the inside and gradually falling off on the outside. As expected from the pinhole shape, the penetration fall off is exponential with respect to the distance from the centre (figures 3.2 and 3.3). On a pixel basis, the scatter component is orders of magnitude ($> 10^3$ for Tc-99m and $> 10^5$ for I-125) lower than the maximum intensity of the direct photons (note the different scale bars in the images), but the scatter is spread across all of the detector surface.

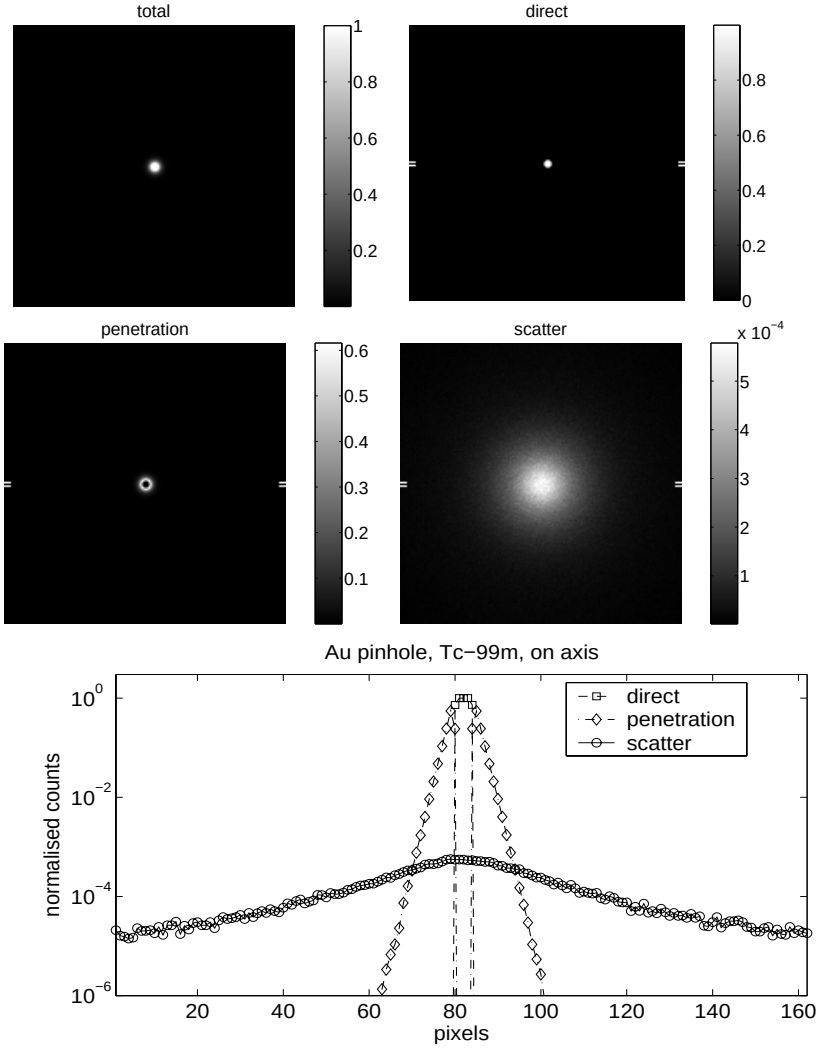

Figure 3.2: Distribution on the detector from an on-axis Tc-99m source and associated image profiles, normalised to the maximum in “total”.

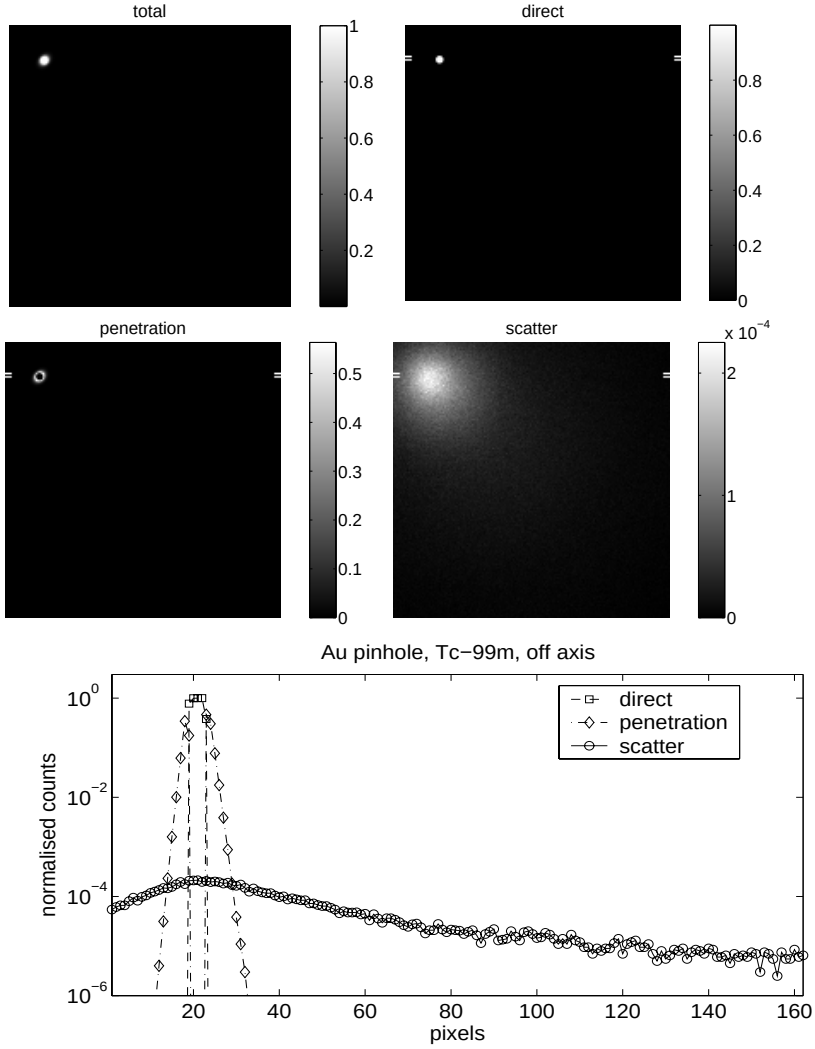

Figure 3.3: Distribution on the detector from an off-axis Tc-99m source and associated image profiles, normalised to the maximum in “total”.

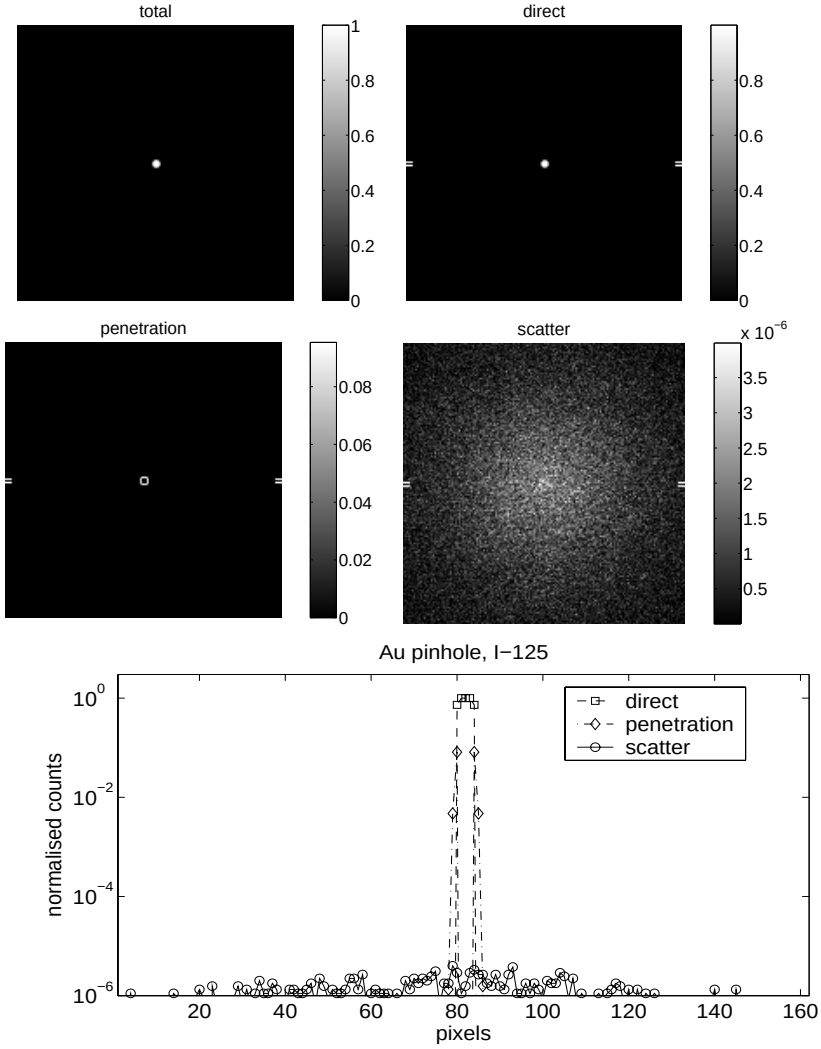

Figure 3.4: Distribution on the detector from an on-axis I-125 source and associated image profiles, normalised to the maximum in “total”.

3.3.2 Numerical data

Table 3.1: Fractions of detected direct, penetrated, and scattered photons; calculated for Pb, W, Au, and Pt and an energy window of ± 14 keV.

pinhole		Pb			W	
diameter (microns)	100	300	500	100	300	500
Tc-99m direct %	6.56	28.09	43.92	10.15	36.73	53.00
Tc-99m penetration %	88.14	68.43	53.54	84.23	59.90	44.79
Tc-99m scatter %	5.30	3.48	2.54	5.62	3.37	2.31
I-125 direct %	73.81	90.58	94.16	78.80	92.48	95.40
I-125 penetration %	25.77	9.27	5.75	20.74	7.37	4.52
I-125 scatter %	0.43	0.14	0.09	0.46	0.15	0.08
pinhole		Au			Pt	
diameter (microns)	100	300	500	100	300	500
Tc-99m direct %	12.80	42.02	58.06	14.27	44.26	60.12
Tc-99m penetration %	82.27	55.19	40.07	80.79	53.08	38.12
Tc-99m scatter %	4.93	2.78	1.88	4.94	2.66	1.76
I-125 direct %	82.00	93.70	96.17	83.00	94.13	96.42
I-125 penetration %	17.69	6.20	3.77	16.69	5.78	3.53
I-125 scatter %	0.30	0.10	0.06	0.30	0.09	0.05

In tables 3.1 and 3.2 the fractions of detected direct, penetrated and scattered photons with respect to the total number of photons detected are listed for pinhole diameters 100, 300 and 500 μm. In these simulations, 50 million photons were emitted by the source. If I-125 and Tc-99m are compared, we find that the main difference is the much lower penetration and scatter fraction for I-125. In the case of Tc-99m, approximately 40 to 80 % of the detected photons are penetrated photons, whereas in the case of I-125 only about 4 to 20 % are penetrated photons. The scatter fraction for Tc-99m is not as high as the penetration fraction, but it is still around 5 % for the 100 μm diameter pinholes. The scatter fraction for I-125 is below 0.5 % in all cases listed in table 3.1. For all corresponding situations, the scatter fraction is more than an order of magnitude lower for I-125 than for Tc-99m, even up to a factor of 30 or 40 for a 500 μm pinhole diameter. Comparing the materials, we find that the order of performance from poorest to best is lead, tungsten, gold, and platinum.

The major difference between the photon counting system using an energy window (table 3.1) and the integrating system (table 3.2) is that the scatter fraction is higher with the integrating system with Tc-99m. As expected, the direct and penetration fractions decrease

Table 3.2: The same data as in table 3.1, in this table with an energy-integrating system instead of an energy window.

pinhole		Pb			W	
diameter (microns)	100	300	500	100	300	500
Tc-99m direct %	6.35	27.54	43.28	10.03	36.48	52.72
Tc-99m penetration %	85.55	67.04	52.73	83.32	59.47	44.45
Tc-99m scatter %	8.10	5.42	3.99	6.65	4.06	2.83
I-125 direct %	73.35	90.37	94.03	78.60	92.30	95.29
I-125 penetration %	26.16	9.46	5.86	20.91	7.54	4.62
I-125 scatter %	0.49	0.18	0.11	0.50	0.16	0.09
pinhole		Au			Pt	
diameter (microns)	100	300	500	100	300	500
Tc-99m direct %	12.55	41.58	57.61	14.03	43.84	59.73
Tc-99m penetration %	80.74	54.57	39.77	79.48	52.57	37.87
Tc-99m scatter %	6.71	3.85	2.62	6.49	3.60	2.40
I-125 direct %	81.65	93.56	96.09	82.69	93.99	96.33
I-125 penetration %	17.99	6.33	3.85	16.94	5.91	3.60
I-125 scatter %	0.36	0.11	0.07	0.37	0.10	0.06

accordingly. Interestingly, for I-125, when an integrating system is used, the fraction of direct photons decreases but the penetration fraction increases (unexpectedly). This can be explained by the fact that Tc-99m is mono-energetic and I-125 emits a spectrum (27–35 keV). The existence of different energies in the system promotes "beam-hardening". Hence, penetration has a higher probability of occurring for a photon at a higher energy. Therefore, the energy spectrum of penetrated photons is shifted towards a greater abundance of higher energies with respect to the energies emitted by the source. Because the contributions to the number of counts are energy-weighted, this explains the increased penetration fraction.

3.3.3 Energy distribution of scattered photons

The energy distribution (without applying Gaussian detector energy response) and cumulative energy distribution of the scattered photons reaching the detector are plotted for a 300 microns diameter gold pinhole. See figure 3.5 for Tc-99m and figure 3.6 for I-125.

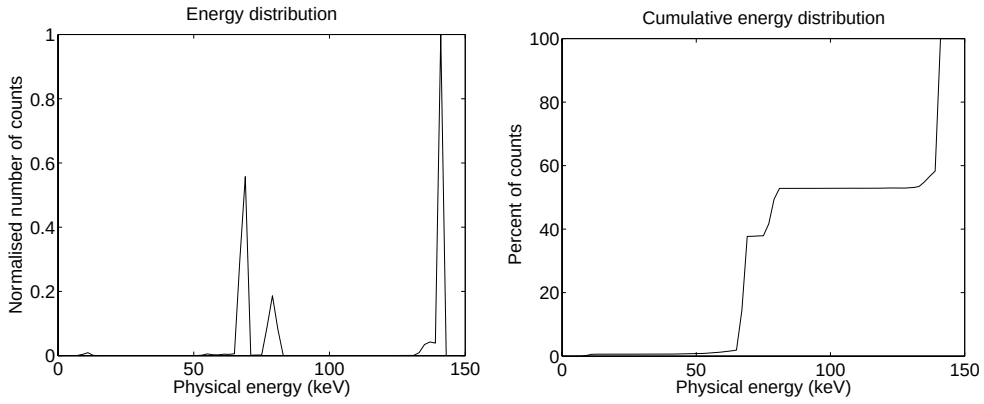

Figure 3.5: Energy distribution (left) and cumulative energy distribution (right) of scattered photons reaching the detector for a gold pinhole and a Tc-99m source. The energy used here is the physical energy of the scattered photons reaching the detector. Note that more than 50 % of the scattered photons have an energy below 90 keV.

For Tc-99m, half of the scattered photons have an energy between 60 and 80 keV, whereas for I-125 around 30 % of the scatter is below 27 keV. The energy distribution is not a smooth curve but shows distinct peaks; this can be explained by the characteristic X-rays from gold. For example, the $K_{\alpha 1}$ energy for gold is 68.8 keV. The implications of the distribution are elucidated in the discussion section.

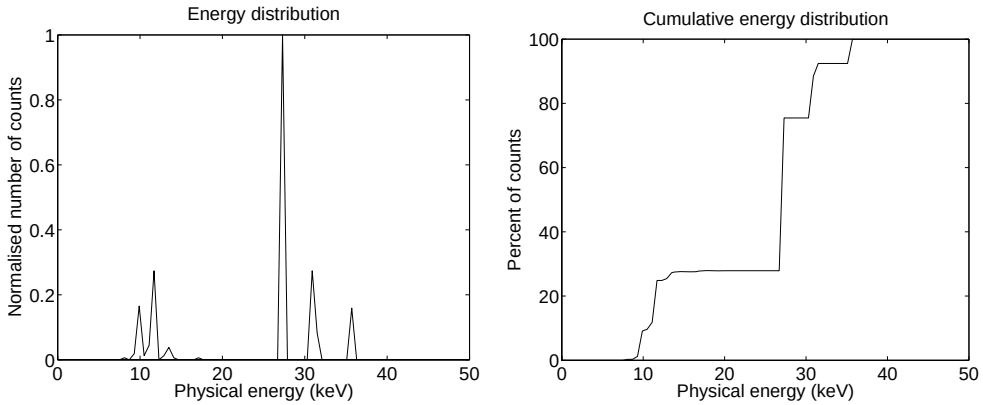

Figure 3.6: Like figure 3.5, but for an I-125 source. Note that about 30 % of the scattered photons have an energy below 15 keV.

3.3.4 Pinhole diameter dependency

The number of counts for direct, penetrated and scattered photons on the detector are shown as a function of pinhole diameter (figure 3.7 for Tc-99m and figure 3.8 for I-125). In the simulation for each data point, the source emitted 50 million photons in a cone with a half-top-angle of 6.417 °. For clarity, the plots for the scatter component are shown separately on a different scale in figure 3.9. Note that the vertical axes denote absolute numbers of photons, whereas in the preceding tables the numbers denote relative fractions. Least-squares curve fits are applied with the linear relations described in section 3.2.1. As shown in the figures, the model fits well to the data. The data for scattered I-125 photons deviate more from the fits; this can be explained by the count statistics associated with the low number of detected photons in this particular case.

Figures 3.7 and 3.8 demonstrate at what pinhole diameter the direct photons become dominant (the highest relative contribution). With Tc-99m, for W, Au, and Pt, they become dominant at 350–430 µm. For Pb they dominate at above 500 µm. In contrast, with I-125 the direct photons form the largest fraction below 50 µm for all these materials. This demonstrates again that lower pinhole diameters make sense for I-125 than for Tc-99m.

The curve fits determine five parameters (A – E in section 3.2.1); the values of A, B and C can also be predicted from equations 3.1 and 3.5. For the simulations used in figures 3.7 and 3.8 the values of the five model parameters obtained from a curve fit, as well as theoretical predictions for these values for the direct and penetration components are listed in table 3.3 for Tc-99m and table 3.4 for I-125. The units in the table are μm^{-2} for A, μm^{-1} for B and D,

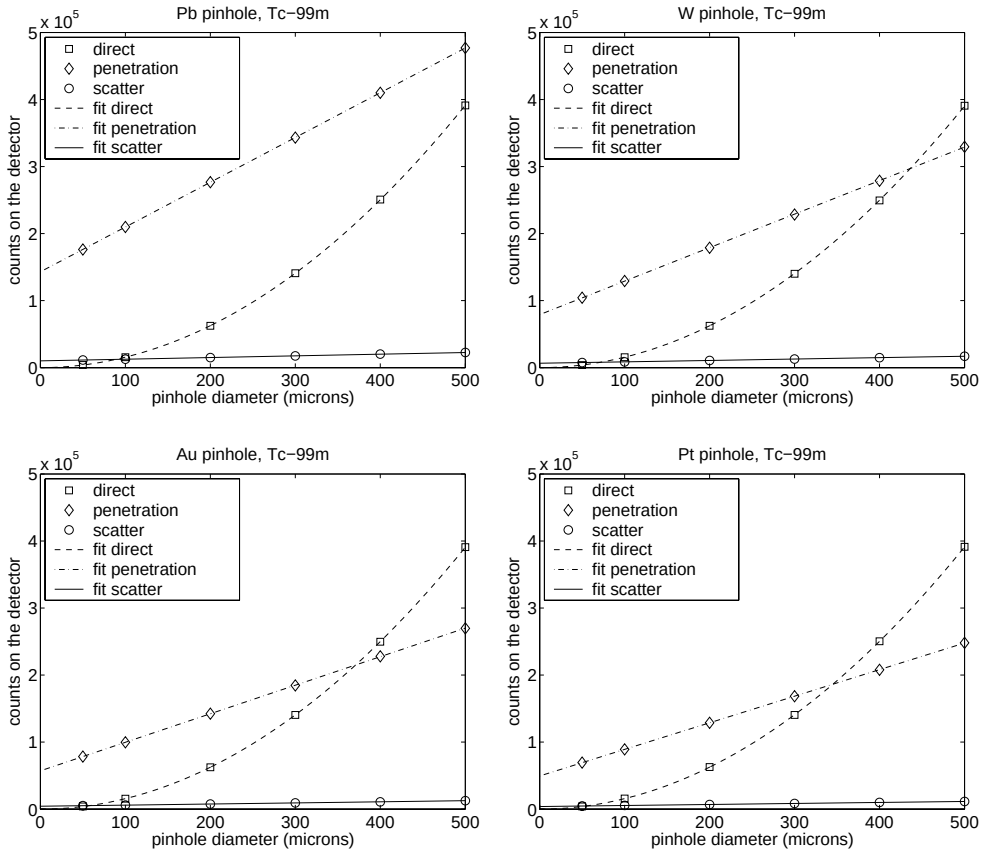

Figure 3.7: Dependency of the number of direct, penetration, and scatter photons on the pinhole diameter for Tc-99m. The data points are the results of MCS and the lines are least-squares fits according to the parametric model in section 3.2.1.

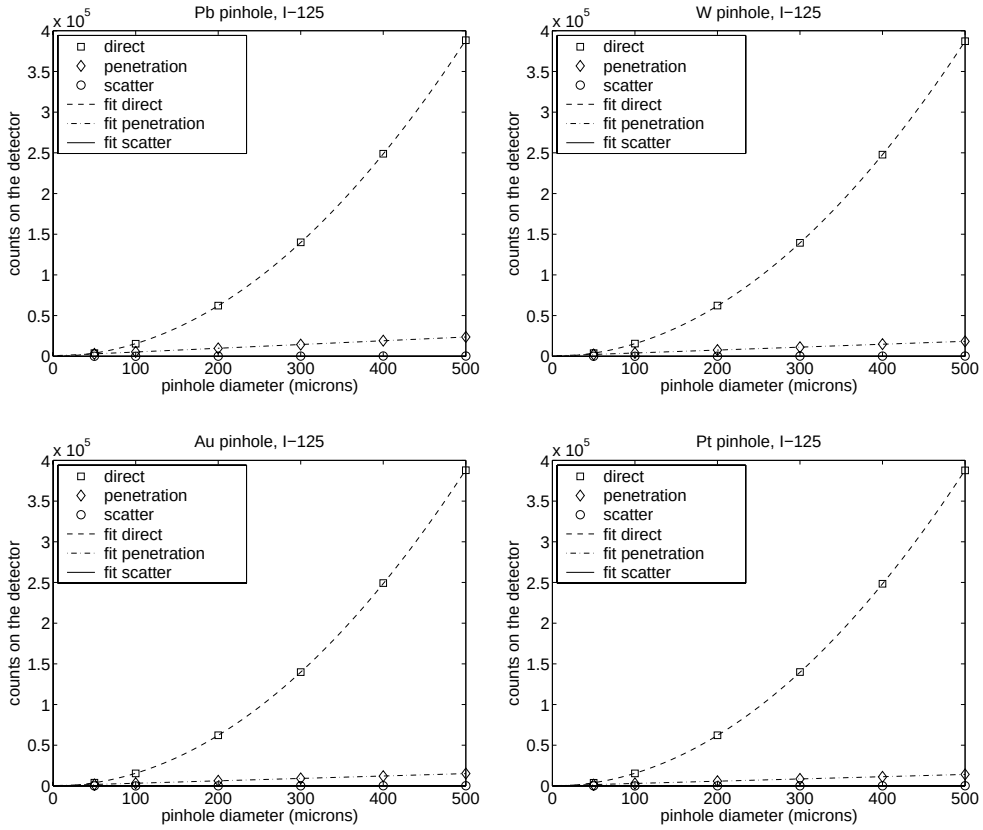

Figure 3.8: Like figure 3.7 but for I-125.

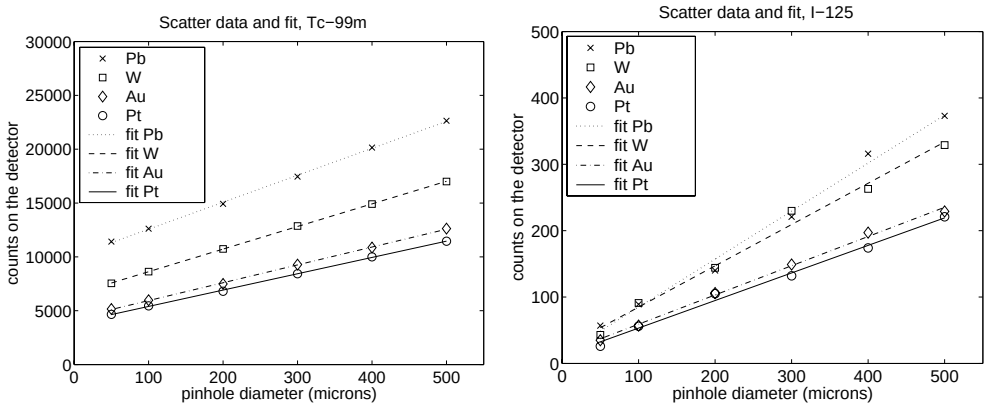

Figure 3.9: The data and model of the scatter component from figures 3.7 and 3.8.

Table 3.3: The five model parameters A–E for the cases in figure 3.7. The number of direct, penetrated and scattered photons as a function of the pinhole diameter (in μm) are $N_{\rm d} = A \times d_{\rm p}^2$, $N_{\rm p} = B \times d_{\rm p} + C$, and $N_{\rm s} = D \times d_{\rm p} + E$ respectively (section 3.2.1). "Fit model" values are the result of the curve fit to the Geant data, "Paix" are the predicted values according to equations 3.1 and 3.5.

	Au	Pt	Pb	W
A (fit model)	1.56248	1.56481	1.56546	1.56133
A (Paix)	1.56654	1.56654	1.56654	1.56654
difference	-0.26%	-0.11%	-0.07%	-0.33%
B (fit model)	425.729	396.705	667.848	499.867
B (Paix)	423.654	392.234	666.833	498.535
difference	0.49%	1.14%	0.15%	0.27%
C (fit model)	57114.2	49434.3	142978	79058.3
C (Paix)	57286.4	49104.2	141926.2	79326.8
difference	-0.30%	0.67%	0.74%	-0.34%
D (fit model)	16.5707	15.1656	25.0199	20.9940
E (fit model)	4283.56	3881.56	10071.2	6523.71

Table 3.4: Like tabel 3.3 for I-125 and figure 3.8.

	Au	Pt	Pb	W
A (fit model)	1.55374	1.55196	1.55420	1.54874
A (Paix)	1.54696	1.54696	1.54696	1.54696
difference	0.44%	0.32%	0.47%	0.12%
B (fit model)	29.6336	27.6755	46.1074	35.8477
B (Paix)	30.0105	28.1576	46.3868	36.3432
difference	-1.26%	-1.71%	-0.60%	-1.36%
C (fit model)	308.156	256.008	627.589	455.685
C (Paix)	300.984	264.929	718.292	441.507
difference	2.38%	-3.37%	-12.63%	3.21%
D (fit model)	0.44027	0.41523	0.72318	0.62192
E (fit model)	15.0959	11.7315	12.5123	22.6712

and dimensionless for C and E. The “Paix model” values are according to equation 3.5, but corrected for the detector energy window since that is also applied in the simulations. This correction and the calculation for B and C are done for Tc-99m and for each of the energies in the I-125 spectrum separately, using attenuation coefficients from [31]. The simulation results match the theoretical values very well, in many cases to within 1 %. The largest relative differences occur in the value of C for I-125. The value of C itself is the number of penetration photons when the pinhole diameter is zero (but there is still a knife edge shape): if this value is only a few hundred photons then several percent of error can be expected by count statistics alone.

Tables 3.5 and 3.6 contain the ratio of the number of penetrated to the number of direct photons for Tc-99m and for I-125. The table compares the results of the Geant Monte Carlo simulations to both the predicted values according to the Paix model (equation 3.5) and the fit curves in figures 3.7 and 3.8 evaluated at the same diameter values. For Tc-99m, the majority of the comparisons results in less than 1 % difference and the highest deviation is 2.5 %. For I-125, the deviations are generally somewhat larger (the largest is 3.5 %) and there appears to be a correlation between the deviation of the Paix model and the deviation of the curve fits. Considering the lower numbers of penetrated photons with I-125 and the observation that both positive and negative deviations occur, this may indicate the observed differences are largely due to the count statistics in the simulation data. Overall the comparison shows that the penetration part of the simulations in this paper matches well with what was already known about penetration in knife-edge pinholes. Since equation 3.4 was experimentally verified for

Table 3.5: The number of penetrated photons divided by the number of direct photons for Tc-99m. "Geant" values are the numbers obtained from the simulations (the data points in figure 3.7). "Paix model" values are according to equation 3.5. "Fit model" values are according to the curves in figure 3.7.

		Pt			Au	
d(mm)	Geant	Paix model	Fit model	Geant	Paix model	Fit model
0.05	17.66	17.54(-0.7%)	17.71(0.3%)	20.05	20.03(-0.1%)	20.07(0.1%)
0.1	5.661	5.638(-0.4%)	5.694(0.6%)	6.428	6.361(-1.1%)	6.380(-0.8%)
0.2	2.052	2.035(-0.8%)	2.057(0.3%)	2.281	2.266(-0.6%)	2.276(-0.2%)
0.3	1.199	1.183(-1.4%)	1.196(-0.3%)	1.313	1.308(-0.4%)	1.314(0.1%)
0.4	0.830	0.822(-1.0%)	0.831(0.2%)	0.913	0.905(-0.9%)	0.910(-0.3%)
0.5	0.634	0.626(-1.2%)	0.633(-0.1%)	0.690	0.687(-0.4%)	0.691(0.2%)
		W			Pb	
d(mm)	Geant	Paix model	Fit model	Geant	Paix model	Fit model
0.05	26.72	26.63(-0.4%)	26.66(-0.2%)	43.95	44.74(1.8%)	45.07(2.5%)
0.1	8.301	8.248(-0.6%)	8.265(-0.4%)	13.45	13.31(-1.0%)	13.40(-0.4%)
0.2	2.867	2.858(-0.3%)	2.867(-0.0%)	4.430	4.392(-0.8%)	4.416(-0.3%)
0.3	1.631	1.624(-0.4%)	1.630(-0.1%)	2.437	2.425(-0.5%)	2.437(0.0%)
0.4	1.118	1.112(-0.5%)	1.117(-0.1%)	1.635	1.630(-0.3%)	1.637(0.1%)
0.5	0.843	0.839(-0.5%)	0.843(-0.0%)	1.219	1.214(-0.5%)	1.219(-0.1%)

Table 3.6: Like table 3.5, for I-125 with Fit model corresponding to curves in figure 3.8.

		Pt			Au	
d(mm)	Geant	Paix model	Fit model	Geant	Paix model	Fit model
0.05	0.414	0.427(3.0%)	0.423(2.1%)	0.446	0.459(3.1%)	0.461(3.4%)
0.1	0.201	0.196(-2.3%)	0.195(-3.1%)	0.216	0.211(-2.5%)	0.211(-2.4%)
0.2	0.094	0.094(-0.2%)	0.093(-1.0%)	0.101	0.101(-0.2%)	0.100(-0.4%)
0.3	0.061	0.062(0.5%)	0.061(-0.2%)	0.066	0.066(-0.3%)	0.066(-0.5%)
0.4	0.045	0.046(2.2%)	0.046(1.6%)	0.048	0.049(1.9%)	0.049(1.7%)
0.5	0.037	0.037(0.0%)	0.036(-0.8%)	0.039	0.039(-0.5%)	0.039(-0.7%)
		W			Pb	
d(mm)	Geant	Paix model	Fit model	Geant	Paix model	Fit model
0.05	0.579	0.576(-0.6%)	0.581(0.2%)	0.766	0.774(1.1%)	0.755(-1.5%)
0.1	0.263	0.260(-1.3%)	0.261(-0.9%)	0.349	0.341(-2.2%)	0.337(-3.5%)
0.2	0.123	0.123(0.3%)	0.123(0.5%)	0.156	0.159(2.3%)	0.158(1.8%)
0.3	0.080	0.080(0.9%)	0.080(0.9%)	0.102	0.104(1.3%)	0.103(1.0%)
0.4	0.060	0.060(-0.7%)	0.060(-0.7%)	0.077	0.077(-0.3%)	0.077(-0.4%)
0.5	0.047	0.048(0.2%)	0.047(0.1%)	0.061	0.061(-0.2%)	0.061(-0.2%)

some cases [16] the penetration component of the Monte Carlo simulations inhere can be regarded as validated indirectly.

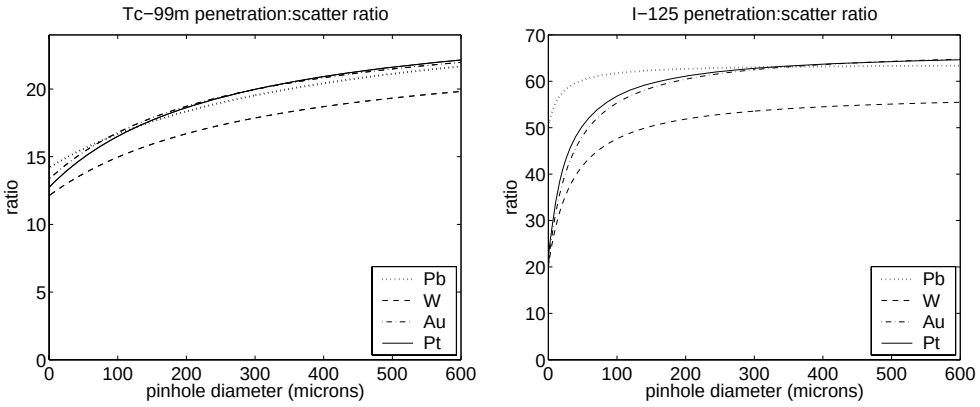

Figure 3.10: The ratio of total counted penetrated to scattered photons for Tc-99m(left) and I-125(right) as a function of pinhole diameter.

The model can be used also to investigate the ratio of the penetration to the scatter as a function of the pinhole diameter. This is shown in figure 3.10 for Tc-99m and I-125. The expected behaviour is that the penetration to scatter ratio is constant above a certain (small) pinhole diameter, because both the detected penetrated photons and the detected scattered photons should originate from the same small edge around the aperture. The expected behaviour is seen with I-125, but there is a stronger diameter dependence for Tc-99m. This finding indicates that for Tc-99m, there are penetrated or scattered photons reaching the detector that originate from deeper areas in the pinhole material and at a greater distance from the pinhole centre.

3.4 Discussion

To characterise penetration and scatter for lead, tungsten, gold and platinum micro-pinhole apertures, we performed Monte Carlo simulations for I-125 (27–35 keV) and Tc-99m (140 keV).

The four pinhole materials studied belong to the same row in the periodic table of the elements and have a relatively high Z (atomic number). Gold ($Z = 79$, $\rho = 19.32\ \mathrm{g/cm^3}$) and platinum ($Z = 78$, $\rho = 21.45\ \mathrm{g/cm^3}$) have either a higher ρ (mass density) or a higher Z than lead ($Z = 82$, $\rho = 11.35\ \mathrm{g/cm^3}$) and tungsten($Z = 74$, $\rho = 19.30\ \mathrm{g/cm^3}$), which

makes them superior stopping materials. Uranium ($Z = 92$, $\rho = 18.95\ \mathrm{g/cm^3}$) has an even better stopping power, but has the disadvantage that pinholes would be hard to manufacture. U-238 is not readily available, the toxic uranium oxide may be shed and the radioactivity of depleted uranium can contaminate the pinhole image.

In the present study several choices have been made with respect to geometry and energy resolution. If a different pinhole acceptance angle or a micro-pinhole with a channel had been used, this of course would have affected the numerical results. Characterising the penetration and scatter for differently shaped micro-pinholes is a subject for future investigation. The values for source-to-pinhole and pinhole-to-detector distances have been chosen according to novel designs of multi-pinhole SPECT systems. The results for the scatter distribution on the detector can easily be extended to the situation where a larger detector is placed correspondingly further away from the pinhole, because the distribution is determined completely by the angular distribution of the scatter photons emerging from the pinhole area. Generally, even if the exact numbers are different in other systems due to a different geometry, we expect that the trends observed in this paper will still give good indications of what to expect under these changed conditions.

We now consider the energy distribution described in section 3.3.3. The cumulative energy curves in figures 3.5 and 3.6 can be used to answer the question: what energy resolution of the system is required for a given fraction of the scattered photons to be rejected? For example, the flat part of the cumulative distribution between 80 and 140 keV for Tc-99m means that any system energy resolution between ≈ 5 and 60 keV would reject ≈ 55 % of the scattered photons. Similarly for I-125, 30 % of the scattered photons can be rejected if the system can distinguish between 12 keV and 27 keV photons. However, the scatter fraction for I-125 is so low that it may not be worthwhile applying energy discrimination for pinhole scatter reduction. The results obtained can be used to guide decisions about which detectors to use for novel micro-SPECT systems.

The present paper quantifies effects of both penetration and scatter in pinholes. A possible application is to take such characteristics into account during SPECT reconstruction in order to correct for these effects. Iterative algorithms use a transition matrix which can be represented by point spread function tables. If the effects of penetration and scatter are incorporated accurately, corrections for these effects can be done fairly well. An example of an algorithm that models penetration, and which is dedicated for incorporation in iterative reconstruction software is listed in [19]. Iterative correction for both scatter have been performed in the past for clinical SPECT *e.g.* [32–36] In addition energy based correction methods have been proposed *e.g.* [37–40] which do not depend on the characteristics determined inhere.

3.5 Conclusions

We have characterised the aperture penetration and scatter in micro-pinholes by studying the spatial distribution on the detector, energy distribution of scatter and pinhole diameter dependency.

For the knife-edge micro-pinholes considered, the number of penetrated and scattered photons is well described by linear functions of the pinhole diameter, as was shown by Monte-Carlo simulations. For Tc-99m the overall detected scatter fraction ranges from a very few percent up to several percent of the total detected photons. For I-125 the fraction is more than an order of magnitude lower, and always below 0.6 %. The number of scattered photons per pixel was more than 3 orders of magnitude below the number of direct photons in the central part of the point spread function. Platinum and gold are superior to tungsten and lead with regard to pinhole scatter, while platinum performs slightly better than gold. The penetration component of the simulation results matches well (in many cases within 1 %) to values predicted by the effective diameter equation in [16, 17, 22].

For Tc-99m, approximately 55 % of the scattered photons can be removed from the measurement by energy discrimination if the system energy resolution is better than 40 %. For I-125, approximately 30 % of the scattered photons can be rejected if the system energy resolution is better than 15 keV (50 %). This resolution can be hard to achieve for a detector at 30 keV, but the fraction of scattered particles is already so low for I-125 that a further reduction by energy discrimination may not be worth the effort.

The results presented in this paper may be useful for guiding the design of high resolution detectors and pinholes for small animal SPECT systems. Design considerations comprise that energy discrimination can be hard to achieve with some types of detectors and pinhole sizes need to be chosen such that they are suitable for the energy of the isotope of interest.

Acknowledgments

We thank Dr A P Colijn for his help with the Geant simulations. We thank Dr C R Tenney at Thomas Jefferson University for fruitful discussions. This work was sponsored by the Netherlands Organisation for Scientific Research, grant 917.036.335.

Bibliography

[1] R J Jaszczak, J Li, H Wang, M R Zalutsky, and R E Coleman. Pinhole collimation for ultra-high-resolution small-field-of-view SPECT. *Phys.Med.Biol.*, 39:425–37, 1994.

[2] K Ishizu, T Mukai, Y Yonekura, M Pagani, T Fujita, N Tamaki, H Shibasaki, and J Konishi. Ultra-high-resolution SPECT system using four pinhole collimators for small animal studies. *J. Nucl. Med.*, 26:2282–2289, 1995.

[3] D A Weber and M Ivanovic. Ultra-high-resolution imaging of small animals: implications for preclinical and research studies. *J. Nucl. Card.*, 6:332–344, 1999.

[4] M C Wu, H R Tang, D W Gao, A Ido, J W O'Connell, B H Hasegawa, and M W Dae. ECG gated pinhole SPECT in mice with millimeter resolution. *IEEE Trans. Nucl. Sci.*, 47:1218–1227, 2000.

[5] J B A Habraken, K de Bruin, M Shehata, J Booij, R Bennink, B L van Eck Smit, and E Busemann Sokole. Evaluation of high-resolution pinhole SPECT using a small rotating animal. *J. Nucl. Med.*, 42:1863–1869, 2001.

[6] D P McElroy, L R MacDonald, F J Beekman, Y Wang, B E Patt, J S Iwanczyk, B M W Tsui, and E J Hoffman. Performance evaluation of A-SPECT: A high resolution desktop pinhole SPECT system for imaging small animals. *IEEE Trans. Nucl. Sci.*, 49:2139–2147, 2002.

[7] Z Liu, G A Kastis, G D Stevenson, H H Barrett, L R Furenlid, M A Kupinski, D D Patton, and D W Wilson. Quantitative analysis of acute myocardial infarct in rat hearts with ischemia-reperfusion using a high-resolution stationary SPECT system. *J. Nucl. Med.*, 43:474–480, 2002.

[8] M A King, P H Pretorius, T Farncombe, and F J Beekman. Introduction to the physics of molecular imaging with radioactive tracers in small animals. *Journal of cellular biochemistry*, Suppl. 39:221–230, 2002.

[9] N U Schramm, G Ebel, U Engeland, T Schurrat, M Béhé, and T M Behr. High-resolution SPECT using multipinhole collimation. *IEEE Trans. Nucl. Sci.*, 50:315–320, 2003.

[10] F J Beekman, D P McElroy, F Berger, S S Gambhir, E J Hoffman, and S R Cherry. Towards in vivo nuclear microscopy: I-125 imaging in mice using micro-pinholes. *Eur. J. Nucl. Med.*, 2002.

[11] R K Rowe, J N Aarsvold, H H Barrett, J C Chen, W P Klein, B A Moore, I W Pang, D D Patton, and T A White. A stationary hemispherical SPECT imager for three-dimensional brain imaging. *J. Nucl. Med.*, 34:474–480, 1993.

[12] G K Kastis, H B Barber, H H Barrett, H C Gifford, I W Pang, D D Patton, G Stevenson, and D W Wilson. High resolution SPECT imager for three-dimensional imaging of small animals (abstract). *J. Nucl. Med.*, 39:9P, 1998.

[13] F J Beekman and B Vastenhouw. Design and simulation of U-SPECT, an ultra-high resolution molecular imaging system. *Conference Proceeding of 2002 IEEE Nuclear Science Symposium and Medical Imaging Conference, Norfolk, USA*, 2002.

[14] F J Beekman, A P Colijn, B Vastenhouw, V M Wiegant, and M A F M Gerrits. High-resolution emission tomography of small laboratory animals: physics and gamma-astronomy meet molecular biology. *Nuclear Instruments and Methods in Physics Research Section A: Accelerators, Spectrometers, Detectors and Associated Equipment*, 509 (1-3):229–234, 2003.

[15] B M W Tsui. *Collimator design, properties and charateristics. In* The Scintillation Camera G. H. Simmons. The Society of Nuclear Medicine, New York, 1988.

[16] M F Smith and R J Jaszczak. The effect of gamma ray penetration on angle-dependent sensitivity for pinhole collimation in nuclear medicine. *Med. Phys.*, 24:1701–1709, 1997.

[17] S D Metzler, J E Bowsher, M F Smith, and R J Jaszczak. Analytic determination of pinhole collimator sensitivity with penetration. *IEEE Trans. Med. Im.*, 20:730–741, 2001.

[18] S D Metzler, J E Bowsher, K L Geer, and R J Jaszczak. Analytic determination of the pinhole collimator's point-spread function and rms resolution with penetration. *IEEE Trans. Med. Im.*, 21:878–887, 2002.

[19] M Gieles, H W A M de Jong, and F J Beekman. Accelerated Monte Carlo simulation of micro-pinhole imaging using Kernel Forced Detection. *Phys.Med.Biol.*, 47:1853–1867, 2002.

[20] H M Deloar, H Watabe, T Aoi, and H Iida. Evaluation of penetration and scattering components in conventional pinhole SPECT: phantom studies using Monte Carlo simulation. *Phys. Med. Biol.*, 48:995–1008, 2003.

[21] H O Anger. *Radioisotope cameras*, volume 1, pages 485–552. Academic, New York, 1967. G. J. Hine Ed.

[22] D Paix. Pinhole imaging of gamma rays. *Phys. Med. Biol.*, 12(4):489–500, 1967.

[23] CERN. *GEANT4 Home Page. http://geant4.web.cern.ch/geant4*.

[24] S Agostinelli, J Allison, K Amako, and Apostolakis, J et al. GEANT4—a simulation toolkit. *Nuclear Instruments & Methods in Physics Research A*, 506:250–303, 2003.

[25] A Likar, T Vidmar, and B Pucelj. Monte Carlo determination of gamma-ray dose rate with the GEANT system. *Health Physics*, 75:165–169, 1998.

[26] J Stepanek, H Blattmann, and Laissue, J A et al. Physics study of microbeam radiation therapy with PSI-version of Monte Carlo code GEANT as a new computational tool. *Med. Phys.*, 27:1664–1675, 2000.

[27] N Colonna and S Altieri. Simulations of neutron transport at low energy: A comparison between GEANT and MCNP. *Health Physics*, 82:840–846, 2002.

[28] R Tascherau, R Roy, and J Pouliot. Relative biological effectiveness enhancement of a 125I brachytherapy seed with characteristic X rays from its constitutive materials. *Med. Phys.*, 29:1397–1402, 2002.

[29] S Staelens, D Strul, G Santin, S Vandenberghe, M Koole, Y D'Asseler, I Lemahieu, and R Van de Walle. Monte Carlo simulations of a scintillation camera using GATE: validation and application modelling. *Phys. Med. Biol.*, 48:3021–3042, 2003.

[30] G Santin, D Strul, D Lazaro, L Simon, M Krieguer, M V Martins, V Breton, and C Morel. GATE: A Geant4-based simulation platform for PET and SPECT integrating movement and time management. *IEEE Trans. Nucl. Sci.*, 50(5):1516–1521, 2003.

[31] M J Berger, J H Hubbell, S M Seltzer, J S Coursey, and D S Zucker. *National Institute of Standards and Technology, XCOM: Photon Cross Section Database*. Gaithersburg, MD, 1999.

[32] C E Floyd, R J Jaszczak, K L Greer, and R E Coleman. Inverse Monte Carlo as a unified reconstruction algorithm for ECT. *J. Nucl. Med.*, 27:1577–1585, 1986.

[33] F J Beekman, C Kamphuis, and M A Viergever. Improved quantitation in SPECT imaging using fully 3D iterative spatially variant scatter compensation. *IEEE Trans. Med. Im.*, 15:491–499, 1996.

[34] E C Frey and B M W Tsui. A new method for modelling the spatially variant object dependent scatter response function in SPECT. *1996 IEEE Nuclear Science Symposium Conference Record, Anaheim, CA, November 1996*, pages 1082–1086, 1996.

[35] B M W Tsui, E C Frey, K J LaCroix, D S Lalush, W H McCarthy, M A King, and G T Gullberg. Quantitative myocardial perfusion SPECT. *J. Nucl. Card.*, 5:507–522, 1998.

[36] F J Beekman, H W A M de Jong, and S van Geloven. Efficient fully 3D iterative SPECT reconstruction with Monte Carlo based scatter compensation. *IEEE Trans. Med. Im.*, 21(8):867–877, 2002.

[37] R J Jaszczak, K L Greer, and C E Floyd. Improved SPECT quantification using compensation for scattered photons. *J. Nucl. Med.*, 25:893–900, 1984.

[38] K Ogawa, Y Harata, and T Ichihara. A practical method for position-dependent Compton-scatter correction in Single Photon Emission CT. *IEEE Trans. Med. Im.*, 10:408–412, 1991.

[39] M A King, G J Hademenos, and S J Glick. A dual photopeak window method for scatter correction. *J. Nucl. Med.*, 33:605–612, 1992.

[40] I Buvat, M Rodriquez-Villafuerte, A Todd-Pokropek, H Benali, and R Di Paola. Comparative assessment of nine scatter correction methods based on spectral analysis using Monte Carlo simulations. *J. Nucl. Med.*, 36(8):1476–1488, 1995.

Chapter 4

Penetration, scatter and sensitivity in channel micro-pinholes for SPECT: a Monte Carlo investigation

F van der Have and F J Beekman
IEEE Trans Nucl Sci 2006; 53(5): 2635–2645.

Abstract

Channel-edge pinhole designs have been proposed in order to reduce the penetration of gamma rays through the edge of the pinhole aperture. A characterization of penetration and scatter in the pinhole aperture metal can be used in the design of small animal SPECT collimators or for model based corrections during micro-SPECT image reconstruction.

In this study the penetration and scatter contributions of micro-pinholes were compared for Tc-99m, I-123, and I-125 for knife-edges and channel-edges. To this end, Geant 4 Monte Carlo simulations of 0.3 mm and 0.5 mm diameter apertures with acceptance angles ranging from 20 to 60 degrees were performed.

At perpendicular incidence of the photons, channel pinholes had lower penetration and scatter fractions than did knife-edge pinholes. This advantage disappeared at higher angles

Figure 4.1: Cylindrical collimator of the U-SPECT-I system, equipped with 75 gold micro-pinholes with an acceptance angle of 30 °. In color print in the appendix.

of incidence. In addition, the total sensitivity decreased substantially with increasing channel height.

Planar projection images of a grid of spheres showed that channel edge pinholes resulted in a slightly higher spatial resolution than knife-edge pinholes with an equal diameter, when combined with a high-resolution detector. However, the channel pinhole's sensitivity and Contrast Inverse Coefficient of Variation were lower than the knife edge pinhole's at the edges of the detector. We conclude that channel pinholes can result in lower imaging performance when used with non-perpendicular incidence photons because of loss of sensitivity.

4.1 Introduction

SPECT permits *in vivo* cross-sectional imaging of radio-labeled molecules. Pinhole SPECT is particularly suitable for use with small animals because it can achieve an excellent resolution sensitivity trade-off in small objects [1–12]. High-resolution small animal imaging involving the use of micro-pinholes is rapidly gaining in popularity [13–16]. Most pinhole SPECT systems are based on scintillation cameras with an intrinsic resolution of approximately 2–3 mm. In order to obtain sufficient resolution, strong projection magnification is required to avoid blurring effects due to the intrinsic camera resolution. New SPECT geometries permit more cameras to be placed around the object and systems with tens up to hundreds of pinholes have been proposed [13–15, 17].

Gold is an interesting material to use for manufacturing micro-pinholes since it has both a high atomic number and a high density, is easy to machine and not radio-active. Gold pinholes can be used in planar [16] and SPECT imaging [18–20]. Gold was also used in the U-SPECT-I system [15], a stationary system with 75 gold aperture pinholes. Its collimator cylinder is

shown in Fig. 4.1. The 75 pinhole inserts, where high stopping power is important, are made of gold. The cylinder itself, however, was made of tungsten to reduce the total collimator costs. With the latest version of the software, image resolutions of 0.45 and 0.35 mm can be obtained with 0.6 and 0.3 mm diameter pinholes, respectively [15, 21].

The increased sensitivity arising from a large number of pinholes can be traded for higher resolution by reducing the pinhole diameter. However, even with high stopping-power materials, these micro-pinholes have much higher relative amounts of penetrated and scattered photons than larger diameter pinholes. Effects of penetration [22–24] and scatter [25, 26] have been characterized, but mainly for knife-edge pinholes and perpendicular incidence. We here investigate whether these detrimental effects can be reduced by a pinhole geometry containing a channel (sometimes also called "keel-edge"), instead of a knife-edge [16,27,28]. So far, results on channel pinholes have not specifically focused on the amounts of penetrated and scattered photons at varying angles of incidence and with small pinhole acceptance angles. The major goal of this paper is to provide characteristics regarding the penetration and scattering of photons in channel pinhole apertures with different channel heights. Results are presented for three isotopes (I-125, Tc-99m, and I-123) and for varying angle of incidence and varying pinhole acceptance angle.

4.2 Methods

Amounts of penetration and scatter were calculated by Monte Carlo simulation. Monte Carlo simulation is a very suitable technique to do this since the underlying physics for particle transport is well known. In nuclear medicine, Monte Carlo simulation is a well-established technique for the simulation of photon transport [29]. Its disadvantage is that long computation times are often required in order to simulate the many millions of random events needed to achieve a sufficiently low noise level.

The Monte Carlo code used for this paper was Geant [30] version 4.5. Geant is an acronym for "GEometry ANd Tracking". It has been developed by CERN and several collaborating groups around the world. Geant is used in high-energy physics, particle physics, dosimetry and radiotherapy [31–34]. It was recently made more user-friendly for and is being used in several nuclear medicine applications [35–37]. The simulations reported in this paper made use of the low-energy extension versions for the photoelectric effect, Compton scattering, Rayleigh scattering, ionization and bremsstrahlung.

A point source was simulated in the geometry illustrated in Fig. 4.2. The simulated isotopes were I-125, Tc-99m, and I-123 with the energy spectrum also including high gamma energies with low incidence. The point source was placed at different positions along the line

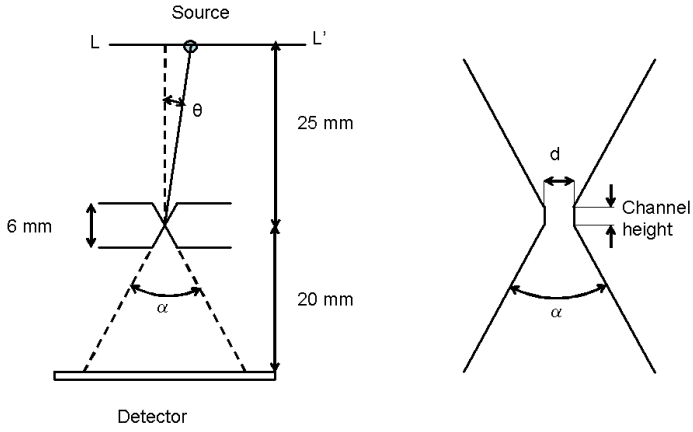

Figure 4.2: The geometry for the Monte Carlo simulations.

L-L' so that the angle of incidence (θ) could be varied. The pinhole aperture material was gold and the aperture diameters (d) tested were 0.3 mm and 0.5 mm. The total acceptance angle of the pinhole (α) was varied from 20 ° to 60 °.

The simulation distinguished three types of photons: (i) direct photons, defined as those that passed through the pinhole opening, (ii) penetrated photons, defined as those that passed through the pinhole metal without interaction, and (iii) scattered photons, defined as those photons that interacted with the pinhole aperture edge material. The detector was square, measuring 25 mm $\times$ 25 mm, which was somewhat larger (in order to catch scattered photons) than the circumscribed square around the circle where direct photons could hit the detector. The detector's energy resolution was modeled to be energy-dependent, Gaussian-distributed, where the Full Width Half Maximum was 10 % of a photon's energy. Energy windows according to table 4.1 were applied to the simulation results.

The Monte Carlo code was validated by comparing the simulated penetration-to-direct ratio to the analytically predicted value obtained from equations 27 and 31 in the work of

Table 4.1: The energy window settings for the isotopes that were used.

Isotope	Photo-peak (keV)	Window Range (keV)
Tc-99m	140	126–154
I-125	27–35	15–45
I-123	159	139–175

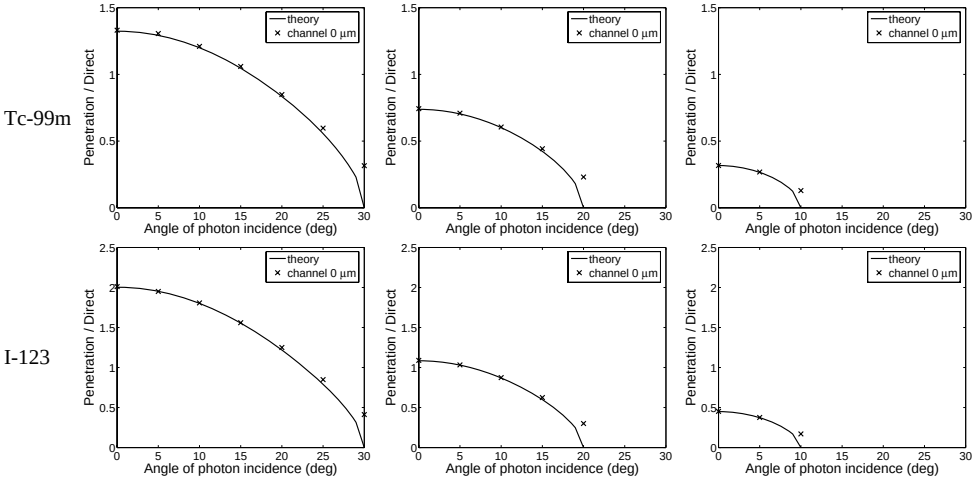

Figure 4.3: The validation for Tc-99m and I-123, pinhole diameter 0.3 mm, acceptance angles 60 °, 40 °, 20 ° (from left to right). The solid lines show the theoretical penetration-to-direct ratio, where the penetrative sensitivity is calculated according to [22]. The cross marks show the corresponding Monte Carlo results.

Metzler *et al.* [22].

The effect of channel pinholes on image quality was investigated in planar images for an extended source distribution consisting of a grid of homogeneously filled spheres. The signal-to-noise ratio was compared between regions-of-interest at the center and at the edge of the image, for both knife-edge and channel pinholes.

4.3 Results and discussion

4.3.1 Validation of the MC code

The validation of the Monte Carlo code versus analytically calculated results for Tc-99m and I-123 is shown in Fig. 4.3. The lines are the theoretical predictions, obtained by dividing $S_{\mathrm{pen}}(\theta)$ from equation 31 in [22] by $S_{\mathrm{geo}}(\theta)$ from equation 2 in [22]. The crosses are Monte Carlo results of the penetration-to-direct ratio. The agreement is good for all angles except for the rightmost part in each figure. This is explained by the difference in assumed geometry: the derivation in [22] assumes an infinite cone as the pinhole shape, while the Monte Carlo simulations were performed for a finite-thickness pinhole insert. In the limit that the angle of incidence approaches the half acceptance angle of the pinhole, the penetration should go to

zero for an infinite cone (as is explained in [22]) but in the case of a finite-thickness pinhole insert, the photons would still be able to go through a small amount of material at the corner where the conical part ends, go through the pinhole opening, and again through a small amount of material at the opposite edge. Considering these differences are understood, and the agreement elsewhere is good, we conclude that the MC results agree with the theoretical prediction.

4.3.2 Simulation of a point source with non-perpendicular incidence

Fig. 4.4 shows the distribution on the detector of the three types of photons at a 30 ° angle of incidence. The images show approximately one quarter of the detector, from the center to the edge where in this case the PSF is located. Since the projection of a circular aperture becomes an ellipse (see also Fig. 4.5) when viewed at an angle, the "direct" component is elliptically shaped. The penetration component was almost completely blocked along the short axis of this ellipse but was not blocked along the long axis. Scattered photons were detected on all of the detector's area.

4.3.3 Ratios of the amount of penetrated and scattered to the amount of direct photons

Figs. 4.6 – 4.11 show, for combinations of several parameters, the ratios of penetrated and of scattered photons to direct photons as well as the effect of a channel in the pinhole on sensitivity. In each of the Figs. 4.6 – 4.11 these ratios are shown, as a function of the angle of photon incidence, in the left and middle column of graphs, respectively and each graph contains data for knife-edge pinholes and pinholes with channel heights of 0.1, 0.2, and 0.3 mm. The top left graphs for I-123(Figs. 4.6 and 4.9) and Tc-99m (Figs. 4.7 and 4.10) show, for example, that at perpendicular incidence using pinholes with the largest acceptance angle (60 °), the ratio of penetrated to direct photons was reduced by typically 60% by the longest channel (0.3 mm) compared to the knife-edge pinhole. The same figures also show that this advantage of channel pinholes disappeared at non-perpendicular incidence. The penetration-to-direct ratio graphs for all the channel heights tended to coincide when the angle of incidence approached the half acceptance angle of the pinhole. The situation for the scatter-to-direct ratio (top middle frames) was similar, although the relative differences between knife edge and channel pinholes were smaller and the reduction by the pinhole with the longest channel with respect to the knife-edge pinhole at perpendicular incidence was typically around 30%.

The different rows of Figs. 4.6 – 4.11 show the graphs for different acceptance angles

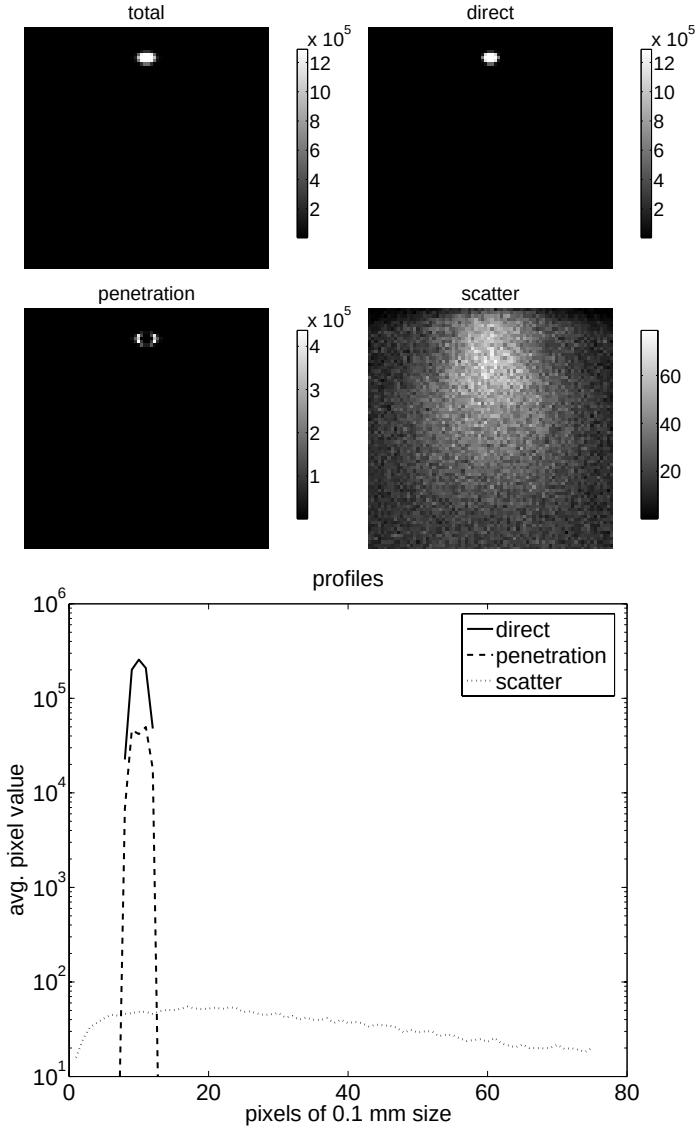

Figure 4.4: Top frames: the distribution of different types of photons on the detector when $\theta = 30\,^{\circ}$, $\alpha = 60\ ^{\circ}$, the channel height was 0.15 mm, with a Tc-99m point source. Bottom: associated vertical image profiles. These were averaged over the central one third of the images shown on a semilogarithmic scale.

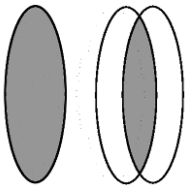

Figure 4.5: The aperture of a knife-edge pinhole reduces to an ellipse when viewed at an angle, the aperture of a channel pinhole reduces to the intersection of two ellipses.

of the pinhole(60 °, 40 °, and 20 °). The shape of the graphs is approximately the same. One thing to notice is that the effect of increasing channel height on the penetration-to-direct and scatter-to-direct ratios was less pronounced when the acceptance angle became smaller. Another, perhaps more important, observation is that the pinhole acceptance angle had a large impact on the ratios of the number of penetrated and scattered to the number of direct photons. For the ranges of acceptance angle and channel height that we simulated, the effect of a lower acceptance angle on the amounts of penetration and scatter was stronger than the effect of adding the longest channel. It seems appropriate that, when choosing a pinhole collimator design, one should first make sure the acceptance angle is as small as the geometrical design of the set-up allows and only then be concerned with the seemingly less important choice of knife-edge or channel pinhole.

Channel pinholes also had a lower total counting sensitivity than did knife-edge pinholes and the decrease of sensitivity depended on the angle of incidence. The third column of Figs. 4.6 – 4.11 shows the decrease of sensitivity of channel pinholes with increasing channel height normalized to a knife-edge pinhole. The normalization means that the decrease in sensitivity that a knife-edge pinhole had when the source was moved along the line L-L', has already been divided out. Channel pinholes with the highest pinhole acceptance angle yielded the lowest relative sensitivity, i.e. the largest decrease in sensitivity with respect to the corresponding knife-edge pinhole. The most extreme decrease is seen at the top right in Figs. 4.6 – 4.8 (all isotopes, 0.3 mm diameter, α=60 °), the channel pinhole's sensitivity dropped to 50% relative to a knife-edge pinhole when the incidence angle θ approached the half acceptance angle (30 °) and the channel height was two thirds of the pinhole diameter; the sensitivity dropped to 30% for a channel height equal to the aperture diameter. The decrease in sensitivity was less dramatic for 0.5 mm diameter pinholes with the same absolute channel heights and also for smaller acceptance angles. The channel pinhole's lower sensitivity is explained in Fig. 4.5. When viewed at an angle, the circular aperture of a knife-edge pinhole becomes an ellipse. In the case of a channel pinhole, the two circles delimiting the

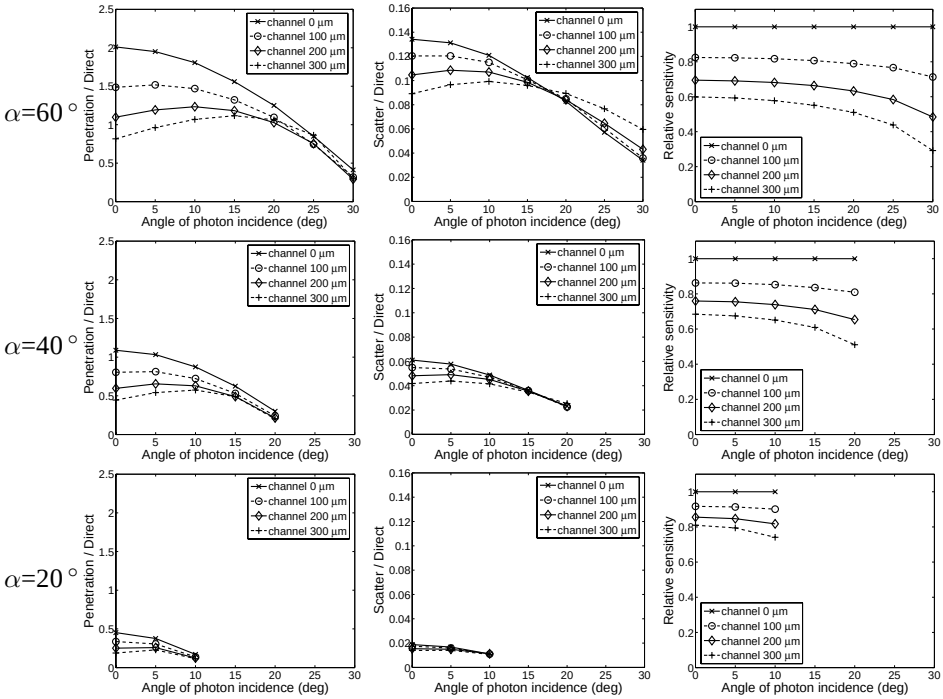

Figure 4.6: For I-123 with 0.3 mm pinholes: the penetration-to-direct (left column) and scatter-to-direct (middle column) ratios as a function of the angle of incidence (θ). The right column shows the total counting sensitivity, normalized to a knife-edge pinhole. The pinhole acceptance angle was 60 °, 40 °, and 20 ° (from top to bottom).

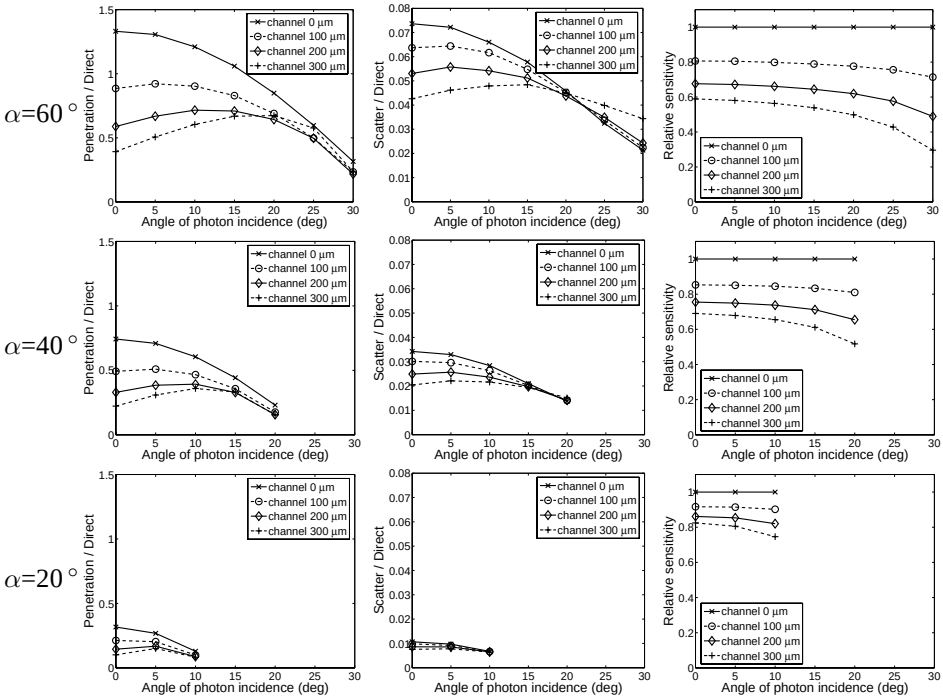

Figure 4.7: Like Fig. 4.6 but for Tc-99m with 0.3 mm pinholes.

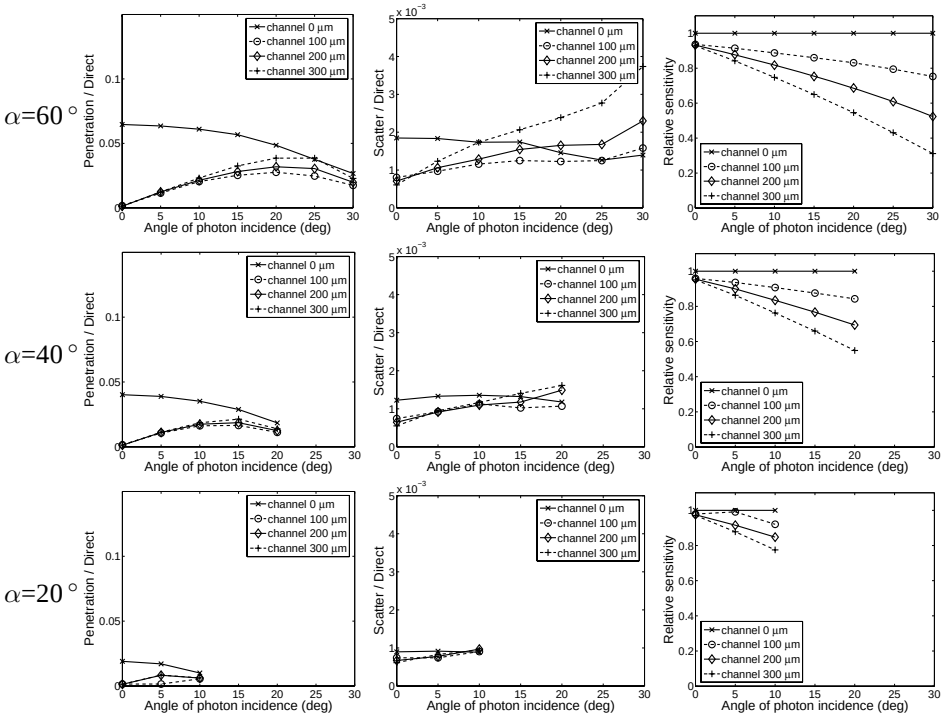

Figure 4.8: Like Fig. 4.6 but for I-125 with 0.3 mm pinholes.

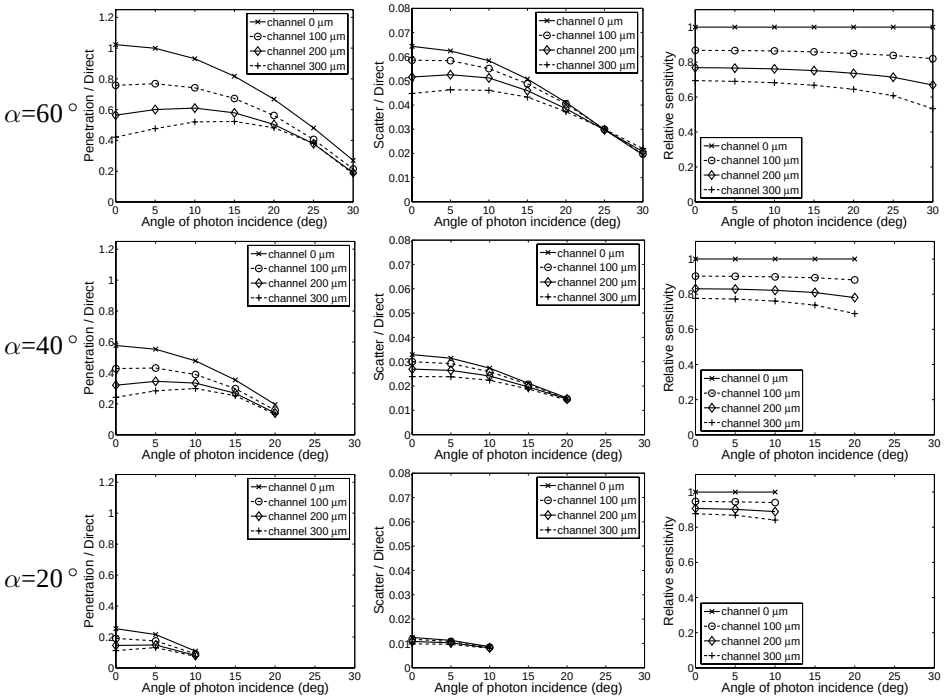

Figure 4.9: Like Fig. 4.6 but for I-123 with 0.5 mm pinholes.

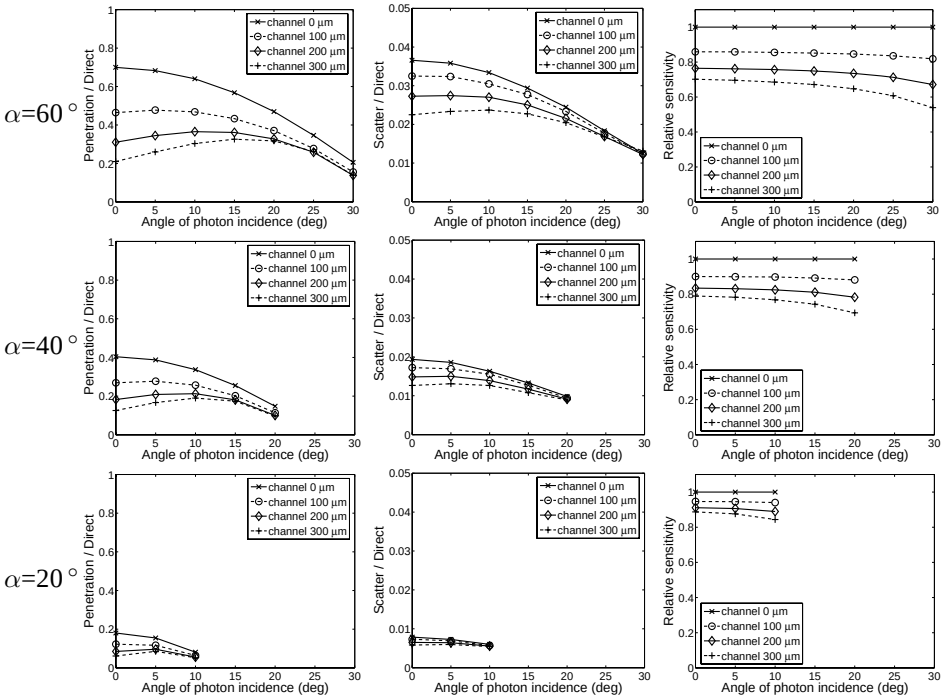

Figure 4.10: Like Fig. 4.6 but for Tc-99m with 0.5 mm pinholes.

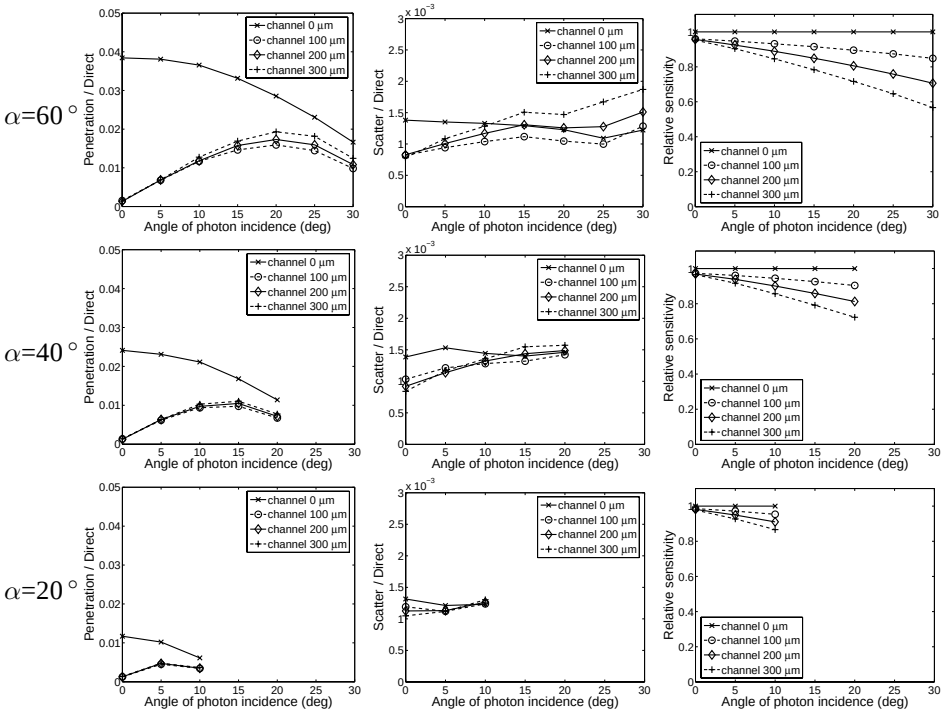

Figure 4.11: Like Fig. 4.6 but for I-125 with 0.5 mm pinholes.

channel become two non-concentric ellipses and the effective opening is reduced to only the intersection.

When the differences between the different isotopes (energies) are investigated, the general trend seems to be that the figures for Tc-99m and I-123 have the same qualitative appearance, the difference is mostly a scaling. The penetration-to-direct and scatter-to-direct ratios for I-123 were a factor 1.2 to 2 higher than those for Tc-99m, while the normalized sensitivity (channel pinholes with respect to knife-edge pinholes) was virtually identical. The graphs for I-125 (Figs. 4.8 and 4.11) have a different appearance. The first thing to note with I-125 is that the effects of penetration and scatter overall are small. It is possible that penetration and scatter effects would be insignificant in real applications. The data shows that the small amount of penetration that was left at perpendicular incidence with a knife-edge pinhole, could be completely removed already by a channel pinhole with a small channel height. With increasing pinhole angle, the penetration-to-direct and scatter-to-direct ratios converge to the same values for all channel heights, like with Tc-99m and I-123. The normalized sensitivity of the channel pinholes with I-125 drops to a similar fraction as with I-123 and Tc-99m when the angle of incidence approaches the half acceptance angle, although the decrease is more linear in the case of I-125.

The effect of the pinhole diameter (0.5 mm vs. 0.3 mm) can be seen by comparing Figs. 4.6 – 4.8 to the corresponding Figs. 4.9 – 4.11. The penetration-to-direct and scatter-to-direct ratios are about half in magnitude for 0.5 mm pinholes with respect to 0.3 mm pinholes. This general result was obtained for all pinhole acceptance angles and all three isotopes, with some minor exceptions in case of I-125. The normalized sensitivity drops in the same way for 0.5 mm pinholes as for 0.3 mm pinholes, but not as dramatically.

The effects of the different parameters can be summarized as follows:

- Angle of incidence. When the angle of incidence increased, the channel pinhole's advantage of lower penetration and scatter disappeared. Furthermore, the channel pinhole's sensitivity decreased more than a knife-edge pinhole's, up to 2.5 times as much for high angles of incidence and small pinhole diameter (0.3 mm).

- Acceptance angle. Pinholes with smaller acceptance angles had much lower penetration and scatter contributions. This effect seems strong relative to the effect of a channel pinhole versus a knife-edge pinhole.

- Isotope/energy. The lowest-energy isotope (I-125) yielded low penetration and scatter contributions overall. The penetration-to-direct and scatter-to-direct ratios for I-123 were up to 2 times higher than for Tc-99m.

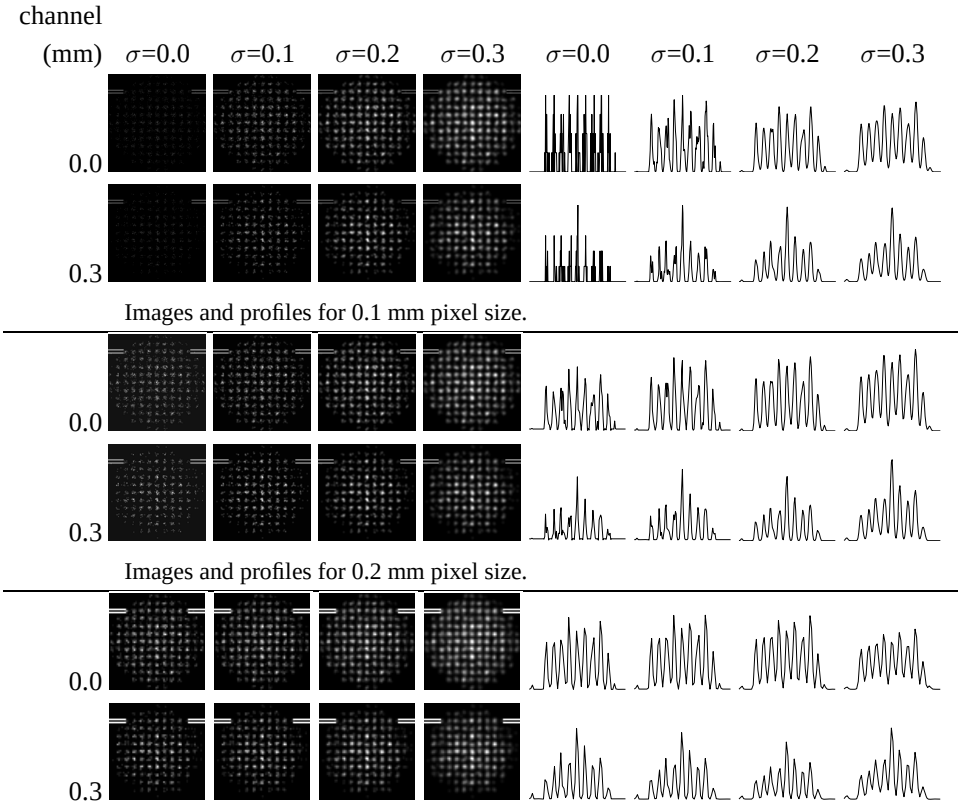

Figure 4.12: Planar images of a square grid of homogeneous spheres of Tc-99m. The acceptance angle was 60 degrees, the channel height was varied from knife edge (0 mm) to 0.3 mm. The resulting images were blurred with Gaussian kernels with an increasing width, where σ is expressed in mm. Top: 0.1 mm pixel size, middle: 0.2 mm pixel size, bottom: 0.4 mm pixel size.

- Pinhole diameter. The penetration-to-direct and scatter-to-direct ratios were higher by about a factor of 2 for 0.3 mm pinholes compared to 0.5 mm pinholes.

4.3.4 Planar images of an extended source

The effect of a knife edge versus a channel edge pinhole on the image of an extended activity distribution and the task to reproduce contrast were also investigated for a pixelated detector. The simulated Tc-99m activity distribution was a square grid of homogeneous spheres of ac-

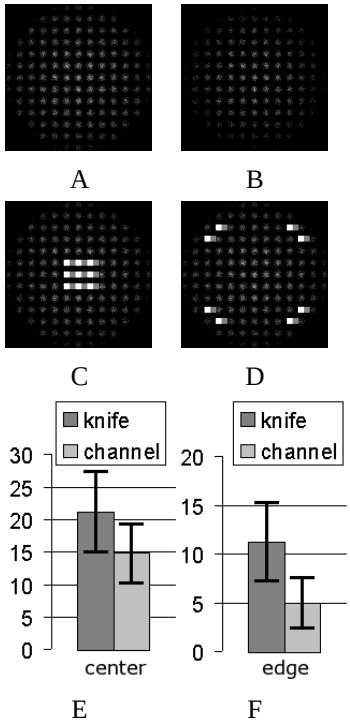

Figure 4.13: Image analysis comparing knife-edge with 0.3 mm channel pinholes. A) knife-edge summed image over 10 noise realizations, B) channel pinhole summed image over 10 noise realizations, C) locations where the contrast was measured for the central region, one contrast value is the difference between the intensity in a region marked in white and an adjacent background region marked in grey, D) like C, but for the edge region, E) representation of the mean and standard deviation levels of the contrast for the central region, calculated across the different locations and 10 noise realizations, F) Like E, but for the edge region.

tivity in a plane parallel to the detector, and perpendicular to the pinhole's axis. The diameter of the spheres was 1.25 mm and the center-to-center distance was 2.5 mm. The detector was simulated having pixel sizes of 0.1, 0.2, and 0.4 mm. The images based on counts within the Tc-99m energy window from this simulation are shown in the left part of Fig. 4.12. Profiles through the second row (profile position indicated in white) from the top of the projection images are shown in the right half of Fig. 4.12. The simulated channel heights were 0 and 0.3 mm. The simulations had an equal number of photons emitted from the spheres. Channel pinholes have a lower sensitivity but provide a higher resolution radiation pattern on the detector surface. The images are all presented at different low-pass filtering settings, expressed in the σ determining the width of the Gaussian filter used.

The image and profile for the case of the smallest pixel size and no blurring demonstrated that the channel pinhole resulted in a higher resolution, in the sense that the projections from different spheres were better separated in the profile. However, when either the blurring level or the pixel size was increased, this resolution advantage was no longer seen. The most apparent disadvantage of the channel pinhole was that, towards the edges of the field of view on the detector, the intensity of the projections dropped much more for channel edge than for knife edge pinholes, yielding a noisier image.

In order to measure the difference in contrast between the knife edge and 0.3 mm channel pinholes in the case of small pixels and without blurring from Fig. 4.12, ten different noise realizations were computed for these situations. We define the contrast as the difference in signal intensity between one of the areas marked in white and the adjacent area marked in grey in Fig. 4.12. This contrast was calculated in each of the nine positions in the central or eight position in the edge areas for each of the noise realisations, and the contrast's mean and standard deviation was calculated across the resulting 80 or 90 values. The "Contrast Inverse Coefficient of Variation"(CICOV) was then calculated as the mean contrast divided by the standard deviation in the contrast. This CICOV should increase when the resolution is better, because of better separation between the "signal" and "background" areas, and it should decrease when the sensitivity is lower, because that increases noise and therefore the standard deviation. The values obtained are shown in Table 4.2 and as a bar chart with error bars in Fig. 4.13. The CICOV was almost equal for the channel pinhole and the knife-edge pinhole in the central area: we attribute this as the net outcome of a higher resolution counteracting the lower sensitivity for the channel pinhole. The CICOV was significantly higher for the knife-edge pinhole than for the channel in the edge of the image: we attribute this difference to the (much) poorer sensitivity of the channel pinhole relative to the knife-edge in that area.

Table 4.2: The Contrast Inverse Coefficient of Variation (CICOV) of knife-edge versus channel pinhole images of an extended source.

Central				
	contrast mean	contrast variance	contrast stddev	CICOV
knife edge	21.2	37.4	6.11	3.47
channel 0.3 mm	14.8	20.6	4.54	3.27

Edge				
	contrast mean	contrast variance	contrast stddev	CICOV
knife edge	11.3	15.5	3.94	2.87
channel 0.3 mm	5.04	6.64	2.58	1.95

4.4 Conclusion

This paper presented results from Monte Carlo simulations on the performance of channel edge and knife edge pinholes for isotopes, channel heights, pinhole diameters, and acceptance angles, that could be used in multi-pinhole stationary SPECT systems. Channel-edge pinholes can have advantages of relatively lower penetration and scattering contributions to the total photon count, when used at perpendicular photon incidence. This advantage can disappear, however, if the angle of incidence approaches the half cone acceptance angle of the pinhole. The most important disadvantage of channel pinholes was that they had a lower total counting sensitivity than did knife-edge pinholes and that with increasing angle of incidence the counting sensitivity decreased faster than it did for knife edge pinholes. We think that in many cases, choosing the smallest possible pinhole acceptance angle will be at least as influential as adding a pinhole channel for penetration and scatter reduction, without having to deal with the drawbacks of channel pinholes. The planar images of an extended source distribution and Contrast Inverse Coefficient of Variation calculation demonstrated that the resolution of channel edge pinholes was higher, but this could only be exploited in combination with a high-resolution detector. The CICOV was found to be approximately equal between knife-edge and channel pinholes in the central areas of the projection image, and higher for the knife-edge than for the channel pinhole at the edges of the field of view.

Bibliography

[1] R. J. Jaszczak, J. Li, H. Wang, M. R. Zalutsky and R. E. Coleman, *Pinhole collimation for Ultra-high-resolution small-field-of-view SPECT*, Phys. Med. Biol., vol. 39, pp. 425–37, 1994.

[2] K. Ishizu, T. Mukai, Y. Yonekura, M. Pagani, T. Fujita, N. Tamaki *et al.*, *Ultra-high-resolution SPECT system using four pinhole collimators for small animal studies*, J. Nucl. Med., vol. 26, pp. 2282–2289, 1995.

[3] D. A. Weber, M. Ivanovic, D. Franceschi, S-E. Strand, K. Erlandsson, M. Franceschi *et al.*, *Pinhole SPECT: an approach to in vivo high resolution SPECT imaging in small laboratory animals*, J. Nucl. Med., vol. 35, pp. 342–348, 1993.

[4] M. C. Wu, H. R. Tang, D. W. Gao, A. Ido, J. W. O'Connell, B. H. Hasegawa *et al.*, *ECG gated Pinhole SPECT in Mice with Millimeter Resolution*, IEEE Trans. Nucl. Sci., vol. 47, pp. 1218–1227, 2000.

[5] S. R. Meikle, R. R. Fulton, S. Eberl, M. Dahlbom, K. P. Wong and M. J. Fulham, *An investigation of coded aperture imaging for small animal SPECT*, IEEE Trans. Nucl. Sci., vol. 48, pp. 816–821, 2001.

[6] D. P. McElroy, L. R. MacDonald, F. J. Beekman, Y. Wang, B. E. Patt, J. S. Iwanczyk *et al.*, *Performance Evaluation of A-SPECT: A High Resolution Desktop Pinhole SPECT System for Imaging Small Animals*, IEEE Trans. Nucl. Sci., vol. 49, pp. 2139–2147, 2002.

[7] S. Meikle, *Small animal SPECT and its place in the matrix of molecular imaging technologies*, Phys. Med. Biol., vol. 50, In Press, 2005.

[8] A. L. Goertzen, D. W. Jones, J. Seidel, K. Li, and M. V. Green, *First results from the high-resolution mouseSPECT annular scintillation camera*, IEEE Trans. Med. Im., vol. 24(7), pp. 853–867, 2005.

[9] S. D. Metzler, R. J. Jaszczak, N. H. Patil, S. Vemulapalli, G. Akabani, and B. B. Chin, *Molecular imaging of small animals with a triple-head SPECT system using pinhole collimation*, IEEE Trans. Med. Im., vol. 24(7), pp. 853–862, 2005.

[10] A. G. Weisenberger, S. S. Gleason, J. Goddard *et al.*, *A restraint-free small animal SPECT imaging system with motion tracking* IEEE Trans. Nucl. Sci., vol. 52(3), pp. 638–644, 2005.

[11] B. M. W. Tsui, and Y. C. Wang, *High-resolution molecular imaging techniques for cardiovascular research* J. Nucl. Cardiol., vol 12(3), pp. 261–267, 2005.

[12] C. Lackas, N. U. Schramm, J. W. Hoppin *et al. T-SPECT: A novel imaging technique for small animal research* IEEE Trans. Nucl. Sci., vol. 52(1), pp. 181–187, 2005.

[13] Z. Liu, G. A. Kastis, G. D. Stevenson, H. H. Barrett, L. R. Furenlid, M. A. Kupinski *et al., Quantitative analysis of acute myocardial infarct in rat hearts with ischemia-reperfusion using a high-resolution stationary SPECT system*, J. Nucl. Med., vol. 43, pp. 933–939, 2002.

[14] F. J. Beekman and B. Vastenhouw, *Design and simulation of a high-resolution stationary SPECT system for small animals*, Phys. Med. Biol. vol. 49, pp. 4579–4592, 2004.

[15] F. J. Beekman, F. van der Have, B. Vastenhouw, A. J. A. van der Linden, P. P. van Rijk, J. P. H. Burbach, and M. P. Smidt", *U-SPECT-I: A Novel System for Submillimeter-Resolution Tomography with Radiolabeled Molecules in Mice*, J. Nucl. Med., vol. 46(7), pp. 1194–1200, 2005.

[16] F. J. Beekman, D. .P. McElroy, F. Berger, S. S. Gambhir, E. J. Hoffman and S. R. Cherry, *Towards in vivo nuclear microscopy: I-125 imaging in mice using micro-pinholes*, Eur. J. Nucl. Med. Mol. Im., vol. 29, pp. 933–938, 2002.

[17] R. K. Rowe, J. N. Aarsvold, H. H. Barrett, J. C. Chen, W. P. Klein, B. A. Moore, *et al., A stationary hemispherical SPECT imager for three-dimensional brain imaging*, J. Nucl. Med., vol. 34, pp. 474–480, 1993.

[18] C. R. Tenney, *Performance measurements for gold pinholes for small animal SPECT imaging applications*, J. Nucl. Med., vol. 43, p. 917 Suppl., May 2002.

[19] T. F. Peterson, H. Kim, M. J. Crawford, B. M. Gershman, W. C. J. Hunter, H. .B. Barber *et al., SemiSPECT: a small-animal imaging system based on eight CdZnTe pixel detectors*, IEEE Nuclear Science Symposium Conference Record, vol. 3, pp 1844–1847, November 2002.

[20] L. R. Furenlid, D. W. Wilson, Y. C. Chen, H. Kim, P. J. Pietraski, M. J. Crawford *et al., FastSPECT II: A Second-Generation High-Resolution Dynamic SPECT Imager*, IEEE Trans. Nucl. Sci., vol. 51, pp. 631–635, 2004.

[21] F. van der Have, B. Vastenhouw, and F. J. Beekman, *System Calibration and Statistical Image Reconstruction for the U-SPECT-I Stationary Pinhole System* Conference Record of the IEEE NSS/MIC, Puerto Rico, 2005.

[22] S. D. Metzler, J. E. Bowsher, M. F. Smith, and R. J. Jaszczak *Analytic Determination of Pinhole Collimator Sensitivity with Penetration*, IEEE Trans. Med. Im., vol. 20, pp. 730–741, 2001.

[23] S. D. Metzler, J. E. Bowsher, K. L. Greer, and R. J. Jaszczak *Analytic determination of the pinhole collimator's point-spread function and RMS resolution with penetration* IEEE Trans. Med. Im., vol. 21, pp. 878–887, 2002.

[24] M. F. Smith and R. J. Jaszczak, *An analytic model of pinhole aperture penetration for 3D pinhole SPECT image reconstruction* Phys. Med. Biol., vol. 43, pp. 761–775, 1998.

[25] H. M. Deloar, H. Watabe, T. Aoi and H. Iida, *Evaluation of penetration and scattering components in conventional pinhole SPECT: phantom studies using Monte Carlo simulation*, Phys. Med. Biol., vol. 48, pp. 995–1008, 2003.

[26] F. van der Have and F. J. Beekman, *Photon penetration and scatter in micro-pinhole imaging: a Monte Carlo investigation*, Phys. Med. Biol., vol. 49, pp. 1369–1386, 2004.

[27] M. F. Smith, R. J. Jaszczak, and H. Wang, *Pinhole aperture design for 131I tumor imaging*, IEEE Trans. Nucl. Sci., vol. 44, pp. 1154–1160, 1997.

[28] T. Y. Song, Y. Choi, Y. H. Chung, J. H. Jung, Y. S. Choe, K.-H. Lee, *et al.*, *Optimization of pinhole collimator for small animal SPECT using Monte Carlo simulation*, IEEE Trans. Nucl. Sci, vol. 50, pp. 327–332, 2003.

[29] H. Zaidi, *Relevance of accurate Monte Carlo modeling in nuclear medical imaging*, Med. Phys., vol. 26, pp. 574–608, 1999.

[30] S. Agostinelli, J. Allison, K. Amako, J. Apostolakis, H. Araujo, P. Arce *et al.*, *GEANT4 - a simulation toolkit*, Nucl. Instrum. Methods Phys. Res. A, vol. 506, pp. 250–303, 2003.

[31] J. Stepanek, H. Blattmann,J. A. Laissue *et al.*, *Physics study of microbeam radiation therapy with PSI-version of Monte Carlo code GEANT as a new computational tool*, Med. Phys., vol. 27, pp. 1664–1675, 2000.

[32] A. Likar, T. Vidmar, and B. Pucelj, *Monte Carlo determination of gamma-ray dose rate with the GEANT system*, Health Physics, vol. 75, pp. 165–169, 1998.

[33] N. Colonna and S. Altieri, *Simulations of neutron transport at low energy: A comparison between GEANT and MCNP*, Health Physics, vol. 82, pp. 840–846, 2002.

[34] R. Tascherau, R. Roy, and J. Pouliot, *Relative biological effectiveness enhancement of a 125I brachytherapy seed with characteristic X rays from its constitutive materials*, Med. Phys., vol. 29, pp. 1397–1402.

[35] S. Jan, G. Santin, D. Strul, S. Staelens, K. Assié, D. Autret *et al.*, *GATE: a simulation toolkit for PET and SPECT*, Phys. Med. Biol., vol. 49, pp. 4543–4561, 2004.

[36] S. Staelens, D. Strul, G. Santin, S. Vandenberghe, M. Koole, Y. D'Asseler *et al.*, *Monte Carlo simulations of a scintillation camera using GATE: validation and application modelling*, Phys. Med. Biol., vol. 48, pp. 3021–3042, 2003.

[37] S. Staelens, K. Vunckx, J. De Beenhouwer, F. Beekman, Y. D'Asseler, J. Nuyts, and I. Lemahieu, *GATE simulations for optimization of pinhole imaging*, Nucl. Instr. Meth. A, In Press, 2005.

Chapter 5

Optimizing multi-pinhole SPECT geometries using an analytical model

M C M Rentmeester, F van der Have, and F J Beekman
Phys Med Biol 2007; 52: 2567–2581.

Abstract

State-of-the-art multi-pinhole SPECT devices allow for sub-mm resolution imaging of radiomolecule distributions in small laboratory animals. The optimization of multi-pinhole and detector geometries using simulations based on ray-tracing or Monte Carlo algorithms is time consuming particularly because many system parameters need to be varied. As an efficient alternative we develop a continuous analytical model of a pinhole SPECT system with a stationary detector set-up, which we apply to focused imaging of a mouse. The model assumes that the multi-pinhole collimator and the detector both have the shape of a spherical layer, and uses analytical expressions for effective pinhole diameters, sensitivity, and spatial resolution. For fixed fields-of-view, a pinhole-diameter adapting feedback loop allows for the comparison of the system resolution of different systems at equal system sensitivity, and vice versa. The model predicts that (i) for optimal resolution or sensitivity the collimator layer with pinholes should be placed as closely as possible around the animal given a fixed detector layer, (ii) with high-resolution detectors a resolution improvement up to 31% can be

achieved compared to optimized systems, (iii) high-resolution detectors can be placed close to the collimator without significant resolution losses, (iv) interestingly, systems with a physical pinhole diameter of 0 mm can have an excellent resolution when high-resolution detectors are used.

5.1 Introduction

Dedicated Single Photon Emission Computed Tomography (SPECT) and Positron Emission Tomography (PET) instruments in concert with the radio-labeling of small molecules, antibodies, peptides, and probes for gene expression have facilitated *in vivo* assessment of molecular mechanisms and the development of new tracers and pharmaceuticals. Recent instrumentation developments in this multi-disciplinary field of radio-molecular imaging have initiated a revolution in biomedical sciences. However, improving image resolution is, among other things, essential to fully exploit available disease models and tracers. SPECT systems employing pinhole collimators permit radio-labeled molecule distributions to be imaged *in vivo* in small animals at sub-mm resolution level. Several pinhole SPECT systems, stationary and non-stationary, have been designed and constructed in recent years, e.g., [1–13]. Some overviews and introductions to the subject of small animal SPECT have been published recently, e.g., [14–16].

For gamma-ray detection, a whole spectrum of detectors is available. On one end of this range conventional detectors based on continuous scintillation crystals can be found, typically 10 mm thick NaI, with Photo-Multiplier Tubes (PMTs) exploiting the Anger principle [17]. These detectors typically have an intrinsic resolution of about 3 – 4 mm. Instead of PMTs, various other detection techniques are used and new techniques are being investigated [18]. On the other end of the spectrum are the very high-resolution detectors that can reach resolutions below a hundred μm. Compared to conventional detectors, high-resolution detectors are orders of magnitude more expensive per unit of detector surface, which currently limits their applicability.

Two groups have designed, constructed, and evaluated stationary small animal SPECT systems based on polygonal geometries; the FastSPECT systems of the University of Arizona, e.g. [12, 19], and the U-SPECT systems developed at the University Medical Center Utrecht [11, 13, 16]. The FastSPECT II system consists of a modular 16 camera set-up, based on conventional NaI detectors. In the basic configuration suitable for small-animal imaging, with 1 mm pinholes FastSPECT-II reaches a system resolution of about 2.5 mm and a sensitivity of 0.04% [12]. The first U-SPECT system was based on conventional detectors with an intrinsic resolution of 3.2 mm. Using 0.6 mm pinholes, a reconstructed resolution of

< 0.5 mm can be obtained [20] and a reconstructed resolution of ≤ 0.35 mm is possible using 0.3 mm pinholes [13, 21]. As a result, U-SPECT-I allows for discrimination of molecule concentrations in adjacent volumes as small as about 0.1 microliters (using 0.6 mm pinholes) or 0.04 micro-liters (using 0.3 mm pinholes). A similar stationary system (U-SPECT-III) but with high-resolution detectors ($< 100\mu$m) based on EMCCDs [22] was recently proposed [11]. Other groups are also pursuing the goal of constructing high-resolution SPECT systems based on high-resolution detectors, e.g., [2, 18, 23–27].

The U-SPECT systems are designed in such a way that all pinholes focus on a small volume-of-interest. In this way a specific object area is adequately magnified on the detector plane, while only a limited part of the available detector surface is required for creating each mini pinhole camera. All these cameras together result locally in a very high sensitivity, e.g., 0.22% with 0.6 mm pinholes with U-SPECT-I. The field-of-view can be extended for sub-mm full-body imaging by moving the focus to different positions through translation of the bed [20,28]. This will result in a lower average sensitivity. However, resolutions of ≈ 0.5 mm can still be reached, even when total-body scans are performed with this focusing device.

Optimization studies of SPECT systems are often based on simulations. Simulations based on ray-tracing have been used for studies of complete pinhole systems, e.g. [11, 29], while simulations based on Monte Carlo algorithms were used to study particular aspects of pinhole systems, e.g., [30–36]. These simulations tend to be very time-consuming. The goal of the present paper is (i) to develop an analytical model of stationary multi-pinhole SPECT and (ii) to exploit the model as a guide for optimizing and comparing two classes of focusing pinhole SPECT systems. One class represents systems based on conventional detectors such as U-SPECT-I and FastSPECT. The other represents designs that anticipate the use of gamma cameras with a high resolution detector such as U-SPECT-III [11].

5.2 Methods

The geometry used in the analytical system model that will be employed is shown in the left panel of figure 5.1. Both the detector set-up and collimator are modeled as spherical layers with radii r_d and r_c respectively. In this study all systems that are compared have an equally-sized spherical area with radius r_f in which each point is seen by all pinholes (see the right panel of figure 5.1). This area we denote "central field-of-view" (CFOV). r_f is chosen such that it is large enough to cover the mid-brain or heart of a mouse. The collimator contains knife-edge pinholes with a physical pinhole diameter d and aperture material with an attenuation coefficient μ. The actual number of pinholes that can be employed is determined by the radius of the CFOV, the size of the detector, and the requirement that the projections of

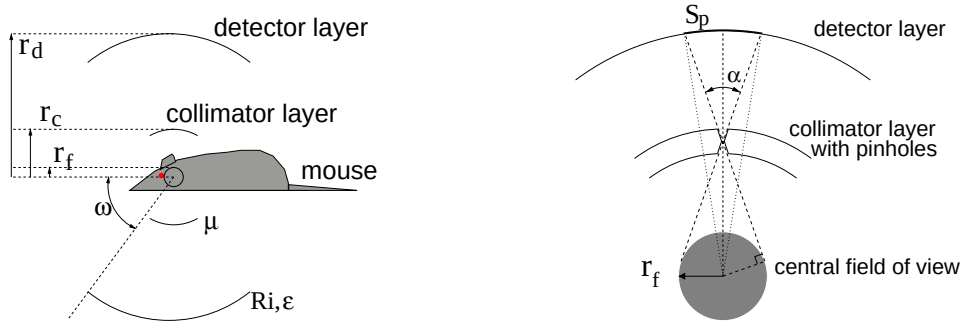

Figure 5.1: Left: Cross section of the spherical layer shells that constitute our SPECT model together with the mouse to be studied. All defining quantities of the model are shown. Right: Projection of the central field-of-view through one pinhole onto the detector. The knife-edge pinholes with pinhole diameter d are shaped in such a way that the central field-of-view is projected without being obstructed by the collimator.

the CFOV on the detector do not overlap. To facilitate numerical optimization, the number of pinholes is a continuous variable, i.e., allowing for non-integer values. The detector scintillation crystals provide an intrinsic resolution R_i, and have a capturing efficiency ε. The opening angle of the detector, ω, is fixed. Together with r_d it determines the size of the detector. The collimator radius r_c is always chosen in such a way that it allows for physical insertion into the detector layer as well as for the insertion of the animal into the collimator. The quantities r_f, r_c, r_d, R_i, μ, ω, ε, and d define the system. In the right panel of figure 5.1 the configuration of one knife-edge pinhole of the system is shown. The opening angle α of the pinhole is always chosen as small as possible to maximize the stopping power of the pinhole aperture material, but such that the pre-defined CFOV is projected on the detector without being truncated by the collimator, therefore α equals $2\arcsin(r_f/r_c)$.

Once the geometry and physical properties of the system are known, the size of the projection of the CFOV through one pinhole onto the detector can be calculated. This projection is a spherical cap on the detector with a surface S_p of approximately

$$S_p \approx \pi \left[r_f \frac{(r_d - r_c)}{r_c} \right]^2 . \tag{5.1}$$

We demand that the projections of the CFOV on the detector do not overlap. This implies that approximately a fraction of $\pi/4$ of the continuous detector surface will actually be covered with non-overlapping spherical cap projections. The number of pinholes in the collimator is determined by dividing the totally available detector surface by S_p and explicitly taking the

cover fraction $\pi/4$ into account.

The system resolution is calculated as follows:

$$R_t = \sqrt{\left(\frac{r_c}{r_d - r_c}\right)^2 R_i^2 + R_{\text{geo}}^2} \tag{5.2}$$

with the geometrical resolution in the center of the system

$$R_{\text{geo}} = d_{\text{eff,R}} \frac{r_d}{r_d - r_c}. \tag{5.3}$$

Here we take penetration effects along the knife-edges of the pinhole apertures into account following [37]: the effective pinhole diameter in the resolution sense is given by

$$d_{\text{eff,R}} = d + \frac{\ln(2)}{\mu} \tan(\frac{\alpha}{2}). \tag{5.4}$$

Note that the reconstructed resolution can be significantly better than the system resolution of equation (5.2) when photon transport through the pinhole aperture edge plus detector blurring are modeled during iterative reconstruction of the image.

The sensitivity resulting from projection through one pinhole can be computed taking penetration and attenuation effects of the knife-edge pinhole-aperture material into account [38]:

$$d_{\text{eff,S}} = \sqrt{d^2 + \frac{2}{\mu} d \tan(\frac{\alpha}{2}) + \frac{2}{\mu^2} \tan^2(\frac{\alpha}{2})}. \tag{5.5}$$

Multiplied by the number of pinholes N in the collimator and by the detector capturing efficiency ε, this gives the total sensitivity of the system for a point source in the middle of the CFOV

$$S = N \cdot \varepsilon \cdot \frac{d_{\text{eff,S}}^2}{16 r_c^2}. \tag{5.6}$$

When the detector is fixed this leaves the collimator with pinholes as the part that can be modified most easily. To determine the collimator parameters that give the best performing system we employ a scheme where we start with a reference system with a given resolution and sensitivity. We look for a possible improvement of the system by varying r_c and d simultaneously while keeping the sensitivity (or resolution) on a fixed value as a constraint. Then the pairs of values for r_c and d can be determined for which the system resolution (or sensitivity) of the new system improves over the reference system. This is done numerically, or visually from graphs.

The same procedure is applied when other parameters are varied, e.g., the detector radius r_d and d while keeping the collimator radius r_c constant.

5.3 Results

5.3.1 Conventional Detector Systems (CDS)

For optimization of CDS, first a reference system with parameters approximating U-SPECT-I was determined. The reference sensitivity and resolution for the case of gold pinholes of 0.3 and 0.6 mm were calculated. All calculations were performed for ^{99m}Tc at 140 keV, where the attenuation coefficient for gold μ = 4.27 mm^{-1} [39]. The CFOV radius was chosen r_f = 6 mm, and the collimator radius r_c = 24 mm. The gamma detectors are approximated by a detector with radius r_d = 190 mm and opening angle $\omega = 25^\circ$. Like U-SPECT-I, a detector with 10 mm NaI scintillation crystals was assumed which has a capturing efficiency for perpendicular incidence, neglecting depth-of-interaction effects, $\varepsilon = 0.89$ at 140 keV and intrinsic resolution R_i = 3.2 mm. Based on these input parameters the model implies that the system has sixty complete pinhole projections, system resolution $R_t = 0.87$ mm, and system sensitivity $S = 0.25\%$ for $d = 0.6$ mm pinholes, and $R_t = 0.61$ mm, $S = 0.077\%$ for $d = 0.3$ mm pinholes. The model input parameters and resulting system properties are summarized in the first two columns of table 5.1.

With this fixed-detector set-up, optimization is possible by varying the collimator parameters. First the sensitivity is kept fixed at the reference system's value for radius $r_c = 24$ mm, i.e., S = 0.077% for d = 0.3 mm, and S = 0.25% for d = 0.6 mm (see table 5.1). By then varying r_c and d simultaneously different values for R_t are obtained. The top two panels of figure 5.2 show, as a function of r_c, the resulting system resolution R_t as well as the resulting pinhole diameter d. The optimal system resolution is found when the collimator with pinholes is placed as close as possible to the object. For $S = 0.077\%$ an improvement in resolution of 26% can be attained while for $S = 0.25\%$ an improvement of 13% is possible compared to the reference system (table 5.2). Here we chose a lower limit of r_c = 14 mm to allow an actual mouse to fit into the measuring cavity.

The bottom panels of figures 5.2 and 5.3 show the results of optimizing the system's sensitivity for fixed system resolutions: R_t = 0.61 mm (d = 0.3 mm) and R_t = 0.87 mm (d = 0.6 mm). Again, r_c and d are varied simultaneously but now to keep R_t fixed. The resulting sensitivities and pinhole diameters are shown in the bottom two panels of figure 5.2. The same trend as with the optimization for resolution is observed, i.e., the optimal sensitivity is found when the collimator with pinholes is placed as close as possible to the object. Keeping R_t fixed at 0.87 mm an increase of sensitivity of 36% is achievable while for a R_t fixed at 0.61 mm a sensitivity increase of even 108% is achievable (see table 5.2), where we chose a lowest limit r_c = 14 mm for the collimator again.

The characteristics of CDS with larger detector radii (r_d = 240 mm and 290 mm) are also

Table 5.1: Above the horizontal line the model parameters for several representative systems with conventional detectors (CDS) and high-resolution detectors (HRDS) are presented. The parameters that are not given are the same for all systems considered here: r_f = 6 mm, r_c = 24 mm, μ = 4.27 mm $^{-1}$, and ω = 25°. Below the horizontal line the resulting system properties for these configurations are given.

	CDS				HRDS			HRDS			HRDS			HRDS		
d [mm]	0.3	0.6	0.6	0.6	0.024	0.22	0.3	0.024	0.22	0.3	0.11	0.45	0.59	0.11	0.45	0.59
r_d [mm]	190	190	240	290	30	75	190	30	75	190	30	75	190	30	75	190
R_i [mm]	3.2	3.2	3.2	3.2	0.1	0.1	0.1	0.2	0.2	0.2	0.1	0.1	0.1	0.2	0.2	0.2
# pinholes	60	60	56	54	754	99	60	754	99	60	754	99	60	754	99	60
α [°]	29	29	29	29	29	29	29	29	29	29	29	29	29	29	29	29
R_g [mm]	0.39	0.74	0.71	0.70	0.33	0.39	0.39	0.33	0.39	0.39	0.76	0.39	0.72	0.33	0.72	0.72
R_t [mm]	0.61	0.87	0.80	0.76	0.52	0.40	0.39	0.76	0.40	0.39	0.86	0.39	0.72	1.10	0.73	0.72
S [%]	0.077	0.25	0.24	0.23	0.077	0.077	0.077	0.077	0.077	0.077	0.25	0.25	0.25	0.25	0.25	0.25
$d_{\mathrm{eff,R}}$ [mm]	0.34	0.64	0.64	0.64	0.066	0.26	0.34	0.066	0.26	0.34	0.15	0.49	0.63	0.15	0.49	0.63
$d_{\mathrm{eff,S}}$ [mm]	0.37	0.66	0.66	0.66	0.10	0.29	0.37	0.10	0.29	0.37	0.18	0.51	0.65	0.18	0.51	0.65

Table 5.2: Optimization results for CDS systems with parametrizations of table 5.1 for three different detector radii. In the top half the results for the collimator configuration and optimal system resolution are shown when the sensitivity is kept fixed; in the bottom half the sensitivity when the system resolution is kept fixed. The left half shows the optimal results; the right half shows the results when a realistic value for the collimator radius was taken: r_c = 24 mm.

r_d	190 mm		240 mm		290 mm		190 mm		240 mm		290 mm	
S fixed [%]	0.077	0.25	0.077	0.25	0.077	0.25	0.077	0.25	0.077	0.25	0.077	0.25
Optimal R_t [mm]	0.45	0.76	0.42	0.74	0.40	0.73	0.61	0.87	0.53	0.82	0.49	0.79
r_c [mm]	14.0	14.0	14.0	14.0	14.0	14.0	24.0	24.0	24.0	24.0	24.0	24.0
# pinholes	18	18	18	18	18	18	61	61	56	56	55	55
d [mm]	0.26	0.58	0.27	0.60	0.27	0.61	0.30	0.60	0.31	0.62	0.32	0.63
R fixed	0.61	0.87	0.61	0.87	0.61	0.87	0.61	0.87	0.61	0.87	0.61	0.87
Optimal S [%]	0.16	0.34	0.17	0.35	0.17	0.35	0.075	0.25	0.12	0.29	0.14	0.31
r_c [mm]	14.0	14.0	14.0	14.0	14.0	14.0	24.0	24.0	24.0	24.0	24.0	24.0
# pinholes	18	18	18	18	18	18	61	61	56	56	55	55
d [mm]	0.43	0.69	0.46	0.72	0.48	0.74	0.29	0.60	0.40	0.67	0.45	0.71

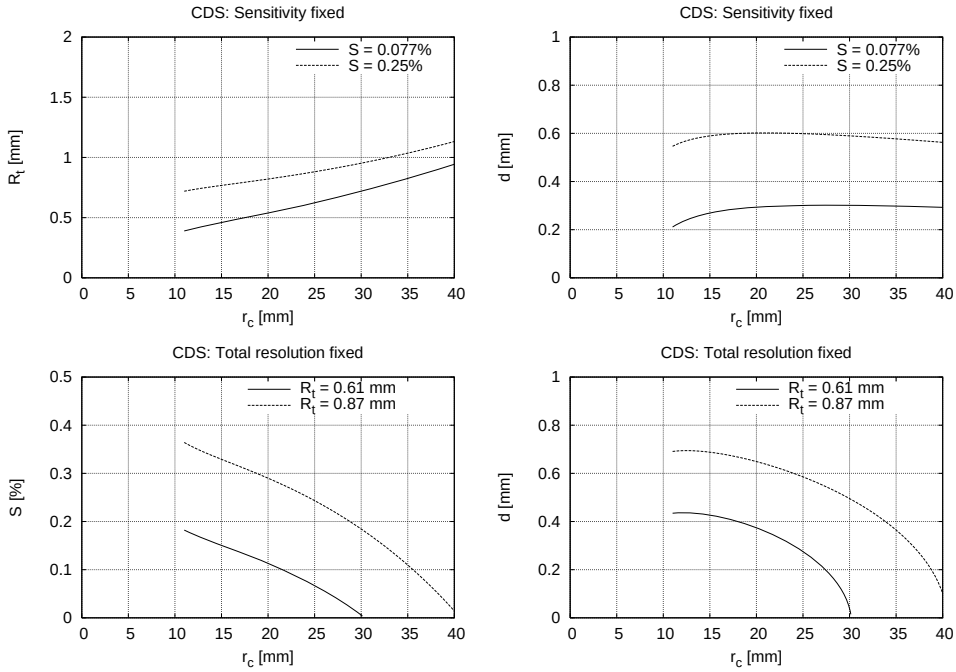

Figure 5.2: Optimization results of a conventional detector system (CDS): optimal system resolution and sensitivity are obtained when the collimator is placed as close as possible to the animal. The two top figures show the resulting system resolution R_t and corresponding pinhole diameter d are shown as function of the collimator radius r_c for fixed sensitivities S = 0.25% and 0.077%. The two bottom figures show the results for the sensitivity and pinhole diameter when the system resolution is kept fixed at R_t = 0.61 mm and 0.87 mm.

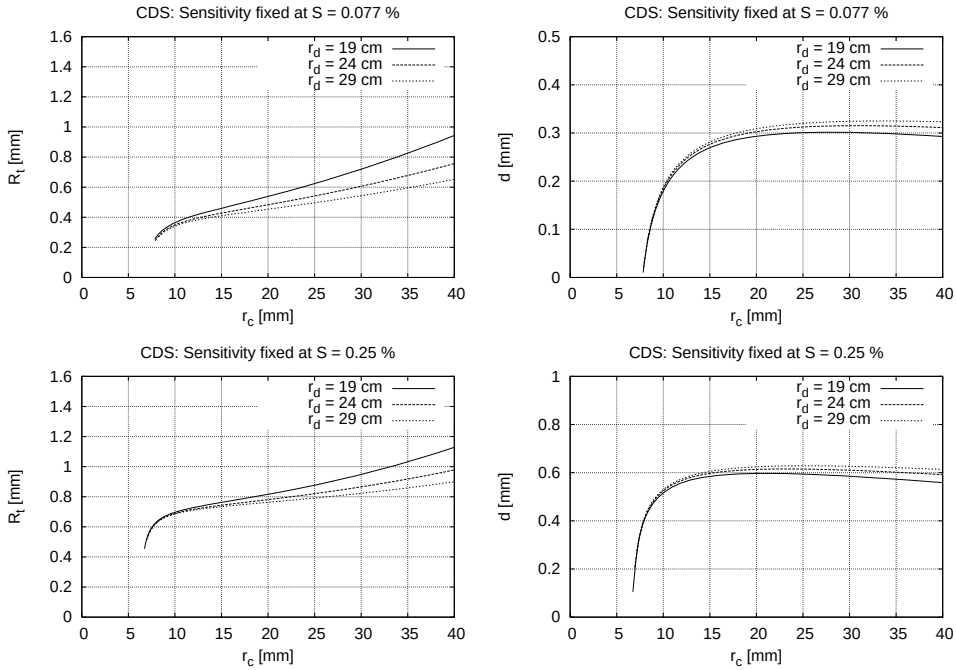

Figure 5.3: For three different detector sizes of a CDS system and two fixed values for the system sensitivity, the system resolution R_t and pinhole-diameter d as function of r_c are shown. A bigger detector size (bigger magnification) gives better results.

Table 5.3: The results (system resolution and collimator configuration) of optimization for resolution for several HRDS system configurations as given as in table 5.1. The sensitivity is kept fixed at S = 0.077% or S = 0.25%.

	HRDS					
r_d [mm]	30	75	190	30	75	190
R_i [mm]	0.1	0.1	0.1	0.2	0.2	0.2
S fixed [%]	0.077					
Optimal R_t [mm]	0.31	0.35	0.36	0.35	0.35	0.36
r_c [mm]	14.0	14.0	14.0	14.0	14.0	14.0
# pinholes	54	24	18	54	24	18
d [mm]	0.086	0.21	0.26	0.086	0.21	0.26
S fixed [%]	0.25					
Optimal R_t [mm]	0.68	0.70	0.71	0.69	0.70	0.71
r_c [mm]	14.0	14.0	14.0	14.0	14.0	14.0
# pinholes	54	24	18	54	24	18
d [mm]	0.28	0.49	0.58	0.28	0.49	0.58

shown in table 5.1. As the magnification increases, so does the system resolution. Compared to the system with r_d = 190 mm a 13% better resolution can be reached by setting r_d to 290 mm while the sensitivity decreases with only 8%.

For these three different CDS detector sizes the system parameters were optimized for resolution by keeping the sensitivity S fixed. The resulting system resolution and pinhole diameters are displayed in figure 5.3 and the left half of table 5.2 (with 14 mm taken as the minimum value for r_c). The effect of using a larger detector on the optimal resolution becomes more significant for larger collimator diameters. When keeping r_c fixed at the realistic value of 24 mm, with bigger detectors the system resolution can be improved up to 10% (for S = 0.25%) or about 20% (for S = 0.077%) compared to the reference systems with the same sensitivities (see the right half of table 5.2).

5.3.2 High-Resolution Detector Systems (HRDS)

For HRDS three different values for the detector radius r_d (30, 75, and 190 mm) and two different intrinsic resolutions R_i (0.1 and 0.2 mm) are investigated. To enable comparison with the CDS model, we choose all the other system parameters (r_f, r_c, μ, ω, ε) identical except for the pinhole diameter d. For each of the systems the pinhole diameter is chosen such that the resulting sensitivity of the system is 0.077% or 0.25%, corresponding with the CDS

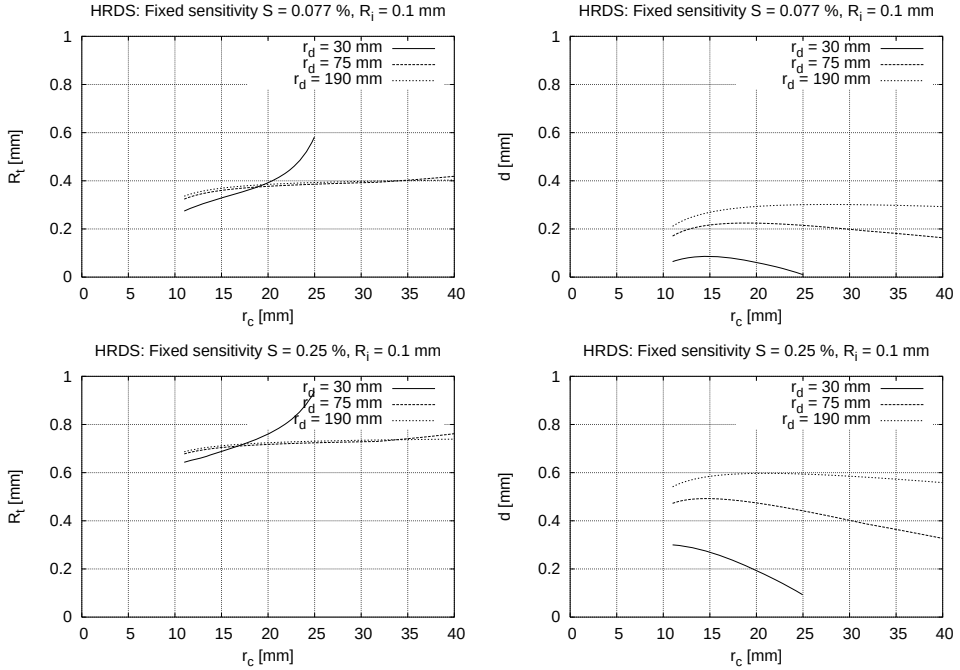

Figure 5.4: The results of optimization for system resolution of a HRDS system with three different detector radii and R_i = 0.1 mm. The two top figures show the resulting system resolution and corresponding pinhole diameter as function of r_c for fixed sensitivity S = 0.077%; the two bottom figures for S = 0.25%.

reference system's sensitivities for d = 0.6 and d = 0.3 mm pinholes respectively. For these 12 configurations the model parameters and the resulting system properties are displayed in table 5.1.

Table 5.3 and figure 5.4 show that a system resolution of an HRDS system can be improved up to 49% when compared to the unoptimized CDS system (with R_d = 190 mm) when compared at equal sensitivity, and up to 31% better resolution is reached when compared to the optimized CDS system (with R_c = 14 mm and R_d = 190 mm), a number which for the optimal value of R_c is rather independent of the detector radius. Again, it is beneficial to place the pinholes as close as possible to the mouse. This, however, could lead to a rather low number of pinholes. Such set-ups can conflict with a minimum number of pinholes that is required to cover the CFOV from a sufficient number of different angles in a pure stationary mode. In the case of too small a number of angles, better sampling can then be achieved by moving the bed, see, e.g., [20, 28].

Since high-resolution detectors are very expensive it is interesting to see that a small

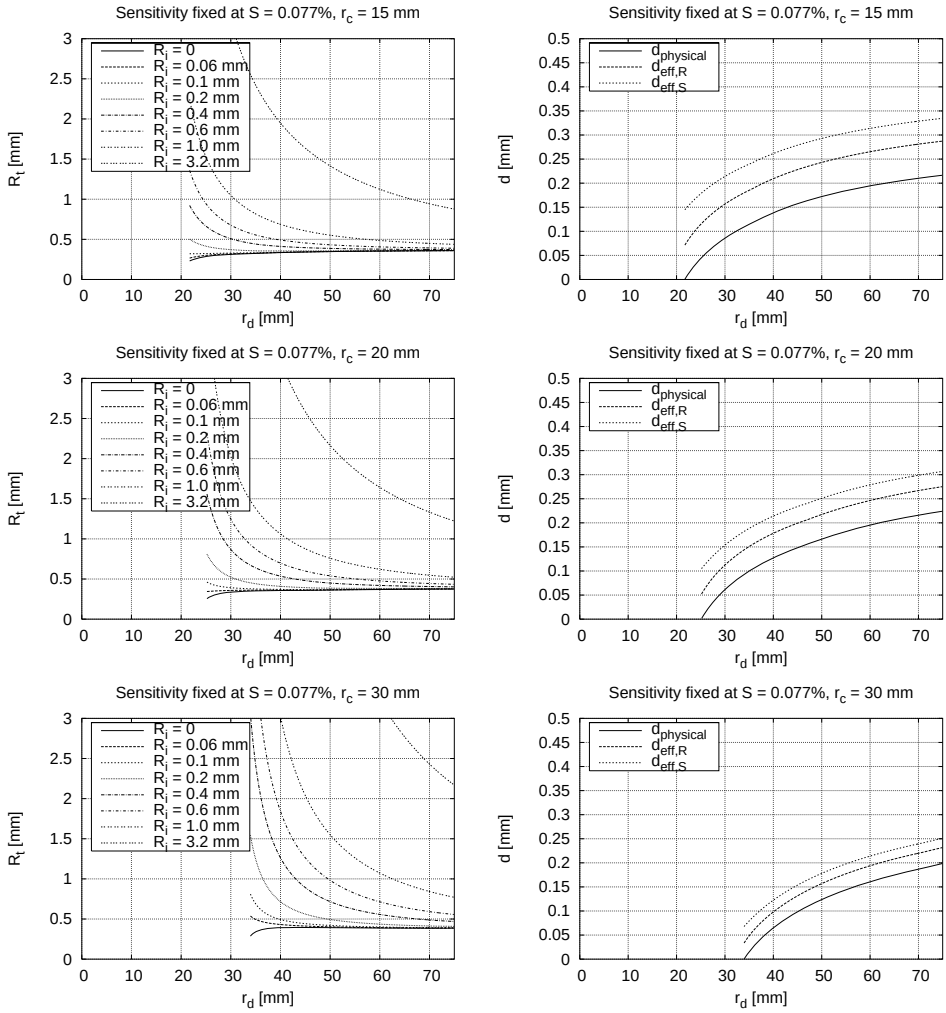

Figure 5.5: Results of optimizing an HRDS system with fixed collimator radius and fixed sensitivity S = 0.077%. The resulting system resolution R_t and pinhole diameters d are shown as a function of detector radius r_d for seven different intrinsic resolutions R_i. From top to bottom for three different values of r_c: 15, 20, and 30 mm.

detector ring can be used without a strong reduction in image quality. As the price of the detectors is dependent on the intrinsic resolution the calculations are made for different values of R_i. In the model that means that we can also study the dependence on the intrinsic resolution R_i in addition to the size of the detector. To find the optimal detector set-up we take the HRDS model, keep the sensitivity fixed and vary the detector radius and pinhole diameter simultaneously. This is done for three fixed values for the collimator radius: r_c = 15, 20, and 30 mm. The resulting system resolution and pinhole diameters are shown in figure 5.5 for fixed $S = 0.077\%$ and for R_i equaling 0.06, 0.1, 0.2, 0.4, 0.6, 1.0, and 3.2 mm.

We see that given a fixed collimator radius and a fixed sensitivity, a larger detector radius, and thus a larger magnification, almost always helps to attain a better resolution. However, there appears to be a point where this improvement is no longer significant. For example, in figure 5.5 we can see that for a system with collimator radius r_c = 15 mm for detector radii larger than r_d = 40 mm an intrinsic resolution better than 0.2 mm does not lead to a vast improvement of the system resolution.

Figure 5.5 also demonstrates that when the detector radius r_d is getting smaller and approaching (but not reaching) the collimator radius r_c, at some point the physical pinhole diameter becomes zero. In that case all photons that reach the detector do so by penetrating through the pinhole aperture material. Although the physical pinhole diameter is zero, the effective pinhole diameter (which is also shown in the figures) is not. These systems can still reach a good resolution when the value of R_i is sufficiently low such that the curve in figure 5.5 is almost flat.

The very compact system with r_d = 30 mm is studied in figure 5.6. The dependence of the obtained system resolution R_t is considered as a function of the collimator radius r_c with the intrinsic resolution R_i of the detector as a parameter. The results are shown for seven values of R_i between 0 and 1 mm and sensitivities S = 0.077% and 0.25%. Again, the optimal results are obtained when the collimator is placed as close as possible to the animal. The figure clearly illustrates that in these situations where $d_{\text{eff}} \gg d_{\text{physical}}$ the penetration effects are very significant. For whole-body scanning of animals, however, a larger radius r_c is needed. The performance of a system is still good in that case.

5.4 Discussion

An analytical model of a multi-pinhole SPECT system was constructed. The model is based on spherical symmetry and contains a collimator and detector shaped as spherical layers. It explicitly includes the effects of penetration through the pinhole aperture material according to a validated model [40].

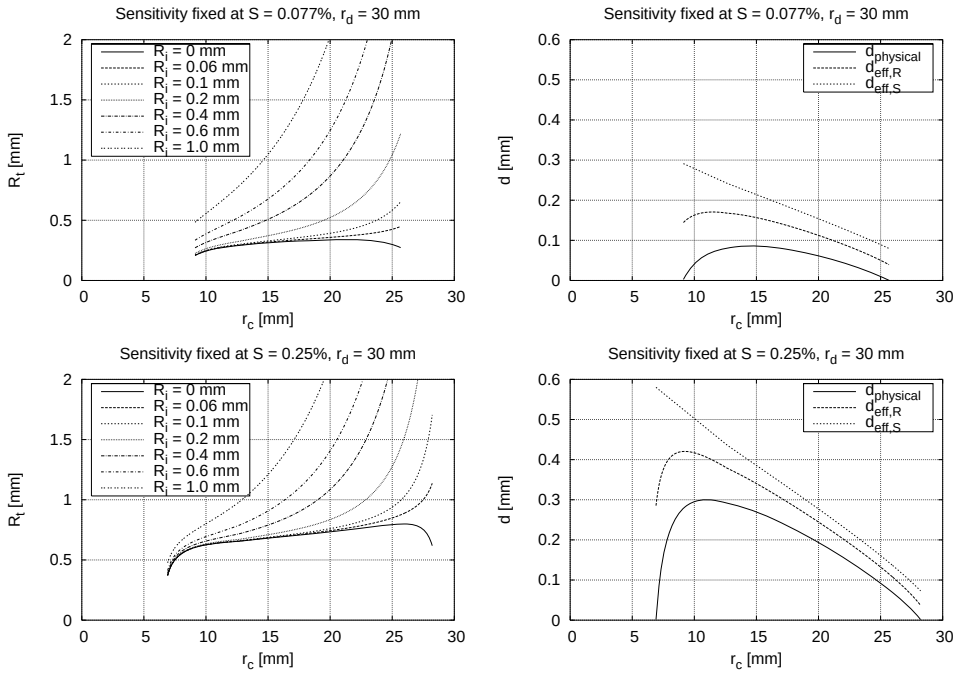

Figure 5.6: For a compact HRDS system with r_d = 30 mm and six different intrinsic resolutions R_i of the detector, the resulting pinhole diameter and system resolution are shown as function of the collimator radius r_c when the sensitivity S is kept fixed. The two top figures for S = 0.077%, the two bottom figures for S = 0.25%.

With the model, SPECT systems with conventional low-resolution detectors (CDS) and high-resolution detectors (HRDS) were studied. An attempt to optimize a CDS resembling the U-SPECT-I system has been made. With the U-SPECT-I system we are dealing with an almost unalterable clinical gamma camera. This leaves only the collimator that can be adjusted to create an optimal system. We can optimize the system by decreasing the collimator radius as is shown in figure 5.2. For a fixed sensitivity S, an improvement of resolution of as much as 34% for the U-SPECT-I system with 0.3 mm pinholes is within reach. To achieve that, however, the collimator would have to be placed as close as possible to the object, which may not always be desirable for practical reasons. Some additional space around the mouse is needed for equipment, e.g., the heating system for the bed, or tubes, but also space is required for easy movement of the bed with the mouse, especially for total-body imaging in scanning focus mode.

In addition, we have studied HRDS systems with intrinsic detector resolutions and detector sizes as given by the parameters in table 5.1. These high intrinsic resolutions are imperative to construct a system of which the system resolution is significantly better than current existing conventional-detector systems. Demanding the same sensitivity as for the U-SPECT-I system, an improvement of about 31% over an optimized CDS system may be possible, depending on the detector radius r_d. Again the highest resolution is obtained by placing the collimator as close as possible to the mouse.

For a required fixed sensitivity we studied the explicit dependence of the resulting system resolution as a function of the detector radius (figure 5.5). The fact that for HRDS systems with sufficiently low R_i the curve is almost flat leads to the conclusion that such a system can have a small detector radius. As high-resolution cameras are very expensive, this is a significant result from an economical point of view. Another interesting observation is that we can construct SPECT systems with a physical pinhole diameter of zero that will still show very respectable performance. In such systems the imaging will be achieved purely by means of photons that have penetrated through the pinhole aperture material.

In our model we do not allow the pinhole projections of the CFOV to overlap on the detector surface. Recent studies [41,42] indicate that overlap offers no significant advantages and only gives a kind of artificial increase of system sensitivity, although this will depend on the type of distribution that is imaged.

In the optimization studies conducted in this paper only two variables (r_c or r_d, and d) were varied simultaneously to find improved values for resolution by demanding a fixed value for the sensitivity, and vice versa. Implementation of these optimizations was fairly straightforward. Optimization involving more complicated constraints and where additional model parameters can be varied, e.g., in case of a budget limit on the detector system, will

require a different approach. Then not only the collimator parameters, but also the detector parameters which are intimately related to the budget (ω and r_d, corresponding to detector size; ε and R_i corresponding to detector performance) need to be varied. One could then employ an iterative scheme where the system parameters are optimized subsequently, taking all new constraints and degrees of freedom into account.

Various other optimization studies have been published, e.g. [2, 33, 35, 43, 44]. Whereas our model considers geometrical aspects as well as pinhole properties simultaneously, other studies concentrated on more particular aspects. For example, in [35] the optimal number of pinholes and their geometrical arrangement was studied by means of Monte Carlo simulations. Song et all. 2003 studied various aspects of the shape and size of the pinhole aperture.

The model proposed in this paper serves as a guide to find optimized SPECT systems, with the most relevant effects included in the model. Many practical issues that play a role when designing an actual SPECT system would be too complex to address in a simple model; it would make the model overly complex for optimization studies, likely without any additional benefit. In defining our reference model we used values for the model parameters that, given the differences in shape between the U-SPECT set-up and the spherical model, resemble the U-SPECT geometry well and closely reproduces the U-SPECT performance. Therefore the model seems to be applicable to realistic situations. Future systems may exploit some aspects of the spherical symmetry of our model which may offer a more efficient use of the detector surface. Although we studied dedicated small-animal SPECT systems in the present paper, our model may just as well be applicable to explore clinical pinhole SPECT.

5.5 Conclusion

We constructed an analytical model for the resolution and sensitivity properties of multi-pinhole SPECT. The effects of penetration through the pinhole aperture material were explicitly included. Depending on the actual freedom one has in designing the collimator and the detector, the model has many parameters that can be adjusted. The model was used to optimize the performance of current systems and to find future system configurations that lead to even better performance.

For both conventional detector systems (CDS) and high-resolution detector systems (HRDS), placing the pinhole collimator as close as possible to the object will result in the highest resolution. HRDS systems can achieve a system resolution superior to that of contemporary systems without a decrease of sensitivity. Compared to CDS systems these can be very compact.

This study indicates that small-animal SPECT devices can be improved significantly, particularly when high-resolution detectors are available.

Acknowledgments

This work was sponsored by the Medical Council of The Netherlands Organisation for Scientific Research, grant 917.36.335.

Bibliography

[1] J. Palmer and P. Wollmer. Pinhole emmission computed tomography: method and experimental evaluation. *Phys. Med. Biol.*, 35(3):339–350, 1990.

[2] M. M. Rogulski, H. B. Barber, H. H. Barrett, R. L. Shoemaker, and J. M. Woolfenden. Ultra-high-resolution Brain spect imagine: Simulation results. *IEEE Trans. Nucl. Sci.*, 40:1123–1129, 1993.

[3] R. K. Rowe, J. N. Aarsvold, H. H. Barrett, J. C. Chen, W. P. Klein, B. A. Moore, I. W. Pang, D. D. Patton, and T. A. White. A stationary hemispherical SPECT imager for three-dimensional brain imaging. *J. Nucl. Med.*, 34:474–480, 1993.

[4] R. J. Jaszczak, J. Li, H. Wang, M. R. Zalutsky, and R. E. Coleman. Pinhole collimation for ultra-high-resolution small-field-of-view SPECT. *Phys.Med.Biol.*, 39:425–37, 1994.

[5] K. Ishizu, T. Mukai, Y. Yonekura, M. Pagani, T. Fujita, N. Tamaki, H. Shibasaki, and J. Konishi. Ultra-high-resolution SPECT system using four pinhole collimators for small animal studies. *J. Nucl. Med.*, 26:2282–2289, 1995.

[6] D. A. Weber and M. Ivanovic. Ultra-high-resolution imaging of small animals: implications for preclinical and research studies. *J. Nucl. Card.*, 6:332–344, 1999.

[7] M. C. Wu, H. R. Tang, D. W. Gao, A. Ido, J. W. O'Connell, B. H. Hasegawa, and M. W. Dae. ECG gated pinhole SPECT in mice with millimeter resolution. *IEEE Trans. Nucl. Sci.*, 47:1218–1227, 2000.

[8] Z. Liu, G. A. Kastis, G. D. Stevenson, H. H. Barrett, L. R. Furenlid, M. A. Kupinski, D. D. Patton, and D. W. Wilson. Quantitative analysis of acute myocardial infarct in rat hearts with ischemia-reperfusion using a high-resolution stationary SPECT system. *J. Nucl. Med.*, 43(7):933–939, 2002.

[9] D. P. McElroy, L. R. MacDonald, F. J. Beekman, Y. Wang, B. E. Patt, J. S. Iwanczyk, B. M. W. Tsui, and E. J. Hoffman. Performance evaluation of A-SPECT: A high resolution desktop pinhole SPECT system for imaging small animals. *IEEE Trans. Nucl. Sci.*, 49:2139–2147, 2002.

[10] S. R. Meikle, P. Kench, A. G. Weisenberger, R. Wojcik, M. F. Smith, S. Majewski, S. Eberl, R. R. Fulton, A. B. Rosenfeld, and M. J. Fulham. A prototype coded aperture detector for small animal SPECT. *IEEE Trans. Nucl. Sci.*, 49(5):2167–2171, 2002.

[11] F. J. Beekman and B. Vastenhouw. Design and simulation of a high-resolution stationary SPECT system for small animals. *Phys. Med. Biol.*, 49:4579–4592, 2004.

[12] L. R. Furenlid, D. W. Wilson, Y. C. Chen, H. Kim, P. J. Pietraski, M. J. Crawford, and H. H. Barrett. FastSPECT II: A second-generation high-resolution dynamic SPECT imager. *IEEE Trans. Nucl. Sci.*, 51(3):631–635, June 2004.

[13] F. J. Beekman, F. van der Have, B. Vastenhouw, A. J. A. van der Linden, P. P. van Rijk, J. P. H. Burbach, and M. P. Smidt. U-SPECT-I: A novel system for submillimeter-resolution tomography with radiolabeled molecules in mice. *J. Nucl. Med.*, 46(7):1194 – 1200, July 2005.

[14] M. A. King, P. H. Pretorius, T. Farncombe, and F. J. Beekman. Introduction to the physics of molecular imaging with radioactive tracers in small animals. *J. Cell. Biochem.*, Suppl. 39:221–230, 2002.

[15] S. R. Meikle, F. J. Beekman, and S. E. Rose. Complementary molecular imaging technologies: High resolution SPECT, PET and MRI. *Drug Discovery Today: Technology*, 3:187–194, 2006.

[16] F. J. Beekman and F. van der Have. The pinhole: Gateway to ultra-high resolution three-dimensional radio-nuclide imaging. *Eur. J. Nucl. Med. Molec. Im.*, 33(accepted for publication), 2006.

[17] H. O. Anger. Scintillation camera. *Rev.Sci.Instr.*, pages 27–33, 1958.

[18] H. H. Barrett and W. C. J. Hunter. *Detectors for Small-Animal SPECT I*, chapter 2, pages 9–48. Springer, 2005.

[19] W. P. Klein, H. H. Barrett, I.W. Pang, D. D. Patton, M. M. Rogulski, J. D. Sain, and W. E. Smith. FASTSPECT: electrical and mechanical design of a high-resolution dynamic SPECT imager. *Conference Record of the 1995 Nuclear Science Symposium and Medical Imaging Conference*, 2:931 – 933, 1995.

[20] B. Vastenhouw and F. J. Beekman. Sub-mm total-body murine imaging with U-SPECT-I. *J. Nucl. Med.*, page (accepted), 2007.

[21] F. van der Have, B. Vastenhouw, M. C. M. Rentmeester, and F. J. Beekman. System calibration and statistical image reconstruction for sub-mm stationary pinhole SPECT. *Conference Record of the 2005 Nuclear Science Symposium and Medical Imaging Conference, Puerto Rico*, pages M11–291, 2005.

[22] G. A. de Vree, A. H. Westra, I. Moody, F. van der Have, C. M. Ligtvoet, and F. J. Beekman. Photon-counting gamma camera based on an electron-multiplying CCD. *IEEE Trans. Nucl. Sci.*, 52(3):580 – 588, June 2005.

[23] H. B. Barber. Applications of semiconductor detectors to nuclear medicine. *Nucl. Instr. and Meth. A*, 436:102–110, 1999.

[24] T. E. Peterson, D. W. Wilson, and H. H. Barrett. Application of silicon strip detectors to small-animal imaging. *Nucl. Instr. Meth. A*, 505:608–611, 2003.

[25] L. J. Meng, N. H. Clinthorne, S. Skinner, R. V. Hay, and M. Gross. Design and feasibility study of a single photon emission microscope system for small animal I-125 imaging. page (in press), 2006.

[26] Vivek V. Nagarkar, Irina Shestakova, Valeriy Gaysinskiy, Sameer V. Tipnis, Bipib Singh, William Barber, Bruce Hasegawa, and Gerald Entine. A CCD-based detector for SPECT. *IEEE Trans. Nucl. Sci.*, 53:54 – 58, 2006.

[27] Todd C. Soesbe, Matthew A. Lewis, Edmond Richter, Nikolai V. Slavine, and Peter P. Antich. Development and evaluation of an EMCCD based gamma camera for use in preclinical SPECT imaging. *IEEE Trans. Nucl. Sci.*, (submitted for publication), 2006.

[28] F. J. Beekman, B. Vastenhouw, and F. van der Have. Towards 3D nuclear microscopy using locally focusing many-pinhole SPECT. *Proceedings of the 2003 International Meeting on Fully Three-Dimensional Image Reconstruction in Radiology and Nuclear Medicine*, 1, 2004.

[29] Steven Staelens, Kathleen Vunckx, Jan De Beenhouwer, Freek Beekman, Yves D'Asseler, Johan Nuyts, , and Ignace Lemahieu. GATE simulations for optimization of pinhole imaging. *Nucl. Instr. Meth. A*, 569(2):359–363, 2006.

[30] M. F. Smith and R. J. Jaszczak. An analytic model of pinhole aperture penetration for 3D SPECT image reconstruction. *Phys.Med.Biol.*, 33:761–775, 1998.

[31] M. Gieles, H. W. A. M. de Jong, and F. J. Beekman. Monte Carlo simulations of pinhole imaging accelerated by kernel-based forced detection. *Phys. Med. Biol.*, 47:1853–1867, 2002.

[32] H. M. Deloar, H. Watabe, T. Aoi, and H. Iida. Evaluation of penetyration and scattering components in conventional pinhole SPECT: Phantom studies using monte carlo simulation. *Phys. Med. Biol.*, 48:995–1008, 2003.

[33] Tae Yong Song, Yong Choi, Yong Hyun Chung, Jin Ho Jung, Yearn Seong Choe, Kyung-Han Lee, Sang Eun Kim, and Byung-Tae Kim. Optimization of pinhole collimator for small animal SPECT using monte carlo simulation. *IEEE Trans. Nucl. Sci.*, 50:327–332, 2003.

[34] F. van der Have and F. J. Beekman. Photon penetration and scatter in micro-pinhole imaging: a Monte Carlo investigation. *Phys. Med. Biol.*, 49:1369–1386, 2004.

[35] Zixiong Cao, Girish Bal, Roberto Accorsi, and Paul D. Acton. Optimal number of pinholes in multi-pinhole SPECT for mouse brain imaging — a simulation study. *Phys. Med. Biol.*, 50:4609–4624, 2005.

[36] F. van der Have and F. J. Beekman. Penetration, scatter and sensitivity in channel micro-pinholes for SPECT: a Monte Carlo investigation. *IEEE Trans. Nucl. Sci.*, 53(5):(accepted), October 2006.

[37] R. Accorsi and S. D. Metzler. Analytic determination of the resolution-equivalent effective diameter of a pinhole collimator. *IEEE Trans. Med. Im.*, 23(6):750–763, June 2004.

[38] S. D. Metzler, J. E. Bowsher, M. F. Smith, and R. J. Jaszczak. Analytic determination of pinhole collimator sensitivity with penetration. *IEEE Trans. Med. Im.*, 20:730–741, 2001.

[39] M. J. Berger, J. H. Hubbell, S. M. Seltzer, J. S. Coursey, and D. S. Zucker. XCOM: Photon cross section database. *[Online]*, 1999.

[40] S. D. Metzler and R. Accorsi. Resolution- versus sensitivity-effective diameter in pinhole collimation: experimental verification. *Phys. Med. Biol.*, 50:5005 – 5017, 2005.

[41] K. Vunckx and J. Nuyts. Effect of overlapping projections on reconstruction image quality in multipinhole spect. *Conference Record of the 2006 Nuclear Science Symposium and Medical Imaging Conference, San Diego*, pages M11–412, 2006.

[42] P. Mok, Y. Wang, and B. M. W. Tsui. Quantification of the multiplexing effect in multi-pinhole small animal SPECT. *Conference Record of the 2006 Nuclear Science Symposium and Medical Imaging Conference, San Diego*, pages M07–1, 2006.

[43] M. Ivanovic, D. A. Weber, and S. Loncaric. Multi-pinhole collimator optimization for high resolution SPECT imaging. *IEEE Nuclear Science Symposium, 1997*, 2:1097–1101, 1997.

[44] N. Schramm, A. Wirrwar, and H. Halling. Development of a multi-pinhole detector for high-sensitivity SPECT imaging. *Conference Record of 2001 IEEE Nuclear Science Symposium and Medical Imaging Conference, San Diego, USA*, 3:1585–1586, 2001.

Chapter 6

System calibration and statistical image reconstruction for ultra-high-resolution stationary pinhole SPECT systems

F van der Have, B Vastenhouw, M C M Rentmeester, and F J Beekman
Submitted.

Abstract

For multi-pinhole SPECT, iterative reconstruction algorithms are preferred over analytical methods, because of the often complex multi-pinhole geometries and the ability of iterative algorithms to compensate for effects like spatially variant sensitivity and resolution. Ideally such compensation methods are based on accurate knowledge of the position-dependent point spread functions (PSFs) specifying the response of the detectors to a point source at every position in the instrument.

This paper describes a method for model-based generation of complete PSF lookup tables from a limited number of point source measurements for stationary SPECT systems and its application to a sub-mm resolution stationary small-animal SPECT system containing 75

pinholes (U-SPECT-I). The method is based on the generalization over the entire object to be reconstructed, of a small number of properties of point source responses which are obtained at a limited number of measurement positions. The full shape of measured point source responses can almost be preserved in newly created PSF tables.

We show that these PSFs can be used to obtain high-resolution SPECT reconstructions: the reconstructed resolutions judged by rod visibility in a micro Derenzo phantom are 0.45 mm with 0.6 mm pinholes and below 0.35 mm with 0.3 mm pinholes. In addition we show that different approximations such as truncating the PSF kernel, with significant reduction of reconstruction time, can still lead to acceptable reconstructions.

6.1 Introduction

Single Photon Emission Computed Tomography (SPECT) permits *in vivo* volumetric imaging of 3D distributions of radio-labeled molecules. Pinhole collimated SPECT is particularly suitable for studying laboratory animals such as mice and rats, because for small objects it can achieve both a high spatial system resolution and a high sensitivity when compared to parallel hole collimated SPECT. Several SPECT systems using pinhole collimation have been developed [1–8] (for reviews see [9–12]). Stationary systems (that do not need to rotate their detectors) with tens up to hundreds of pinholes have been designed [13–17]. A high number of pinholes results in a high sensitivity which can be traded for a higher system resolution by decreasing the pinhole diameter. The stationary designs provide excellent stability and unique capabilities to perform fast dynamic studies, *e.g.* [13, 18, 19].

Today, iterative reconstruction algorithms are prominent in SPECT. Iterative algorithms have the advantage that they can benefit from accurate models of the photon transport in the SPECT system and they can handle a large variety of detector-collimator geometries. In addition, they can handle noise better than direct methods of reconstruction. Several papers have shown that the more accurate photon transport is modeled during iterative reconstruction the more accurate the reconstructed images will be, not only in terms of resolution and quantitative accuracy but also in terms of signal-to-noise ratio and lesion detectability, *e.g.* [20–24]. An important advantage of iterative reconstruction is that no explicit mathematical expression for the inverse transformation is required. Iterative algorithms only need a way to predict the detector response to a given radio nuclide distribution in the object. To this end, the object space is most times divided into volume elements (voxels) and the total detector response is assumed to be the sum of the responses to small radioactive sources in all of the voxels. A specific detector response to a “point” source is known as the point spread function (PSF). The individual PSFs for all voxels collectively contain the entire information to set up the

"system matrix" or "transition matrix" M of the SPECT system. Each matrix element M_{ji} represents the likelihood that a photon emitted in voxel i is detected in detector pixel j. Then, the activity distribution $\overrightarrow{a}$ is estimated from $\overrightarrow{p} = M \cdot \overrightarrow{a} + \overrightarrow{n}$ where $\overrightarrow{p}$ is the measured projection and $\overrightarrow{n}$ represents the noise in each pixel.

The PSFs for SPECT are sometimes calculated analytically, given "known" properties of the system. Pinhole collimators make the detector response very sensitive to some parameters, *e.g.* the exact position, orientation, size, and shape of each pinhole aperture in the system. Methods for the calibration of rotating pinhole SPECT systems (based on calibration systems for cone-beam SPECT with similar geometry) have been proposed, *e.g.* [25–31], that can determine the acquisition geometry (*e.g.* the position of the pinhole with respect to the axis of rotation and the position, tilt and twist of the detector) using one up to three point sources. These systems still use an analytical model to estimate the pixel values in a PSF. In stationary pinhole systems, it is feasible to determine the PSFs themselves experimentally with a large number of point source measurements. This has the advantage that the actual positions, orientations and sizes of the pinholes and detector pixel sensitivities are accurately incorporated in the PSF tables. Difficulties in manufacturing precise pinhole positions and shapes with exactly the specified diameter (which is only a few tenths of a mm for high-resolution SPECT in mice) could make analytically predicted PSFs deviate from reality. The approach of measuring the complete matrix with a point source was developed at the University of Arizona and was used to calibrate different SPECT systems [14, 15, 32, 33].

Recently, resolutions of small animal SPECT systems have improved from typically a few mm to sub-half-mm resolution [12, 16, 17, 34, 35], which makes it hard to measure the PSF for each voxel: up to millions of tiny voxels are needed to represent the high-resolution images. Then, it is impractical to put a point source that is approximately the size of one voxel at every voxel position. The maximum achievable concentration and the number of counts that have to be acquired from every point position, make it a prohibitively long measurement. In addition, the point source may need to be replaced many times predictably at a precisely known position. Apart from a high number of voxels, a high-resolution scanner may also need a relatively high number of pixels. Depending on the available acquisition modes, this combination could mean that the intermediate storage of all raw data requires enormous amounts of disk space.

Here we propose and validate an efficient and accurate method to obtain the position-sensitive PSF tables for a high-resolution many-pinhole system [16, 17]. We explain how the full system matrix can be determined from measurements at a limited number of positions. In addition, we will present examples to give an impression of the accuracy of estimated PSFs as well as reconstructed images. The trade-off between truncation of the PSF kernel

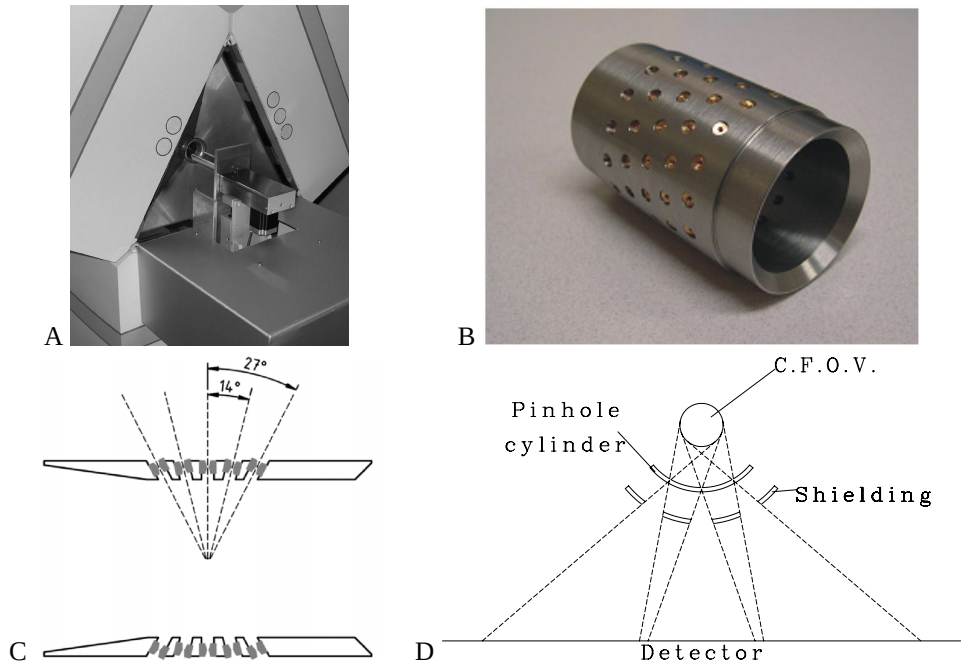

Figure 6.1: A) The U-SPECT-I system. Triangular shaped lead shielding is placed in between three camera heads. A tungsten cylinder containing pinholes is placed in the center of the three detectors. An XYZ-stage with attached bed is placed in front of the lower detector. B) Cylinder with 75 gold pinhole apertures. C) Cross-section of the cylinder with focusing pinholes. D) Cross-section of the shielding tube that prevents projections to overlap.

and the reconstruction speed was also investigated. Reconstructed images are presented for a capillary resolution phantom with different numbers of acquired counts.

6.2 Methods

The method described in this paper is developed for the stationary pinhole SPECT systems U-SPECT-I and U-SPECT-II [16, 34, 36]. These systems have 75 focusing pinholes in a cylindrical configuration with 5 rings of 15 pinholes each (see figure 6.1). The collimator cylinder is placed in the center of three gamma camera heads. Each of the camera heads is divided into a large set of mini gamma cameras, each dedicated to the projection through one pinhole. We ensure the projection areas are non-overlapping by means of a shielding

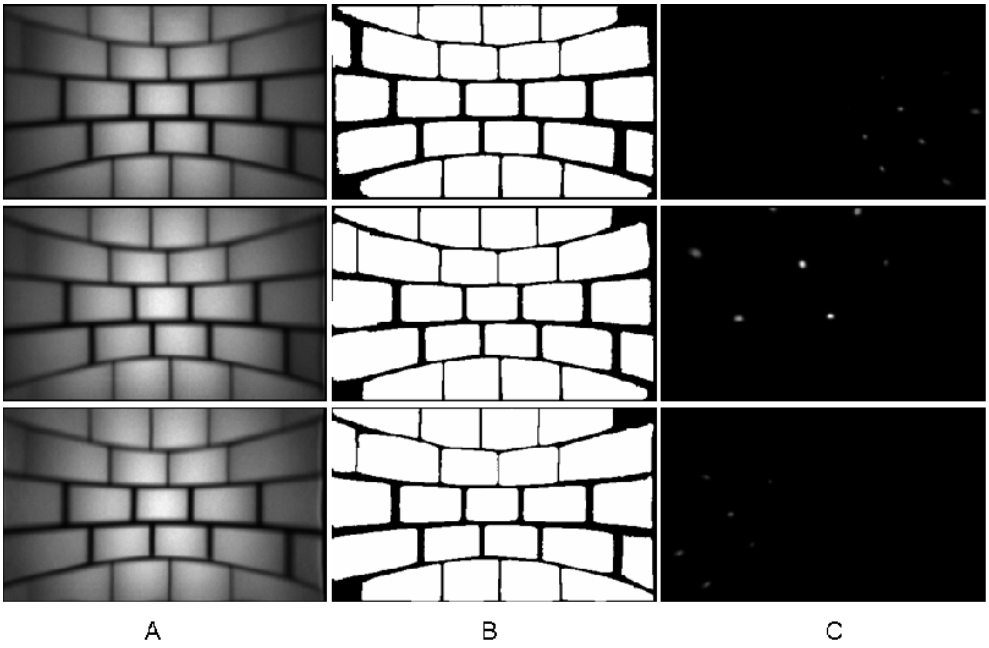

Figure 6.2: A) Measurement with extended source. B) Segmentation of the three detectors into mini gamma cameras. C) Projection of a single point source on the mini cameras.

tube [16, 37, 38]. Figure 6.2 shows how this results in dividing the three large detectors in many small cameras. It also shows an image obtained by placing a bottle with Tc-99m pertechnetate in the scanner as well as an image from a point source.

The method described here for obtaining the PSF tables is based on calculating a number of defining properties at the detector segments (namely the position on the detector, the flux, and the spatial extent) for each measured point source response. The available data are then used to fit a parametric model of these properties and the fit results are used to predict the PSFs for other voxels.

Full PSF tables (representing the "system matrix") are obtained out of a set of point source responses in four steps:

1. Noise suppression and identification of areas that contain the local maximum of a point source response.

2. Characterizing the PSFs using Gaussian modeling.

3. Generalization of the PSF's model over the object space using an analytical pinhole model.

4. Calculation of the supplementary PSFs for storage in tables.

These steps are explained in more detail in the subsections below.

6.2.1 Noise suppression and identification of areas that contain the local maximum of a of a point source response

High-frequency noise in the point source projections is suppressed by Maximum Likelihood Expectation Maximization (ML-EM) fitting with Gaussian basis functions [39]. In contrast to low-pass filtering, this procedure does not degrade the resolution of the measurements, since the width (FWHM) of the basis functions is chosen slightly smaller than the detectors' intrinsic resolution. The result is demonstrated in figure 6.3.

Each detector segment should contain either one or no projected point source. A threshold level is chosen that is based on what the highest pixel count would be in the PSF if the point source is located at the measurement position that is the farthest away from the pinhole and at the maximum angle from the pinhole's axis (the "worst case" situation). Only those detector segments where at least one pixel is above this local threshold are assumed to contain a PSF.

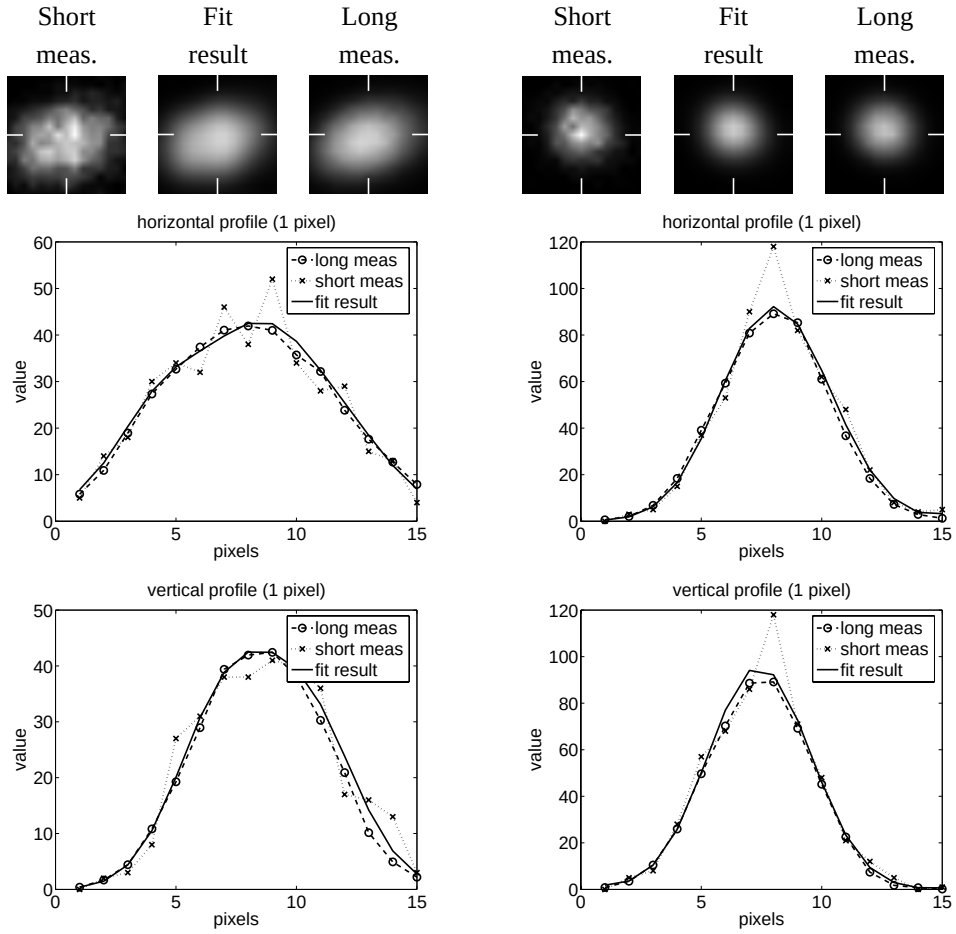

Figure 6.3: Effect of noise suppression using ML-EM fitting for two point source projections. The image after fitting is close to a reference image that has a 40 times longer acquisition period. Horizontal and vertical profiles show the values of a single row and column of pixels through the maximum, indicated by white markers.

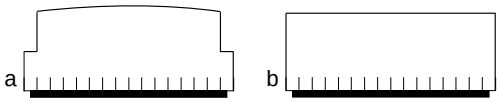

Figure 6.4: Effect of the division by a homogeneous source image. The part of the detector that is not blocked by the shielding, is represented by the black rectangle. The short vertical lines indicate the pixel boundaries. The outermost pixels are covered by the shielding for part of their surface, in this example half of it. a) profile of an extended object before division b) profile of the same object after division, the pixels on the boundaries now have the intensities they would have had if there were no shielding that partially covered them.

6.2.2 Characterizing the PSFs using Gaussian modeling

As the next step, each point source measurement is divided pixel-wise by a high-count projection measurement of a cylindrical reservoir ("bottle") larger than the central field-of-view that is homogeneously filled with Tc-99m. These projections contain information about (i) high-frequency non-uniformities in detector sensitivity and (ii) partial shielding of pixels at segment edges by the pinhole insert or the baffles that prevent overlapping of projections. Division by the extended homogeneous source projection converts the relative intensities between neighboring pixels to what they would have been if there were no shielding, see figure 6.4. This is a prerequisite for the modeling and generalization of the PSF properties over the object space. At a later stage of the process, when the PSFs at missing locations are created, the pixel values will be multiplied again by the projection pixel values obtained with the extended homogeneous source in order to restore the original scaling and recover appropriate PSF values.

After noise suppression by ML-EM fitting, described in the previous section, and after division by the high-count uniform source projection, for each segment the position of the maximum on the detector (ξ,η), the amplitude A, and the width σ are estimated for each point source measurement using Powell fitting.

The detector position of the maximum (ξ,η) is determined to sub-pixel level. The flux (total number of counts) Φ is estimated by $\Phi = 2\pi \cdot A \cdot \sigma^2$. This is an approximation, but it has the advantage that it also works when part of the PSF is outside the detector segment and therefore missing from the measurement.

The property values can only be determined reliably if a large enough fraction of the PSF is located within the detector segment. In order to guarantee this, the properties of a PSF are only determined and used for generalizing the PSF if the pixel with the highest value (after ML-EM fitting) is not on or outside a segment edge, but surrounded by pixels that are inside the segment on all sides.

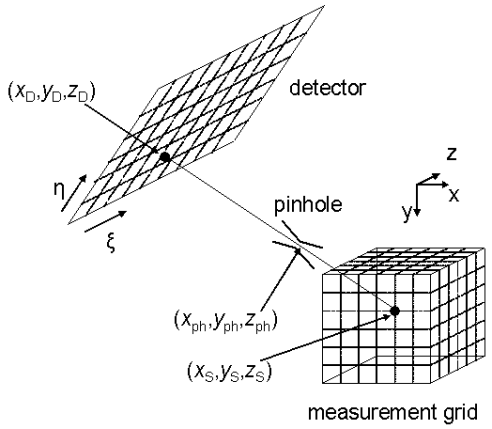

Figure 6.5: The geometry of the model for the ξ and η position on the detector. A certain source location $(x_{\mathrm{S}}, y_{\mathrm{S}}, z_{\mathrm{S}})$ is projected through the pinhole center onto a detector plane, the location of detection is at $x_{\mathrm{D}}, y_{\mathrm{D}}, z_{\mathrm{D}}$.

To obtain the PSF properties, during fitting, the number of pixels needs to be larger for wide PSFs than for narrow ones. Therefore, the fit is done twice. In the first instance all pixels that are both within the segment and within a fixed 15×15 square of pixels (13×13 mm) around the maximum are used. The result of the first fit is used to obtain an approximate value for σ which is subsequently used to determine which pixels are taken into account for the second fit: a square area of $2\sigma \times 2\sigma$, rounded off to an odd-valued integer, and centered around the maximum.

For each detector segment, four 3D arrays are created where the values of the PSF properties are stored as a function of the x, y, z coordinates of the measurement grid in the SPECT system. These arrays are from here on referred to as "property volumes".

6.2.3 Generalization of the PSF's model over the object space using an analytical pinhole model

If one wants to have PSFs available for all points that can be observed by one or more pinholes, without using more more than a few hundred measurement points, which is less than 1 in 6000 voxels for 0.125 mm voxel size, the addition of a limited amount of geometrical information (see also section 6.4, discussion) is required.

Position of the PSF maximum on the detector

The geometry of the detector position model is illustrated in figure 6.5. The point source activity is projected through the pinhole onto a detector segment, of which the orientation is not precisely known. The effective position of detection is determined by the fit procedure which has three variables (the point source's position $x_{\mathrm{S}}, y_{\mathrm{S}}, z_{\mathrm{S}}$) and nine parameters: the pinhole's position ($x_{\mathrm{PH}}, y_{\mathrm{PH}}, z_{\mathrm{PH}}$), the position ($x_{\mathrm{T}}, y_{\mathrm{T}}, z_{\mathrm{T}}$) of the origin of the detector's coordinate system expressed in the coordinate system of the measurement grid, and three rotation or Euler angles (ϕ, θ, ψ) for the detector orientation.

In order to build a mathematical model suitable for fitting, the available measured quantities need to be linked to the model's parameters and variables. The position of the point of detection ($x_{\mathrm{D}}, y_{\mathrm{D}}, z_{\mathrm{D}}$) in the measurement grid's coordinate system can be related to the pinhole position ($x_{\mathrm{PH}}, y_{\mathrm{PH}}, z_{\mathrm{PH}}$) and the source position ($x_{\mathrm{S}}, y_{\mathrm{S}}, z_{\mathrm{S}}$) by assuming that the detection point, the center of the pinhole and the source are situated on the same line:

$$\frac{x_{\mathrm{S}} - x_{\mathrm{PH}}}{x_{\mathrm{PH}} - x_{\mathrm{D}}} = \frac{y_{\mathrm{S}} - y_{\mathrm{PH}}}{y_{\mathrm{PH}} - y_{\mathrm{D}}} = \frac{z_{\mathrm{S}} - z_{\mathrm{PH}}}{z_{\mathrm{PH}} - z_{\mathrm{D}}} \tag{6.1}$$

The coordinates ($x_{\mathrm{D}}, y_{\mathrm{D}}, z_{\mathrm{D}}$) in the measurement grid's coordinate system of the point of detection are also related to the coordinates of this point in the detector's coordinate system (ξ,η) via translation and rotation:

$$R \cdot \begin{pmatrix} \xi \\ \eta \\ 0 \end{pmatrix} + \begin{pmatrix} x_{\mathrm{T}} \\ y_{\mathrm{T}} \\ z_{\mathrm{T}} \end{pmatrix} = \begin{pmatrix} x_{\mathrm{D}} \\ y_{\mathrm{D}} \\ z_{\mathrm{D}} \end{pmatrix} \tag{6.2}$$

where R is a standard rotation matrix expressed in terms of the Euler angles ϕ, θ, and ψ. Note that equating the third coordinate of the detection point in the detector's coordinate system to zero effectively means that all detections are in a plane; *i.e.* the model approximates the detection volume in the scintillation crystal, which has a finite thickness and is expected to be slightly curved due to depth-of-interaction effects, by a single plane.

By combining equations 6.1 and 6.2 and eliminating x_{D}, y_{D}, and z_{D} it is possible to express the available data (ξ and η) in terms of the model's variables and parameters, which is the desired form of a mathematical model in order to be suitable for parameter estimation by fitting. Fitting was performed using the Levenberg-Marquardt algorithm. The initial guess can be obtained by assuming that the pinhole location is on the surface of a cylinder, as seen from the center in the direction of the measurement position where the measured intensity is highest. The detector can be assumed to be behind the pinhole, perpendicular to the pinhole axis at the average pinhole-to-detector distance.

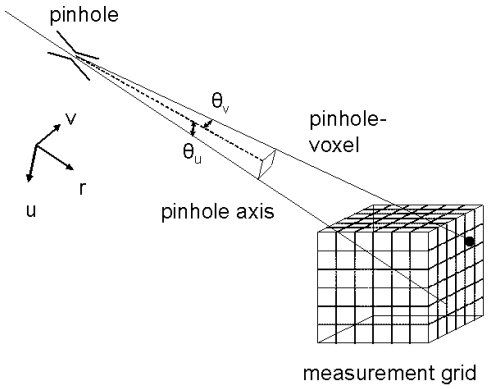

Figure 6.6: The geometry for modeling the flux.

The flux model

Like the position of the center of the PSF, the flux is also generalized using a parametric model and the same nonlinear fit routine. The geometry explaining the flux model is illustrated in figure 6.6. A coordinate system is defined with one axis (denoted "r") along the pinhole axis. The axis must go through the pinhole position itself and is assumed to go through the center of gravity of the cloud of measurement points as well. The other two axes (denoted "u" and "v") are orthogonal to the pinhole axis and to each other. The flux Φ in a certain voxel is modeled:

$$\Phi = \frac{1}{r^2}\left(A + B \cdot \theta_u + C \cdot \theta_v + D \cdot \theta_u^2 + E \cdot \theta_v^2 + F \cdot \theta_u \cdot \theta_v\right) \tag{6.3}$$

where r is the component along the pinhole axis of the distance between the voxel and the pinhole position, obtained from the position fit carried out previously, and θ_u and θ_v are the distances from the voxel to the pinhole in the u and v directions, expressed as angles.

Perpendicular to the pinhole axis, the flux is modeled by the general paraboloid of equation 6.3. If θ is the angle between the pinhole axis and the line connecting the voxel and the pinhole center, then one might expect a $\cos\theta$ dependency. However, the projection data have been divided by the projection of an extended homogeneous source before the flux was measured so the flux data are not exactly described by the $\cos\theta$ fall-off away from the pinhole axis. The fall-off is in fact still very smooth, however, and can be approximated by a paraboloid.

Using fitted parameter values $A - F$ the flux value can be calculated for each voxel in the object space.

Radial sigma

The width (radial sigma, σ_{r}) of the PSF is determined by means of fitting $D_{\mathrm{eff,R}}$, R and l in:

$$\sigma_{\mathrm{r}} = \sqrt{\left(D_{\mathrm{eff,R}} \cdot \frac{l+z}{z}\right)^2 + R^2} \tag{6.4}$$

where $D_{\mathrm{eff,R}}$ describes the effective pinhole diameter with respect to resolution, l is the distance from the pinhole to the detector, projected along the pinhole axis, and z is the distance from the point source to the pinhole, projected along the pinhole axis. The first term under the square root describes the effective pinhole diameter, projected magnified onto the detector as seen from the source. The second term R describes the camera's intrinsic resolution. Again, the pinhole position is taken form the position fit and the axis is assumed to go through the center of gravity of the cloud of measurement points.

6.2.4 Calculation of the supplementary PSFs for storage in tables

Since a low-noise (by means of the ML-EM fit) version of measured PSFs is available, we choose to use those measured PSFs to get the correct overall shape. To estimate a "missing" PSF (for a voxel location not in the measurement grid), the measured PSF whose corresponding point source location is nearest to the missing voxel location is used. That PSF is displaced on the detector to the location specified by the ξ and η values in the property volumes at the missing voxel location. The PSF is then stretched or contracted using the ratio of σ_{r} at the missing point source position to σ_{r} of the measured PSF in all directions. Finally all pixel intensities are scaled such that their sum equals the flux specified by the flux volume at the missing point source location. After the PSF has been created in this way, the pixel intensities should be multiplied by the extended homogeneous source measurement to undo the effect of the division by this measurement at the stage where the properties were determined. According to this procedure a PSF is calculated for all missing point source positions. These are stored on disk to be used in the image reconstruction algorithm.

6.2.5 Validation

We have validated the proposed generalization of PSFs by measuring some additional PSFs to the ones used to generate the PSF tables. These are compared to the corresponding PSFs in the PSF tables. The system is calibrated using 679 measurement positions. The spacing is 3 mm in the x and y (trans-axial) directions and a 1.5 mm in the z (axial) direction.

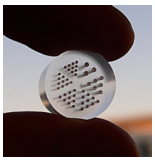

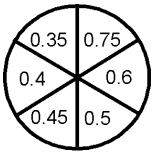

Figure 6.7: Photograph and drawing of the capillary hot rod phantom used in the experiments. The minimum distance between capillaries is equal to the diameter. Capillary sizes of this phantom range from 0.35 to 0.75 mm. In color print in the appendix.

Another validation approach is to verify that the calibration method as a whole produces high resolution reconstructed images, which will also be described in the next section, using a capillary mini Derenzo phantom as shown in figure 6.7 as the object.

6.3 Results

6.3.1 Validation in the projection domain

Figure 6.8 presents some examples of PSFs from the PSF tables generated by the procedure, alongside experimentally measured PSFs at the corresponding voxel location. Horizontal and vertical profiles through the center are shown that are summed over 3 pixels. The first three examples show different locations in the central area of the object space, the last is closer to one side of the cylinder and projects to a segment nearer to the edge of the detector. This combination makes the last PSF brighter, wider (larger σ_r) and less circularly symmetric. The first three examples show that in the central field-of-view area, the volume seen by all pinholes, there is a good agreement between the measured PSFs and the PSFs from the PSF tables, so the position, flux and width are all correctly predicted by the model. The fourth example shows a small position mismatch in the vertical direction, on the order of 0.5 mm on the detector. This remains well below the detector's intrinsic resolution and the equivalent position error in the object space would be around 0.06 mm if the location were in the central area, with a demagnification factor of 8. Most probably, it is even less since there is more demagnification in this case because this voxel's location was closer to the pinhole than the center. This example also shows an underestimation of the flux. As will be shown further on, this still leads to good reconstructions.

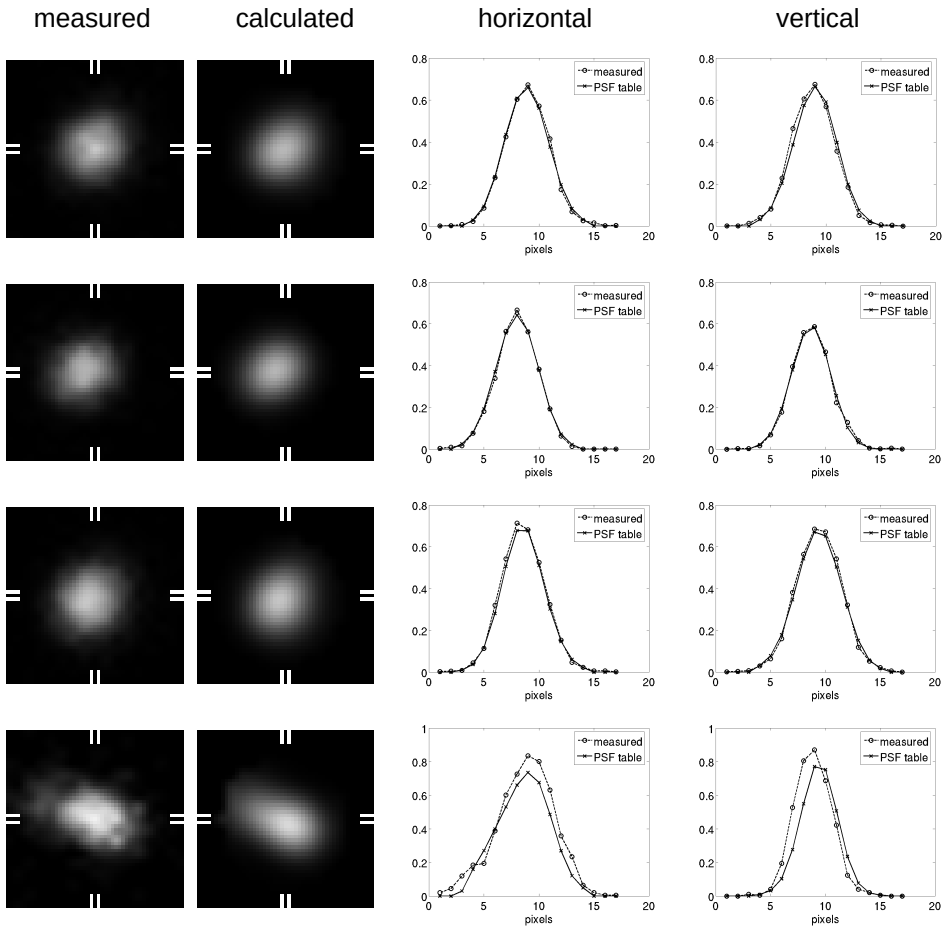

Figure 6.8: Four examples of a measured PSF, obtained at a location in between the grid used to create the PSF tables, with the corresponding PSFs from the PSF tables. The first three examples are from the central area, where the PSFs from the PSF tables predict the position and shape very well. The last example was obtained at a location more towards one side of the cylinder, making the PSF wider. It is also more elongated because it was close to the edge of a camera head, at non-perpendicular incidence.

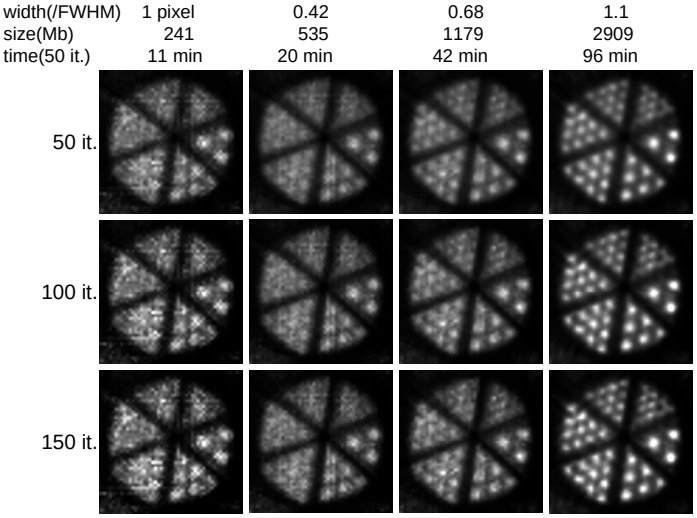

Figure 6.9: Reconstruction for different PSF tail sizes obtained with 0.3 mm pinholes. Voxel size 0.1875 mm. Slice thickness 0.375 mm. Numbers at the top represent the full width of the truncated PSF expressed in units of its FWHM, the resulting matrix size on disk in megabytes, and an example reconstruction time for 50 iterations. Vertically the number of iterations is varied: 50,100,150. Phantom capillary sizes are 0.75, 0.6, 0.5, 0.45, 0.4, and 0.35 mm.

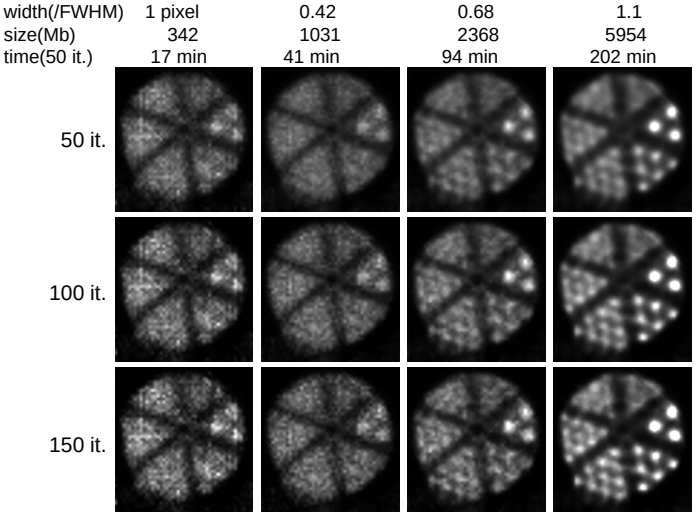

Figure 6.10: Like figure 6.9, but for 0.6 mm pinholes. Voxel size is 0.1875 mm.

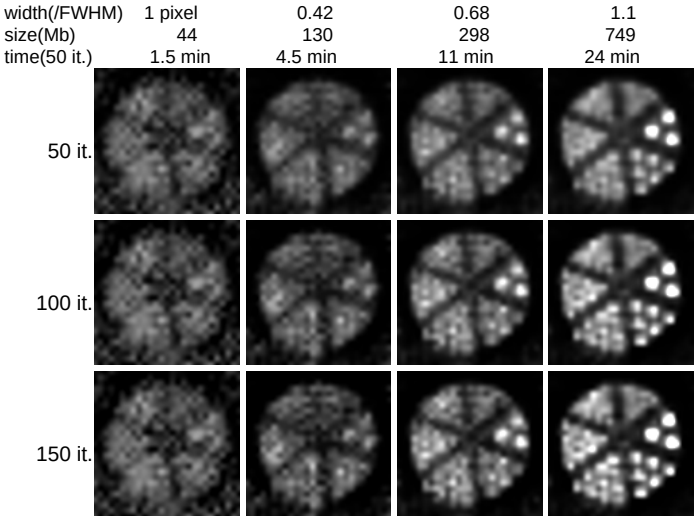

Figure 6.11: Like figure 6.10, but for 0.375 mm voxel size. Slice thickness is also 0.375 mm.

6.3.2 Reconstruction quality versus size of PSF tails

There is an important trade-off in reconstruction methods, including the iterative statistical method we use, between reconstruction accuracy and matrix size. To investigate one aspect of this trade-off, the 'tail size' that was used when PSFs were created, was varied. The diameter of the detector area for which the PSF was created, was proportional to the generalized σ_r of the PSF. The PSF generation is implemented in such a way that there is always at least one pixel in each PSF. For example, in the limiting case where the PSF diameter is $0\times$ the FWHM, all PSFs are created as the single pixel that is closest to the specified ξ, η location, containing the total specified flux. Figures 6.9–6.11 give reconstructed results for 50,100, and 150 iterations, while the tail size incorporated in the PSF is $0\times$ FWHM, $0.43\times$ FWHM, $0.68\times$ FWHM, and $1.1\times$ FWHM. Figure 6.9 is for the 0.3 mm pinholes and 0.1875 mm voxel size, figure 6.10 is for 0.6 mm pinholes and 0.1875 mm voxel size, and figure 6.11 is for 0.6 mm pinholes and 0.375 mm voxel size. The results are all compared with a slice thickness of 0.375 mm. The resulting matrix sizes on disk are given for reference as well as example reconstruction times on a 2.66 GHz Xeon system. This system had 8 Gb of memory, such that in all cases the matrix needed to be read from disk only once. The matrices used were available for a much larger voxel extent than the capillary phantom shown, which means that they would also be suitable for total-body mouse imaging for example. These reconstruction times were all obtained with the same fairly straightforward implementation of the Maximum Likelihood Expectation Maximization (ML-EM) algorithm which was not

optimized for speed. The results show that the largest PSF width of $1.1\times$ FWHM resulted in the reconstruction that allows the best visual distinction of rods. Wider PSFs were also tested, but did not lead to better results.

Voxel size has a big impact on matrix size and thus reconstruction time, because of the cubic power relation between voxel size and matrix size. The effect of doubling the voxel size (leading to an eight-fold reduction in matrix size) on image quality for the case of 0.6 mm pinholes can be seen by comparing figures 6.10 and 6.11. While the smaller voxel size results look better, the difference is not so dramatic that the coarser voxels are useless; in some applications the images with the coarser voxels may be considered good enough — estimating the total amount of activity in a fairly large region-of-interest over multiple points in time for example — where the gain in speed could make it worthwhile to use coarse voxels.

With 0.3 mm pinholes smaller rods can be distinguished than with the 0.6 mm pinholes, which may not be surprising. What may not be obvious *a priori* is that the 0.6 mm pinholes actually require at least the same PSF size in units of FWHM as the 0.3 mm pinholes in order to reach the highest achievable resolution, while each FWHM is already larger than the corresponding PSF from a 0.3 mm pinhole because of the larger diameter. This makes the 0.3 mm pinholes matrix smaller than the 0.6 mm pinholes matrix, when comparing at equal voxel and pixel size, by a factor of approximately 2 in the given examples.

6.3.3 Reconstruction with different acquisition times for 2 pinhole diameters

Figure 6.12 shows the hot rod resolution phantom images compared for different acquisition times. The activity concentration was 300 MBq/ml Tc-99m (25 MBq in total in the capillaries). The acquisition times could of course be scaled if one wants to have an impression of the achievable resolution at other concentrations. The experiment was done with both the 0.3 and the 0.6 mm pinholes and after reconstruction, the results are displayed for a slice thickness of 0.375 mm and 3.75 mm for each pinhole diameter. Visually the 0.3 mm pinholes yield a superior resolution for acquisition times down to 1 minute (or even shorter if the larger slice thickness is viewed). Only for the extremely short acquisition times (below 1 minute) do the 0.6 mm pinholes produce superior results, because the 0.3 mm pinholes collect too few counts. For 10 seconds acquisition time, it is still possible to obtain 0.75 mm reconstructed resolution for the 0.6 mm pinholes. The best achievable resolution, on the other hand, is seen to be 0.45 mm for the 0.6 mm pinholes and below 0.35 mm for the 0.3 mm pinholes.

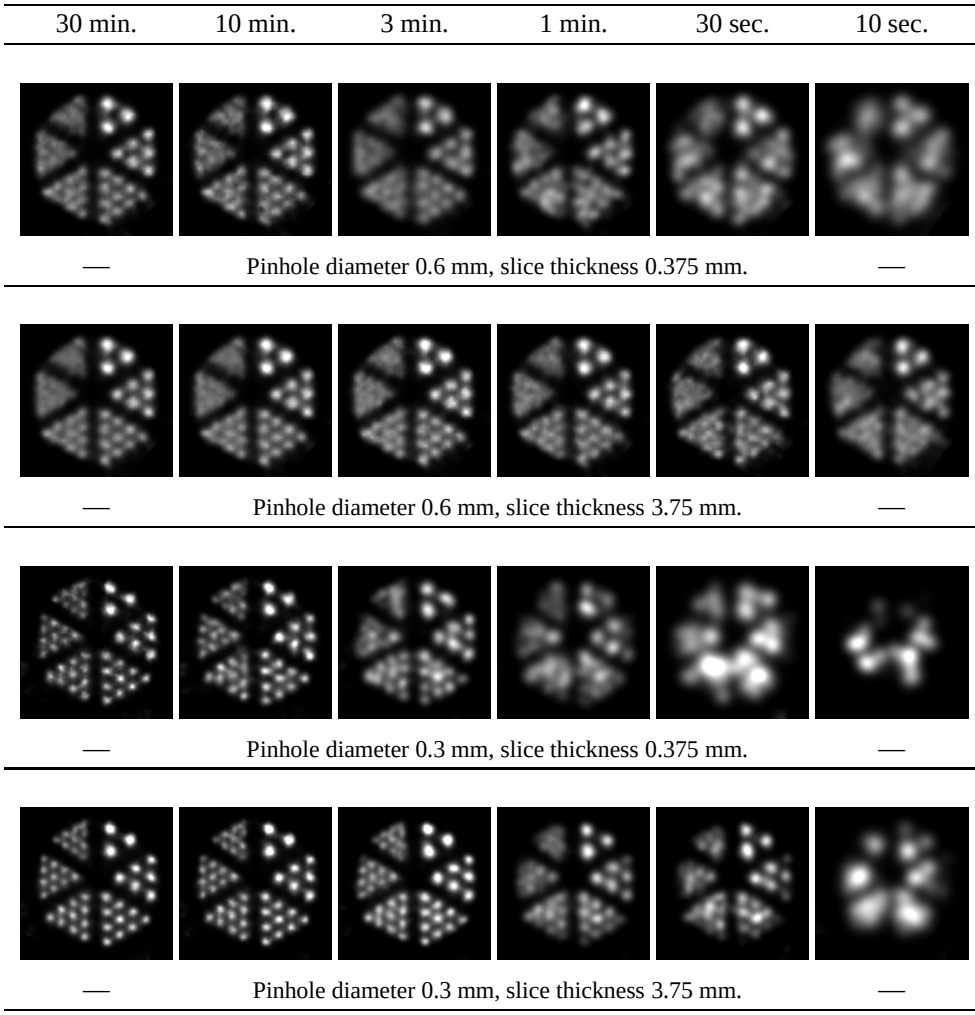

Figure 6.12: The influence of acquisition time (total number of detected counts) on the reconstructed image. This panel shows that with 0.3 mm pinholes a resolution of < 0.35 mm (0.04 μl) can be obtained. At extremely short acquisition times a resolution of 0.75 mm can still be reached. Acquisition times range from half an hour down to 10 seconds.

6.4 Discussion

In this paper we have presented a method to obtain full PSF tables (*i.e.* calibrate a system) based on a limited number of measurements and generalization of properties of PSFs over the object space. There are several methods to generalize the property values to all missing positions. In fact, our first reconstruction software for U-SPECT-I used a linear interpolation and extrapolation algorithm for filling the complete property volumes. This worked quite well to determine the matrix in a relatively small area around the field of view of the scanner. When using a scanning focus method [34] to image a larger volume, the PSFs need to be available for a larger volume inside the collimator cylinder and a generalization algorithm without any extra information cannot derive accurate PSFs, especially at locations very close to the pinholes. To be of any use such an algorithm would require so many measurement points that the whole calibration procedure would take a prohibitively long time. Therefore, we have added some geometrical information, but not as much as specifying the exact location, orientation and shape of every pinhole. The uncertainty in those is one of the reasons to use experimentally determined PSFs in the first place. Trying to find a balance between adding too little and too much geometrical information we have arrived at the parametric fit procedure described in subsection 6.2.3.

The system matrix is determined experimentally (as opposed to, *e.g.*, analytically calculated) because this automatically takes into account most physical effects that influence detection. Wide angle scatter is not incorporated in the PSF tables. However, the effects of object attenuation and scatter are much less severe in small animal imaging as in human imaging. Pinhole aperture scattering typically amounts to a few percent of the total detected counts when Tc-99m is used [40].

The example reconstruction times that were indicated, were obtained with a straightforward implementation of the ML-EM algorithm. By using block iterative algorithms (*e.g.* Ordered Subsets EM) together with faster processors with parallel processing, the reconstruction can be accelerated by more than two orders of magnitude. Since it is not always given that OS-EM methods will converge in the same way as ML-EM and the way to optimally implement them for a system such as U-SPECT is a topic of investigation on its own, we chose to use a clean ML-EM algorithm for the comparisons and results in this paper.

6.5 Conclusion

This paper presents a method to create full PSF tables for a small-animal SPECT scanner from a limited number of measurements with a point source. It is based on determining

four properties of a PSF and generalizing those properties to include all locations where no point source measurement is available. This way measurement of the PSF for all individual voxels is unnecessary. The full shape of measured PSFs can be used in generating full PSF tables (the system matrix). It is shown that the method correctly estimates the PSF at a "missing" location in a number of examples and leads to PSF tables that give sub-half-mm reconstruction results.

Using 0.6 mm pinholes, it is possible to do combine sub-minute acquisition times with sub-mm resolution. PSF tables that model the actual system more accurately *e.g.* by incorporating more of the tails, lead to better images at the cost of system matrix size.

Acknowledgments

This work was supported by the Netherlands Organization for Scientific Research (NWO), grant 917.36.335. The authors want to thank Dr Lars R Furenlid (University of Arizona) for his advice on producing the point sources used for calibration.

Bibliography

[1] K. Ishizu, T. Mukai, Y. Yonekura, M. Pagani, T. Fujita, N. Tamaki, H. Shibasaki, and J. Konishi. Ultra-high-resolution SPECT system using four pinhole collimators for small animal studies. *J. Nucl. Med.*, 26:2282–2289, 1995.

[2] D. A. Weber, M. Ivanovic, D. Franceschi, S-E. Strand, K. Erlandsson M. Franceschi, H. L. Atkins, J. A. Coderre, H. Susskind, T. Button, and K. Ljunggren. Pinhole SPECT: an approach to in vivo high resolution SPECT imaging in small laboratory animals. *J. Nucl. Med.*, 35:342–348, 1993.

[3] S. R. Meikle, R. R. Fulton, S. Eberl, M. Dahlbom, K. P. Wong, and M. J. Fulham. An investigation of coded aperture imaging for small animal SPECT. *IEEE Trans. Nucl. Sci.*, 48:816–821, 2001.

[4] D. P. McElroy, L. R. MacDonald, F. J. Beekman, Y. Wang, B. E. Patt, J. S. Iwanczyk, B. M. W. Tsui, and E. J. Hoffman. Performance evaluation of A-SPECT: A high resolution desktop pinhole SPECT system for imaging small animals. *IEEE Trans. Nucl. Sci.*, 49:2139–2147, 2002.

[5] S. D. Metzler, R. J. Jaszczak, N. H. Patil, S. Vemulapalli, G. Akabani, and B. B. Chin. Molecular imaging of small animals with a triple-head SPECT system using pinhole collimation. *IEEE Trans. Med. Im.*, 24(7):853–862, July 2005.

[6] N. U. Schramm, G. Ebel, U. Engeland, T. Schurrat, M. Béhé, and T. M. Behr. High-resolution SPECT using multipinhole collimation. *IEEE Trans. Nucl. Sci.*, 50(3):215–320, June 2003.

[7] C. Lackas, N. U. Schramm, J. W. Hoppin, U. Engeland, A. Wirrwar, and H. Halling. T-SPECT: A novel imaging technique for small animal research. *IEEE Trans. Nucl. Sci.*, 52(1):181–187, February 2005.

[8] A. L. Goertzen, D. W. Jones, J. Seidel, K. Li, and M. V. Green. First results from the high-resolution mouseSPECT annular scintillation camera. *IEEE Trans. Med. Im.*, 24(7):863–867, 2005.

[9] S. R. Meikle, P. Kench, M. Kassiou, and R. B. Banati. Small animal SPECT and its place in the matrix of molecular imaging technologies. *Phys. Med. Biol.*, 50(22):R45 – R61, 2005.

[10] K. Peremans, B. Cornelissen, B. Van Den Bossche, K. Audenaert, and C. Van de Wiele. A review of small animal imaging, planar and pinhole spect gamma camera imaging. *Veterinary radiology and ultrasound*, 46:162–170, 2005.

[11] B. M. W. Tsui and Y. C. Wang. High-resolution molecular imaging techniques for cardiovascular research. *J. Nucl. Cardiol.*, 12:261–267, 2005.

[12] F. J. Beekman and F. van der Have. The pinhole: Gateway to ultra-high resolution three-dimensional radio-nuclide imaging. *Eur. J. Nucl. Med. Molec. Im.*, 33(accepted for publication), 2006.

[13] R. K. Rowe, J. N. Aarsvold, H. H. Barrett, J. C. Chen, W. P. Klein, B. A. Moore, I. W. Pang, D. D. Patton, and T. A. White. A stationary hemispherical SPECT imager for three-dimensional brain imaging. *J. Nucl. Med.*, 34:474–480, 1993.

[14] Z. Liu, G. A. Kastis, G. D. Stevenson, H. H. Barrett, L. R. Furenlid, M. A. Kupinski, D. D. Patton, and D. W. Wilson. Quantitative analysis of acute myocardial infarct in rat hearts with ischemia-reperfusion using a high-resolution stationary SPECT system. *J. Nucl. Med.*, 43(7):933–939, 2002.

[15] L. R. Furenlid, D. W. Wilson, Y. C. Chen, H. Kim, P. J. Pietraski, M. J. Crawford, and H. H. Barrett. FastSPECT II: A second-generation high-resolution dynamic SPECT imager. *IEEE Trans. Nucl. Sci.*, 51(3):631–635, June 2004.

[16] F. J. Beekman, F. van der Have, B. Vastenhouw, A. J. A. van der Linden, P. P. van Rijk, J. P. H. Burbach, and M. P. Smidt. U-SPECT-I: A novel system for submillimeter-resolution tomography with radiolabeled molecules in mice. *J. Nucl. Med.*, 46(7):1194 – 1200, July 2005.

[17] F. J. Beekman and B. Vastenhouw. Design and simulation of a high-resolution stationary SPECT system for small animals. *Phys. Med. Biol.*, 49:4579–4592, 2004.

[18] G. K. Kastis, H. B. Barber, H. H. Barrett, H. C. Gifford, I. W. Pang, D. D. Patton, G. Stevenson, and D. W. Wilson. High resolution SPECT imager for three-dimensional imaging of small animals (abstract). *J. Nucl. Med.*, 39:9P, 1998.

[19] B. Vastenhouw, F. van der Have, A. J. A. van der Linden, L. von Oerthel, J. Booij, J. P. H. Burbach, M. P. Smidt, and F. J. Beekman. Movies of dopamine transporter occupancy with ultra-high resolution focusing pinhole SPECT. *Molecular Psychiatry*, page (in press), 2007.

[20] E. P. Ficaro, J. A. Fessler, P. D. Shreve, J. N. Kritzman, P. A. Rose, and J. R. Corbett. Simultaneous transmission/emission myocardial perfusion tomography. Diagnostic accuracy of attenuation-corrected 99mTc-sestamibi single-photon emission computed tomography. *Circulation*, 93:463–473, 1996.

[21] F. J. Beekman, C. Kamphuis, and E. C. Frey. Scatter compensation methods in 3D iterative SPECT reconstruction: A simulation study. *Phys. Med. Biol.*, 42:1619–1632, 1997.

[22] C. E. Floyd, R. J. Jaszczak, K. L. Greer, and R. E. Coleman. Inverse Monte Carlo as a unified reconstruction algorithm for ECT. *J. Nucl. Med.*, 27(10):1577–1585, 1986.

[23] D. J. Kadrmas, E. C. Frey, S. S. Karimi, and B. M. W. Tsui. Fast implementation of reconstruction based scatter compensation in fully 3D SPECT image reconstruction. *Phys.Med.Biol.*, 43:857–873, 1998.

[24] B. M. W. Tsui, E. C. Frey, K. J. LaCroix, D. S. Lalush, W. H. McCarthy, M. A. King, and G. T. Gullberg. Quantitative myocardial perfusion SPECT. *J. Nucl. Card.*, 5:507–522, 1998.

[25] J. Y. Li, R. J. Jaszczak, H. L. Wang, K. L. Greer, and R. E. Coleman. Determination of both mechanical and electronic shifts in cone-beam SPECT. *Phys. Med. Biol.*, 38(6):743–754, 1993.

[26] P. Rizo, P. Grangeat, and R. Guillemaud. Geometric calibration method for multiple-head cone-beam SPECT system. *IEEE Trans. Nucl. Sci.*, 41(6):2748–2757, 1994.

[27] F. Noo, R. Clackdoyle, C. Mennessier, T. A. White, and T. J. Roney. Analytic method based on identification of ellipse parameters for scanner calibration in cone-beam tomography. *Phys. Med. Biol.*, 45(11):3489–3508, 2000.

[28] D. Beque, J. Nuyts, G. Bormans, P. Suetens, and P. Dupont. Characterization of pinhole SPECT acquisition geometry. *IEEE Trans. Nucl. Sci.*, 22(5):599–612, 2003.

[29] D. Beque, J. Nuyts, P. Suetens, and G. Bormans. Optimization of geometrical calibration in pinhole SPECT. *IEEE Trans. Med. Im.*, 24(2):180–190, 2005.

[30] S. D. Metzler, K. L. Greer, and R. J. Jaszczak. Determination of mechanical and electronic shifts for pinhole SPECT using a single point source. *IEEE Trans. Med. Im.*, 24(3):361–370, 2005.

[31] S. D. Metzler and R. J. Jaszczak. Simultaneous multi-head calibration for pinhole SPECT. *IEEE Trans. Nucl. Sci.*, 53(1):113–120, 2006.

[32] Y.-C. Chen, L. R. Furenlid, D. W. Wilson, and H. H. Barrett. *Small-Animal SPECT imaging*, chapter 12, pages 195–201. Springer, New York, 2005.

[33] J. Y. Hesterman, M. A. Kupinski, L. R. Furenlid, D. W. Wilson, and H. H. Barrett. The multi-module, multi-resolution system (M^3R): A novel small-animal SPECT system. *Med. Phys.*, 34(3):987–993, 2007.

[34] B. Vastenhouw and F. J. Beekman. Sub-mm total-body murine imaging with U-SPECT-I. *J. Nucl. Med.*, page (accepted), 2007.

[35] F. van der Have, B. Vastenhouw, M. C. M. Rentmeester, and F. J. Beekman. System calibration and statistical image reconstruction for sub-mm stationary pinhole SPECT. *Conference Record of the 2005 Nuclear Science Symposium and Medical Imaging Conference, Puerto Rico*, pages M11–291, 2005.

[36] F. van der Have, B. Vastenhouw, and F. J. Beekman. U-SPECT-II: a versatile sub-half-mm resolution small animal SPECT system. *Society of Nuclear Medicine conference 2007, Washington D.C.*, 2007.

[37] F. J. Beekman. A method for obtaining a tomographic image, including an apparatus. *PCT-application WO02093195, Submitted at May 8, 2002*, 2002.

[38] F. J. Beekman. Werkwijze voor het verkrijgen van een tomografische afbeelding, alsmede een inrichting. *Dutch patents 1018060 and 1019666, US patent US7145153 B2 granted 2006-12-05. Submission May 11, 2001*, 2001.

[39] A. P. Colijn and F. J. Beekman. Accelerated simulation of cone beam X-ray scatter projections. *IEEE Trans. Med. Im.*, 23(5):584–590, 2004.

[40] F. van der Have and F. J. Beekman. Photon penetration and scatter in micro-pinhole imaging: a Monte Carlo investigation. *Phys. Med. Biol.*, 49:1369–1386, 2004.

Chapter 7

U-SPECT-I: A novel system for submillimeter-resolution tomography with radiolabeled molecules in mice

F J Beekman, F van der Have, B Vastenhouw, A J A van der Linden, P P van Rijk, J P H Burbach, and M P Smidt

J Nucl Med 2005; 46: 1194–1200.

Abstract

A major advance in biomedical science and diagnosis was accomplished with the development of *in vivo* techniques to image radiolabeled molecules, but limited spatial resolution has slowed down applications to small experimental animals. Here, we present a SPECT system (U-SPECT-I) dedicated to radionuclide imaging of murine organs at a submillimeter resolution. **Methods**: The high performance of U-SPECT-I is based on a static triangular detector setup, with a cylindric imaging cavity in the center and 75 gold micropinhole apertures in the cavity wall. The pinholes are focused on a small volume of interest such as the mouse heart or spine to maximize the detection yield of -photons. Three-dimensional molecular distributions are iteratively estimated using the detector data and a statistical reconstruction algorithm that

takes into account system blurring and data noise to increase resolution and reduce image noise. **Results**: With 0.6-mm-diameter pinholes, the maximum fraction of detected photons emitted by a point source (peak sensitivity) is 0.22% for a 15%-wide energy window and remains higher than 0.12% in the central 12 mm of the central plane. In a resolution phantom, radioactively filled capillaries as small as 0.5 mm and separated by 0.5 mm can be distinguished clearly in reconstructions. Projection data needed for the reconstruction of cross sections of molecular distributions in mouse organs can readily be obtained without the need for any mechanical movements. Images of a mouse spine show Tc99m-hydroxymethylene diphosphonate uptake down to the level of tiny parts of vertebral processes. These are separated clearly from the vertebral and intervertebral foramina. Using another tracer, one can monitor myocardial perfusion in the left and right ventricular walls, even in structures as small as the papillary muscles. **Conclusion**: U-SPECT-I allows discrimination between molecular concentrations in adjacent volumes of as small as about 0.1 μL, which is significantly smaller than can be imaged by any existing SPECT or PET system. Our initial *in vivo* images of the mouse heart and spine show that U-SPECT-I can be used for novel applications in the study of dynamic biologic systems with a clear projection to clinical applications. The combination of high resolution and detection efficiency of U-SPECT-I opens up new possibilities for the suborgan-level study of radiotracers in mouse models.

7.1 Introduction

Dedicated SPECT and PET instruments (1) in concert with the radiolabeling of small molecules, antibodies, peptides, and probes for gene expression have facilitated *in vivo* assessment of molecular mechanisms and the development of new tracers and pharmaceuticals (2–6). Recent developments in this multidisciplinary field of molecular imaging have initiated a revolution in biomedical sciences. A bottleneck in the assessment of molecular mechanisms at the suborgan scale is the limited spatial resolution of available SPECT and PET instruments. In practice, the resolution in living animals is presently limited to tissue volumes of about 1 μL (*e.g.*, (7)) but is often an order of magnitude larger. The increasing availability of genetically modified mice as models for human disease prompts studies with SPECT and PET. However, improving image resolution and dynamic capabilities is essential to fully exploit the disease models and tracers available.

SPECT systems using pinhole apertures permit radiolabeled molecular distributions to be imaged *in vivo* in small animals. Several pinhole-SPECT systems have been designed and constructed in recent years (8–14). In addition to SPECT systems, dedicated small-animal PET systems have been devised for the imaging of radiolabeled molecules (15). The

applications of SPECT and PET partly overlap and often are complementary. The method used for a particular application depends on factors such as equipment costs, infrastructure, required resolution, and counting sensitivity and also is influenced by logistics, costs, and the availability of the specific radiomolecules required.

With micropinhole radionuclide imaging, it becomes possible to obtain high-spatial-resolution projection data, particularly for small organs that can be positioned near the pinhole. For example, a study has shown that the thyroid of a living mouse (typical size, 1×1 mm) can be imaged at a resolution of as good as 0.2 mm using planar pinhole cameras (16). However, a drawback of contemporary pinhole SPECT, compared with PET, is the limited ability to detect a good fraction of the emitted γ-photons. This counting sensitivity decreases further when smaller pinholes are used to increase image resolution. With low counting sensitivity, the high-resolution information content of projection data cannot be fully exploited since reconstructed volumes calculated from these projections tend to be noisy and visual interpretation is possible only after resolution-degrading smoothing operations. These often result in a resolution that is significantly worse than that of images obtained with small-animal PET.

The goal of the present paper is the launching of a dedicated mouse SPECT system (U-SPECT-I), developed at University Medical Center Utrecht, that defines a new front line of small-animal SPECT characteristics through a design that enables one to exploit the high-resolution content of pinhole projection data. U-SPECT-I is stationary in the sense that there is no need for moving any of the parts, such as the detector and the collimator, or the animal. The resultant advantages include system stability, simplicity of system design, the flexibility of performing dynamic studies with any frame-time (14,17,18), and ease of animal handling and positioning. In addition, U-SPECT-I is designed such that all pinholes focus on a small area. In this way, a specific object area is adequately magnified on the detector plane, whereas only a limited part of the detector surface available is required for creating each mini camera. The use of all these independent mini cameras together results in a significantly higher sensitivity, thus overcoming a fundamental problem of micropinhole imaging. The system is based on conventional scintillation γ-cameras that are part of a clinical SPECT system (Prism 3000 S; Picker Medical Systems) and has the flexibility to be switched back rapidly to the original clinical imaging setup. Validation of the system design and its outstanding imaging characteristics is demonstrated through imaging of specific phantoms and mouse organs.

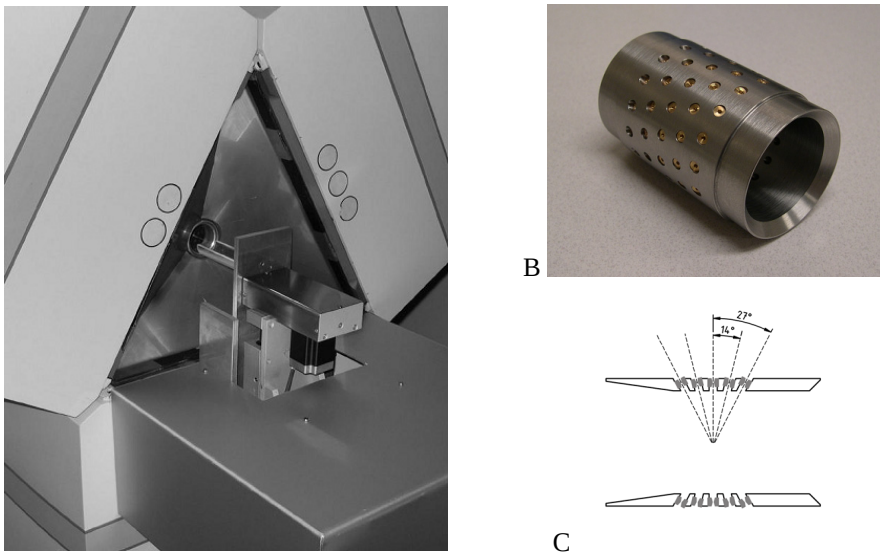

Figure 7.1: (A) Overview of U-SPECT-I system. Triangular lead shielding is placed between camera heads of triple-detector system, tungsten cylinder containing pinholes being centered within the 3 detectors. x,y,z stage with attached bed, placed in front of lower detector, is also visible. (B) Cylinder with 75 gold pinhole apertures that are focused on its center. (C) Cross section of cylinder with tilted pinholes.

7.2 Materials and methods

In this section, we describe the U-SPECT-I system geometry (composition and positioning of pinholes and detectors), the image reconstruction methods, the physical phantom experiments, and the animal experiments that proved the system performance.

7.2.1 Pinhole Design and Geometry of U-SPECT-I

Figure 7.1A shows an overview of the U-SPECT-I system, in which the detectors of a triple-head SPECT system (with clinical collimators removed) are used as a detector ring. A cylinder with 75 gold pinholes is placed in the center (Figs. 7.1B and 7.1C). The pinhole apertures are placed in a 5-fold ring geometry, with each ring containing 15 pinhole apertures. Compared with commonly used lead or tungsten, the gold pinhole apertures have high photon-stopping power, thus reducing blurring caused by radiation penetration and scattering in the aperture edge material (19). In contrast to the earlier-proposed depleted uranium, which has an even better stopping power, gold pinholes can be manufactured quite easily in high quan-

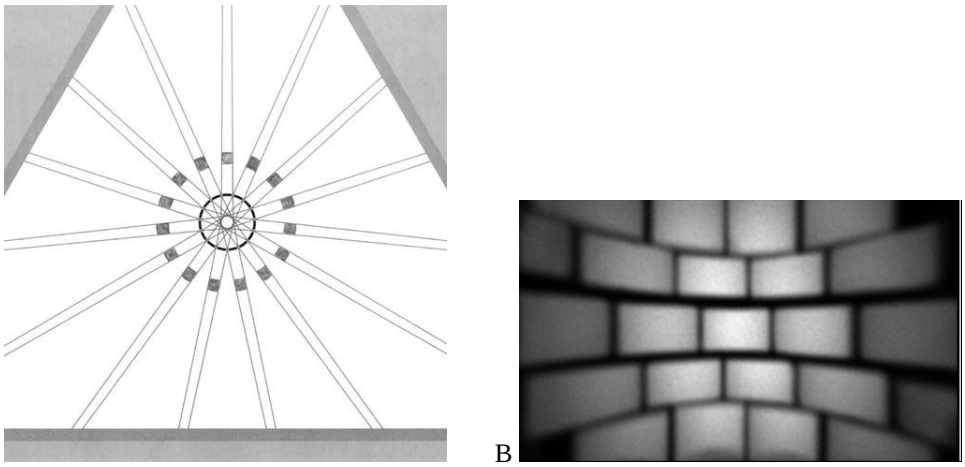

Figure 7.2: Illustration of highly focusing pinhole geometry of U-SPECT-I. (A) Cross section through 1 of 5 rings with pinholes. Lines emerging from central circle mark triangular cross sections of beams in which emitted γ-quanta can travel from animal toward detector. Pinholes in all rings focus on center to maximize detection yield. Lead cylinder with square holes shown in gray is placed around tungsten cylinder with pinholes to prevent projection overlap. (B) Radiation intensity on 1 of 3 detectors when a bottle with a Tc-99m solution is imaged. Image demonstrates how the large detector is divided into a large number of small subcameras.

tities and are not radioactive or poisonous. The high-photon-counting sensitivity obtained with the large number of pinholes can be traded for increased image resolution by the use of relatively small pinholes (0.6 mm diameter). The pinholes have knife edges and an opening angle of 30 °, with shielding placed in such a way that projections do not overlap (Fig. 7.2A). The shielding consists of a lead tube with square holes defining the edges of the projections (Fig. 7.2B).

A cross section through the detector and the central ring with pinholes is shown in figure 7.2A. The edges of the 15 photon beams passing through the 15 pinholes in this ring are indicated by lines that diverge from the individual pinholes toward the detector and toward the center of the cylinder. All pinholes in the various rings focus on the center. The apertures in the outer rings are placed at a wider angle to the transaxial axis. In this way, voxels in the central field of view can be observed via 69 pinholes simultaneously (6 of the 75 pinhole cameras are partly or completely blind because of a missing area of active crystal close to the camera edges in the corners of the triangle). The pinhole positions in adjacent

rings are rotated over 8 ° to increase the variety of angles at which each voxel is observed. The projections of the object area observed by different pinholes do not overlap. Overlap is prevented by placing a lead tube with 75 rectangular holes around the tungsten pinhole cylinder. The diameter of the rings with pinholes is 44 mm when measured at the centers of the pinhole openings. The intrinsic resolution of the γ-cameras was determined to be 3.2 mm in full width at half maximum as measured with a line-shaped beam (140 keV).

7.2.2 Image Reconstruction and Calibration

U-SPECT-I images were reconstructed using 150-iteration maximum-likelihood expectation maximization (20). Point spread functions (PSFs) of the system were used during maximum-likelihood expectation maximization to model the probability that a photon from a certain object position will be detected by a specific detector pixel. PSFs were measured using a 60 MBq point source. The point source was produced from a chromatographic bead, which was approximately 1 voxel. Small amounts (10–15 μL) of concentrated (approximately 4 GBq/mL) pertechnetate were added 10–15 times, and the liquid was evaporated by being heated to about 60 °C. The point source was attached to its holder by a fast-curing epoxy resin.

Each PSF is part of the transition matrix, which is stored entirely on disk. Because one considers entire PSFs during reconstruction, instead of assuming a line integral through the center of each pinhole, the effects of blurring due to pinhole diameter and pinhole penetration and of blurring intrinsic to the detector are corrected for during reconstruction. Other advantages of direct measurement of PSFs are that it obviates separate calibration of mechanical (detector and collimator) and electronics offsets and correction of uniformity and linearity.

The measured PSFs over all voxels in the cylinder together represent the entire system matrix needed during iterative reconstruction of the image. A similar method has been used to calibrate the FASTSPECT system of the University of Arizona (18). With the U-SPECT-I system, the voxel size used in reconstructions is small (0.1875 mm). The projection pixel size used for all measurements reported in this paper was 0.898 mm. Because it would be time consuming to separately measure the PSF for each voxel position in the pinhole cylinder, we measured the PSF in a subset of voxels in the object using an x, y, z stage and a grid of 7 $\times$ 7 $\times$ 11 points with a spacing of 3 mm, 3 mm, and 1.5 mm, respectively. For each measured PSF, we first estimated 3 basic properties: the coordinates of the maximum on the detector, the flux, and the width. Using linear interpolation and extrapolation, we estimated and stored the properties of the missing PSFs.

7.2.3 Study of System Characteristics

Position-dependent point-source sensitivity in the collimator ring was measured using the same scanning point source as used for system calibration. The sensitivity profiles presented in Figure 7.3 were acquired over 3 mutually perpendicular axes, each crossing the center of the field of view, and were obtained with a 15% energy window.

A miniature acrylic resolution phantom (Derenzo phantom) was manufactured. It contained 6 sectors, each containing equally sized sets of capillaries (0.4, 0.5, 0.6, 0.7, 0.8, and 1.0 mm). Each capillary was 10 mm long, the total activity in all capillaries together was 11.1 MBq of Tc-99m, and the data acquisition time was 30 min. The distance between the rods equaled the rod diameter. The phantom diameter was 12 mm. The spatial resolution in such phantoms is often defined by the size of capillaries that can be observed separately.

7.2.4 Animal Studies

Animal studies were conducted following protocols approved by the Animal Research Committee of the University Medical Center Utrecht. Three-month-old C57BL/6JO1aHsd mice (body weight, 25–30 g; Harlan) were anesthetized with a mix of 2.5 mL of Hypnorm (fentanyl, 0.315 mg/mL, and fluanisone, 10 mg/mL; Janssen), 2.5 mL of Dormicum (midazolam, 5 mg/mL; Roche), and 5 mL of Aquadest, administered intraperitoneally, per kilogram of body weight. Thereafter, the radionuclide of interest (0.2 mL solution) was injected into the tail vein. The radionuclides tested were Tc-99m-hydroxymethylene diphosphonate (HDP) for bone imaging and Tc-99m-tetrofosmin for cardiac perfusion imaging. During the entire procedure, animal body temperature was kept at 37 °C.

7.3 Results

7.3.1 Ultrahigh System Sensitivity and Image Resolution

Sensitivity, here expressed as the percentage of emitted γ-quanta that are detected, depends on the pinhole diameter, the number of pinholes, and the distance of the pinholes to the object (21,22). The peak sensitivity with 0.6-mm pinholes was measured to be 0.22% in the central field of view and remained 0.12% within a central transaxial disk with a 12-mm diameter (Fig. 7.3). Sensitivities of other small-animal SPECT systems are typically more than an order of magnitude lower when compared at equal geometric system resolution, because of a low number of pinholes or the less-focusing architecture. High sensitivity is crucial to avoid noisy data and therefore to avoid excessive resolution- degrading low-pass filtering for

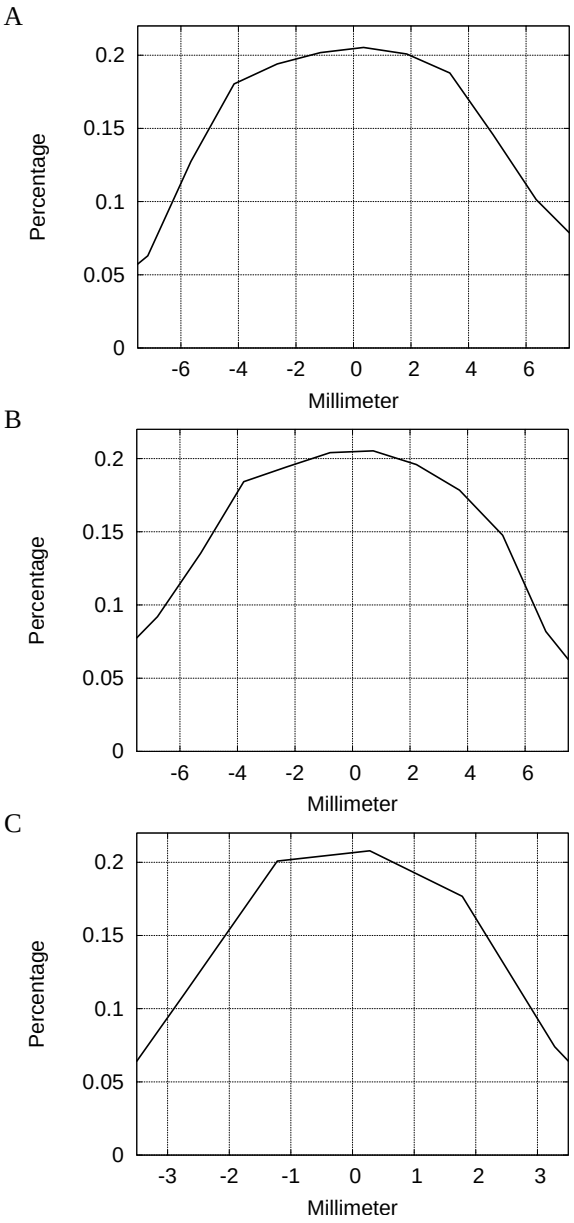

Figure 7.3: Demonstration of high sensitivity of U-SPECT-I. Shown are sensitivity profiles lying along mutually orthogonal lines that cross the center of field of view, obtained with a scanning point source: along x-axis (A), along y-axis (B), and along transaxial axis (z-axis) (C).

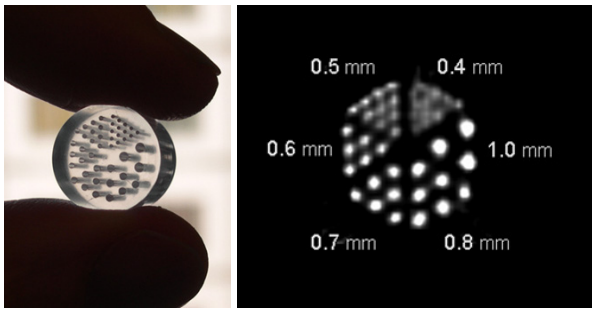

Figure 7.4: Demonstration of submillimeter resolution of U-SPECT-I images. (A) Photograph of miniature acrylic resolution phantom with capillaries used as test object. (B) Reconstructed cross-sectional image, with a slice thickness of 0.5 mm, of the phantom shown in A. Half-millimeter capillaries are clearly separated in the image.

enhancing the appearance of otherwise-noisy reconstructed images. For any pinhole system, the sensitivity can be increased at the cost of system resolution, by enlarging the pinholes.

Imaging of the miniature resolution phantom during 30 min resulted in reconstructions clearly resolving the set of 0.5-mm capillaries (Fig. 7.4). Even some of the 0.4 mm capillaries could be identified. This result indicates that differences in molecular uptake between tiny neighboring tissue volumes on the order of 0.1 μL can readily be distinguished. Note that the smallest capillaries resolved with state-of-the-art PET scanners are approximately 1 mm (7) when advanced statistical reconstruction is applied.

7.3.2 Ultra-High-Resolution Images of Radiomolecules in Live Mice

To show that highly detailed imaging can be extrapolated from test objects to live animals, we acquired images of mice with 2 different tracers often used in clinical SPECT studies. Figure 7.5 shows 3 perpendicular cross sections of a myocardial perfusion volume image obtained with Tc-99m-tetrofosmin. Myocardial perfusion in both the left and the right ventricular walls is clearly visible. Perfusion in the anterior papillary muscle within the left ventricle was readily distinguished in the short-axis slice (arrow). The level of detail presented here may lead to new experimental opportunities in cardiology.

A second experiment was performed to show bone metabolism within a mouse lumbar spine (Fig. 7.6). Three 0.25- mm-thick orthogonal slices through the spine are presented.

A projection of local image maxima (maximum-intensity projection) and isosurface renderings were calculated from the same reconstructed 3-dimensional tracer distribution. Tc-99m-HDP uptake in tiny parts of the individual processes and other tiny vertebral parts was

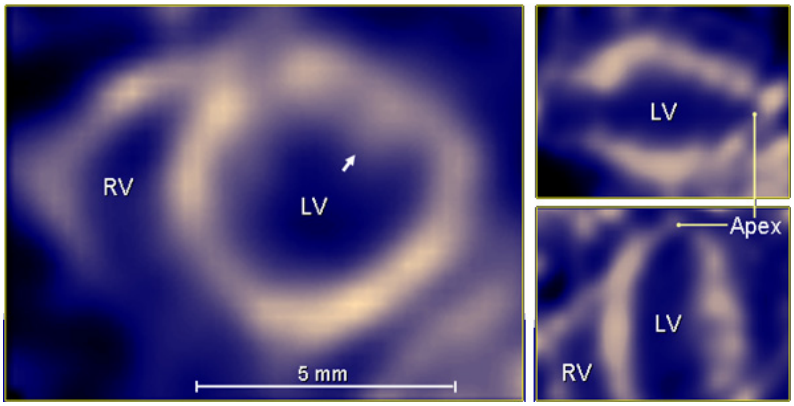

Figure 7.5: Mutual perpendicular cross sections through submillimeter- resolution 3-dimensional myocardial perfusion image volume of living mouse (named Animal Co-Image of the Year at the annual meeting of the Society of Nuclear Medicine, Philadelphia, 2004). Image data were acquired during 30 min, starting 30 min after administration of 222 MBq (6 mCi) of Tc-99m-tetrofosmin. On left is a short-axis slice showing myocardial perfusion in right ventricular (RV) and left ventricular (LV) walls. Perfusion in anterior papillary muscle (arrow) can be distinguished from other parts of left ventricular wall. At top right is a vertical long-axis slice; at bottom right, a horizontal long-axis slice. In color print in the appendix.

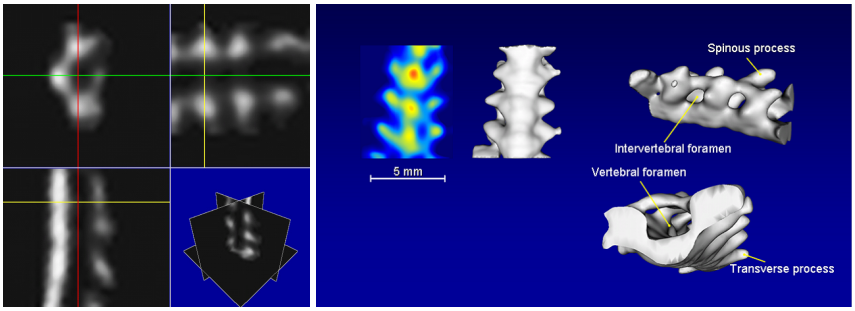

Figure 7.6: Different representations of reconstructed image volume of lumbar spine, acquired during 22 min, 2 h after injection of 148 MBq (4 mCi) of Tc-99m-HDP. (A) Three different orthogonal cross sections. (B) Projection of local image maxima (far left) and 3 isosurface renderings of tracer concentrations in same spinal section (named Animal Co-Image of the Year at the annual meeting of the Society of Nuclear Medicine, Philadelphia, 2004). In color print in the appendix.

readily visualized. Also, the spaces between and within the vertebrae, intervertebral foramen, and vertebral foramen that do not take up Tc-99m- HDP were clearly distinguished from bone tissue, particularly in the isosurface renderings. Because uptake of Tc-99m- HDP-like agents is very much influenced by changes in bone remodulation, such as those caused by mechanical strain or tumor growth, the type of detailed imaging shown here may initiate new research opportunities in locomotion, bone, and cancer research.

7.4 Discussion

In this paper, we have described a new SPECT system that has a highly focused pinhole architecture resulting in high-resolution molecular imaging. Even with standard detectors with an intrinsic resolution of 3.2 mm, SPECT images with a resolution better than 0.5 mm were obtained, without the optimizing of pinhole diameters. U-SPECT-I, and its successors with an even higher resolution, will allow the 3-dimensional assessment of distributions of a wide range of radiolabeled tracers. Labor-intensive in vitro or ex vivo methods may be replaced in several cases by the imaging of intact animals on the submillimeter level, also allowing for accurate longitudinal study designs, instrumental for development of new diagnostic or therapeutic agents. Importantly, U-SPECT-I allows noninvasive imaging of mice with radionuclides and associated radiomolecules, many of which are already approved for clinical use. On the other hand, novel imaging applications and tracer biology developed in mice can readily be applied to the clinical setting, in which radionuclide imaging methods such as SPECT are already in common use.

The present U-SPECT-I system has an outstanding sensitivity/ resolution trade-off, with a field of view that is large enough to cover most essential mouse organs, such as the entire midbrain, the mouse heart, or the lumbar spine. Often only small fields of view are required. The advantage of the focusing setup is that one can acquire many photons from a specific area of interest. As we have shown, this helps to produce a high image resolution. It is possible to extend the field of view without changing the pinhole geometry: The bed has then to be shifted in order to focus the pinholes on different areas of the animal. As a result, the area with highest sensitivity is scanned through the volume of interest in the animal. The most trivial way to extend the field of view is to stitch together the smaller images calculated from separate acquisitions, as is often done in clinical procedures. However, we have devised a more promising solution that consists of a combined reconstruction and acquisition strategy that simultaneously takes into account all projection data from different bed positions and produces the entire image volume from a single reconstruction (23). With this method, it may be possible to extend the useful field of view to the entire central nervous system of a

mouse by using no more than 2 bed positions. Positions can be alternated sufficiently rapidly by shifting back and forth the tiny bed instead of the heavy detectors, enabling dynamic studies with an extended field of view.

Another way to extend the field of view of the U-SPECT-I system is to remove the cylindric shielding between the pinholes and the detector (Fig. 7.2A). As a result, the projections will overlap to a certain extent, the degree of which will depend on the shape of the pinholes, such as the opening angle and type of edge. Systems with overlapping projections (*e.g.*, (12)) have another interesting feature: They can detect a larger fraction of the emitted photons while activity that is concentrated in small areas such as small tumors can still be projected on separate areas on the detector. On the other hand, for the extended distributions that are more common in biology, the overlap of patterns on the detector will lead to significant loss of information about the emission direction of each detected γ-quantum. Whether the increase in detection probability obtained by overlap will compensate for such an information loss strongly depends on the specific distribution of the molecules to be imaged, on the amount of projection overlap, and on the number of detected photons. These will be important factors determining whether the same increase of sensitivity might be better obtained by using larger pinholes instead of more pinholes combined with overlap. Comparisons of the image quality of systems with overlapping projections and with nonoverlapping projections will be a research subject of continuing interest. In addition, several novel (hybrid) projection strategies are currently being developed in our laboratory.

An important cause of the low sensitivity of previously proposed pinhole SPECT systems is that the γ-detection depends on traditional Anger scintillation cameras with a typical intrinsic resolution of approximately 2.0–4.0 mm. Higher-resolution detectors are still extremely expensive if they are required to cover a large area. The problem of limited detector resolution is bypassed with pinhole SPECT, through the application of a significant magnification of the animal via the pinhole on the detector. For adequately magnified projection of a large part of the animal, one needs a large detector surface area. This is why in almost all systems only a few pinhole cameras are placed around the animal; more pinholes would cause overlapping of the projections. With a few pinholes, the resulting bulky cameras need to be rotated to obtain projections at a sufficient number of angles. The required mechanics complicate these SPECT systems and make them difficult to calibrate. In addition, systems requiring detector rotation have only limited flexibility in acquiring and processing dynamic series.

The design of U-SPECT-I allows for stationary acquisition of projection data, similar to the type of acquisitions possible with the FASTSPECT system (18) and PET systems. Together with the high sensitivity achieved with the high number of pinholes, U-SPECT-I will enable researchers to perform dynamic studies on mice, and users will have greater

flexibility in choosing frame time a posteriori. Additionally the design, having no moving parts, will reduce maintenance and may simplify system calibration.

Previous simulation studies (14) of stationary small-animal SPECT devices have indicated that the results with higher-resolution detectors will be significantly better than those presented here, that the focused pinhole geometry with nonoverlapping projection views brings us closer to satisfying Orlov's conditions for adequate sampling of data (24) than do traditional pinhole SPECT systems, and that this is important for producing better results than are possible with traditional pinhole SPECT systems that acquire projections over a single orbit.

U-SPECT-I is based on the use of a triangular scintillation detector setup "borrowed" from a system currently in use for routine clinical SPECT. The entire transformation from U-SPECT-I back to the clinical system takes about 10 min, and no extra calibrations are required between the switching from clinical to animal imaging device. Therefore, the U-SPECT-I design is extremely cost-effective and can universally be applied to clinical SPECT systems. Ultimately, however, stationary SPECT systems may comprise a detector ring or a spheric layer (a sphere concluded by 2 planes), approximated by a polygon that is formed by high-resolution detectors, such as in the U-SPECT-III design (14). High-resolution detectors are under development by several groups (*e.g.*, (25–29)). A next step in U-SPECT evolution will be the application of such detectors. U-SPECT-III has already been tested in simulations, but the costs and availability of detectors are restrictive. Simulation results point to marked progress in small-animal SPECT instrumentation over the next couple of years.

7.5 Conclusion

U-SPECT-I defines a new front line in small-animal SPECT. It is a fully functional, dedicated small-animal SPECT system with an outstanding volumetric resolution on the order of 0.1 μL. Results indicate that resolution is significantly better with U-SPECT-I than with state-of-theart small-animal SPECT and PET systems. The system allows for assessing tracer dynamics in suborgans of the living mouse, as was illustrated by *in vivo* images showing submillimeter details of molecular uptake in the myocardium and vertebrae. The high resolution, high sensitivity, and relatively low hardware costs of U-SPECT-I should now allow detailed molecular imaging to be applied successfully to a wide range of study types, thus creating a broad range of new experimental opportunities. Significant improvements in image quality are expected when the triangular detector setup of U-SPECT-I is replaced by high resolution detectors.

7.6 Acknowledgments

This work was sponsored by the Medical Council of The Netherlands Organization for Scientific Research, grant 917.36.335. We thank Dr. Lars Furenlid for showing us how to make concentrated point sources and Dr. Simon Cherry for introducing Dr. Freek Beekman to the microimaging world. Gijs van der Wilt, Cees van der Linden, Henk te Biesebeek, Jan Brakkee, and Cora de Bruijn are thanked for technical assistance. Dr. Theo van Walsum is thanked for assistance with image display.

References

1. King MA, Pretorius PH, Farncombe T, Beekman FJ. Introduction to the physics of molecular imaging with radioactive tracers in small animals. J Cell Biochem. 2002;39(suppl):221–230.

2. Gambhir SS, Herschman HR, Cherry SR, et al. Imaging transgene expression with radionuclide imaging technologies. Nature Neoplasia. 2000;2:118–138.

3. Phelps ME. Inaugural article: positron emission tomography provides molecular imaging of biological processes. Proc Natl Acad Sci USA. 2000;97:622–6233.

4. Weissleder R. Scaling down imaging: molecular mapping of cancer in mice. Nature Rev Cancer. 2002;2:11–18.

5. Rudin M, Weissleder R. Molecular imaging in drug discovery and development. Nature Rev Drug Discov. 2003;2:123–131.

6. Shah K, Jacobs A, Breakefield XO, Weissleder R. Molecular imaging of gene therapy for cancer. Gene Ther. 2004;11:1175–1187.

7. Yang Y, Tai YC, Siegel S, et al. Optimization and performance evaluation of the microPET II scanner for in vivo small-animal imaging. Phys Med Biol. 2004;49: 2527–2545.

8. Jaszczak RJ, Li J, Wang H, Zalutsky MR, Coleman RE. Pinhole collimation for ultra-high-resolution small-field-of-view SPECT. Phys Med Biol. 1994;39:425– 437.

9. Ishizu K, Mukai T, Yonekura Y, et al. Ultra-high-resolution SPECT system using four pinhole collimators for small animal studies. J Nucl Med. 1995;26:2282– 2289.

10. Weber DA, Ivanovic M. Ultra-high-resolution imaging of small animals: implications for preclinical and research studies. J Nucl Cardiol. 1999;6:332–344.

11. Wu MC, Tang HR, Gao DW, et al. ECG gated pinhole SPECT in mice with millimeter resolution. IEEE Trans Nucl Sci. 2000;47:1218–1227.

12. Meikle SR, Fulton RR, Eberl S, Dahlbom M, Wong KP, Fulham MJ. An investigation of coded aperture imaging for small animal SPECT. IEEE Trans Nucl Sci. 2001;48:816–821.

13. McElroy DP, MacDonald LR, Beekman FJ, et al. Performance evaluation of A-SPECT: a high resolution desktop pinhole SPECT system for imaging small animals. IEEE Trans Nucl Sci. 2002;49:2139–2147.

14. Beekman FJ, Vastenhouw B. Design and simulation of a high-resolution stationary SPECT system for small animals. Phys Med Biol. 2004;49:4579–4592.

15. Chatziioannou A. Molecular imaging of small animals with dedicated PET tomographs. Eur J Nucl Med Mol Imaging. 2002;29:98–114.

16. Beekman FJ, McElroy DP, Berger F, Gambhir SS, Hoffman EJ, Cherry SR. Towards in vivo nuclear microscopy: I-125 imaging in mice using micro-pinholes. Eur J Nucl Med Mol Imaging. 2002;29:933–938.

17. Rowe RK, Aarsvold JN, Barrett HH, et al. A stationary hemispherical SPECT imager for three-dimensional brain imaging. J Nucl Med. 1993;34:474–480.

18. Liu Z, Kastis GA, Stevenson GD, et al. Quantitative analysis of acute myocardial infarct in rat hearts with ischemia-reperfusion using a high-resolution stationary SPECT system. J Nucl Med. 2002;43:933–939.

19. van der Have F, Beekman FJ. Photon penetration and scatter in micro-pinhole imaging: a Monte Carlo investigation. Phys Med Biol. 2004;49:1369–1386.

20. Lange K, Carson R. E.M. reconstruction algorithms for emission and transmission tomography. J Comput Assist Tomogr. 1984;8:306–316.

21. Metzler SD, Bowsher JE, Smith MF, Jaszczak RJ. Analytic determination of pinhole collimator sensitivity with penetration. IEEE Trans Med Imaging. 2001; 20:730–741.

22. Accorsi R, Metzler SD. Analytic determination of the resolution-equivalent effective diameter of a pinhole collimator. IEEE Trans Med Imaging. 2004;23: 750–763.

23. Beekman FJ, Vastenhouw B, van der Have F. Towards 3D nuclear microscopy using locally focusing many-pinhole SPECT. In: Proceedings of the 2003 International Meeting on Fully Three-Dimensional Image Reconstruction in Radiology and Nuclear Medicine. Brest, France: Brest University Press; 2004:262–264.

24. Orlov SS. Theory of three-dimensional reconstruction. I. Conditions for a complete set of projections. Sov Phys Crystallogr. 1975;20:429–433.

25. Matherson KJ, Barber HB, Barrett HH, et al. Progress in the development of larger-area modular 64x64 CdZnTe imaging arrays for nuclear medicine. IEEE Trans Nucl Sci. 1998;45:354–358.

26. He Z, Li W, Knoll GF, Wehe DK, Stahle CM. 3-D position sensitive CdZnTe gamma-ray spectrometers. Nucl Instrum Methods Phys Res A. 1999;422:173– 178.

27. Llopart X, Campbell M, Dinapoli R, Segundo DS, Pemigotti E. Medipix2: a 64-k pixel readout chip with 55-μm square elements working in single photon counting mode. IEEE

Trans Nucl Sci. 2002;49:2279–2283.
28. Pani R, Pellegrini R, Cinti MN, et al. New devices for imaging in nuclear medicine. Cancer Biother Radiopharm. 2004;19:121–128.
29. de Vree GA, Westra AH, Moody I, van der Have F, Ligtvoet CM, Beekman FJ. Photon-counting gamma camera based on an electron-multiplying CCD. IEEE Trans Nucl Sci. In press.

Chapter 8

Design and performance of U-SPECT-II: an ultra-high resolution stationary small-animal imager

F van der Have, B Vastenhouw, A J A van der Linden, W J Branderhorst, J O Krah, and F J Beekman

Abstract

There is a strong need in biomedical science for high-resolution molecular imaging in rodents. Here we present a stationary Multiple Pinhole (MP) Single Photon Emission Computed Tomography system (U-SPECT-II) dedicated for imaging at the sub-mm (rat) and sub-half- mm (mice) resolution level. U-SPECT-II uses three large field-of-view (LFOV) gamma detectors placed in a triangular set-up to obtain high pinhole magnification factors, resulting in high image resolution. In the center of the system cylindrical pinholes (PH) of different sizes can be mounted, creating a large number of projection images on the detectors. Each collimator has a total of 75 gold or tungsten PH distributed over 5 rings. Dedicated shielding prevents overlap of projections. The detectors feature digital read-out and signal processing that produce linearity-, energy-, and uniformity-corrected list mode data. Digital inputs

enable trigger signals to be incorporated in the list mode data. The system is made user friendly with the aid of a scanning focus method and graphical user interface incorporating pre-selection of the field-of-view with the aid of webcam images of the animal. Tc-99m data (energy window of 20%) were reconstructed using an ordered subset algorithm. The reconstructed resolution was 0.35 mm and 0.45mm using the mouse collimator with 0.35 mm and 0.6 mm PH respectively and using the rat collimator with 0.8mm PH. The geometric sensitivity was 0.07% and 0.18% for the mouse collimator with 0.35 mm and 0.6 mm PH, and 0.09% for the rat collimator. U-SPECT-II allows for discrimination of molecule concentrations between adjacent volumes as small as about 0.04 micro-liters (mice) and 0.5 micro-liters (rats), which is better than existing SPECT and Positron Emission Tomography (PET) systems. Our initial in vivo brain and bone images with different dose show that U-SPECT-II can be used for novel applications in the study of dynamic biological systems and (radio) pharmaceuticals. The combination of high resolution and detection efficiency of U-SPECT-II opens up new possibilities for molecular imaging studies in rodent models at the sub-organ level.

8.1 Introduction

Biomedical research strongly benefits from quantitative in vivo techniques and the ability to perform longitudinal studies in individual animals. For example, radiolabeling of small molecules, peptides, antibodies, or probes for gene expression [1–13] have made it feasible to investigate molecular mechanisms in living tissue and to evaluate new pharmaceuticals in vivo. Employing radio-labeled molecules effectively in rodent models requires Single Photon Emission Computed Tomography (SPECT) and Positron Emission Tomography (PET) instruments that are dedicated for imaging small animals. For clinical imaging (i.e. in humans) SPECT and PET are known to have a relatively poor spatial resolution and improving the spatial resolution of SPECT and PET instruments for animal research is an ongoing challenge. Especially the increasing availability of (genetically modified) mice as models for human disease necessitates the development of instruments with a much better spatial resolution and dynamic capabilities than those until recently available.

Several small-animal SPECT and PET instruments [14–19] have been proposed. For a more beneficial resolution-sensitivity trade-off most dedicated small-animal SPECT systems employ pinhole collimation instead of the clinically used parallel hole collimation. Introductions to pinhole SPECT can be found in [20, 21] and [22].

In order to be able to do tomographic reconstruction, projections of the object must be available from a sufficient number of different angles. Most systems achieve this by rotating either the detector or the object [23–30]. Stationary small animal pinhole SPECT sys-

tems [31–35] avoid the need for rotation by using detector set-ups that cover 360 degrees and the use of many pinholes to provide a large number of angles under which the animal is observed. They have fewer moving parts and therefore are less prone to mechanical problems and instability. They also provide the advantage that one can do dynamic imaging with arbitrarily short frame lengths [33, 36, 37]. The full 360 degrees coverage in combination with many focusing micro-pinholes and a high magnification factor to maximize the information content per photon provides a very high reconstructed image resolution as will be shown in the present paper.

The goal of the present paper is to describe a dedicated and user friendly ultra- high-resolution multi-pinhole SPECT scanner (U-SPECT-II, figure 1a) suitable for dynamic imaging of small experimental animals such as rats and mice. The system is a significant improvement over its experimental prototype (U-SPECT-I) [34, 37, 38] which was based on a triple head clinical camera that had to be converted back and forth from a clinical to a high-resolution pre-clinical system. The performance of U-SPECT-II is characterized with respect to sensitivity and resolution for mouse collimators with different diameter pinholes as well as for a rat collimator, using phantom experiments. Animal scans provide further demonstration of the imaging capabilities of U-SPECT-II.

8.2 Materials and Methods

8.2.1 System description

In U-SPECT-II, different multi-pinhole collimators, together with shielding parts to prevent overlap, are easily exchangeable. The sizes of tubes (44 mm and 98 mm diameter) are optimized for imaging mouse- or rat-sized animals (figure 8.1 c and d). The design of the scanner is stationary, meaning that there is no need to move the collimator, detectors or the animal, when a specific organ that fits inside the field-of-view (FOV) is being imaged. If a larger volume of interest, up to total-body imaging, is desired then the animal bed is translated using a 3D translation stage. For most cases this can be done quickly enough to still enable a combination of multiple-position acquisition with dynamic imaging at a timescale in the order of minutes. By using large crystal surface gamma camera heads as detectors and dividing those up into non-overlapping mini gamma cameras, each focused on the FOV through a separate micro-pinhole, the design is allows to obtain a high resolution and a high sensitivity at the same time [39]. The list mode acquisition provides flexibility in processing the data afterwards, e.g. for retrospective gating, choosing time frame length and selection of energy window widths for single and multi-isotope imaging.

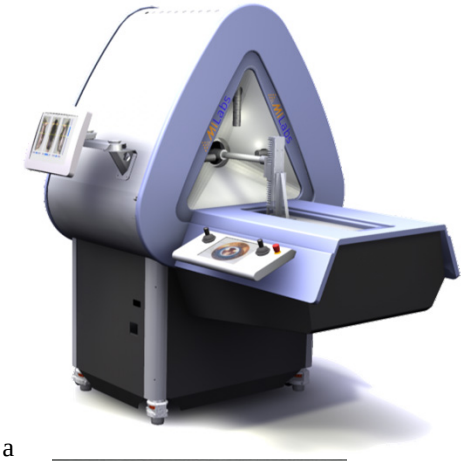

a

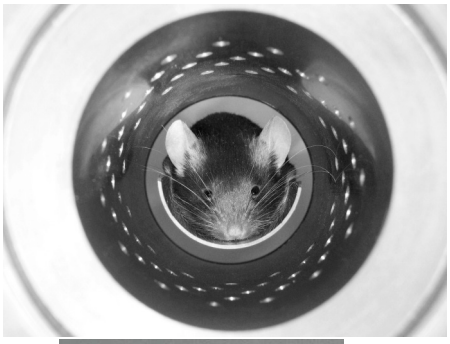

b

c

d

Figure 8.1: a) The U-SPECT-II system. b) The collimator tube surrounding a mouse. c) The mouse collimator and shielding tube. d) The rat collimator and shielding tube. The different tubes as shown in frames c) and d) can be exchanged easily from the posterior of the system. In color print in the appendix.

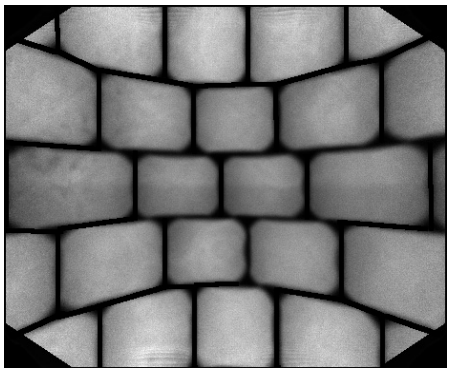

Figure 8.2: Image from an extended source, showing how one large gamma camera is divided up into mini gamma cameras. Each segment of the detector corresponds to one pinhole.

Both the rat and mouse collimator consist of a tungsten cylinder with 5 rings of 15 pinhole apertures. The pinhole positions in each ring are rotated with respect to the pinhole positions in adjacent rings in order to increase the angular sampling of the object (figure 8.1 b). All pinholes focus on a single volume (i.e. the central FOV) in the center of the tube. As shown in figure 8.1 c the mouse collimator is surrounded with tungsten shielding that prevents the projections on the detector from overlapping. In the rat collimator this shielding is implemented in a different way (figure 8.1 d) The "segmentation" of the detector in mini-gamma cameras can be visualized by placing a bottle with uniformly distributed activity that is larger than the field-of-view in the collimator tube and acquiring the projection image (figure 8.2).

The system can distinguish which collimator and bed are mounted, and restricts the motion of the translation stage to prevent collisions. The mounting mechanism of the bed to the robot is made such that the bed is locked in place and can be unlocked and transferred to another scanner, for example to a micro-CT scanner, while keeping the animal in position. This approach [40, 41] combined with a calibration phantom can be used to get registered images from independent imaging modalities without the use of fiducial markers.

Before the animal is moved into the scanner, it is placed between three optical cameras that acquire ordinary visible light images from the two sides and from the top (see figure 8.3 a). In the side views and top view, the user can select which area (volume) needs to be scanned by moving sliders (see figure 8.3 b). The system's software then calculates the sequence of positions necessary to acquire data from this volume and during the acquisition automatically moves the animal through the focus using this sequence [38]. The selection of the region of interest in the graphical user interface [42, 43] makes the system as a whole very user-friendly.

a  b 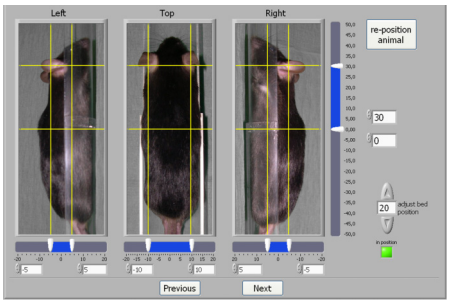

Figure 8.3: a) Mouse observed with three optical cameras for region-of-interest selection. b) User interface allows to select the volume to be scanned. In color print in the appendix.

Image reconstruction is performed with an ordered subset algorithm and a pre- calculated "system matrix" which is created in a calibration procedure that is based on measurements with a physical point source [34, 44]. Table 8.1 lists features in the U-SPECT-II system, compared to its predecessor, U-SPECT-I. One notable difference is the much larger surface area of the detectors. The other design parameters are chosen such that the peak sensitivity and resolution are approximately the same in U-SPECT-II as they were in U-SPECT-I, but the field-of-view seen in a single position is significantly larger, effectively increasing the sensitivity in multi-position scans. At the same time, the physical inner diameter of the mouse collimator has been enlarged to ensure total-body imaging of adult mice can comfortably cover the entire body. The shielding parts (in front of and to the back of the collimator) and the collimator have been made thicker than in U-SPECT-I, which is relevant mostly for imaging higher-energy isotopes.

8.2.2 The U-SPECT-II detectors

The three scintillation gamma camera heads have sodium iodide (NaI) crystals with a thickness of 3/8 inch (9.5 mm) and a useful detection area of 510 $\times$ 381 mm. Each crystal is read out by 55 photo multiplier tubes (PMTs) with the aid of digital read-out electronics. The signal of each individual PMT is digitized, and the electronics in the camera heads, together with the device driver code in the acquisition computer, apply linearity correction, energy correction, and uniformity correction. The detected events are communicated to the acquisition computer via high speed Ethernet connection and stored in list mode format, containing the horizontal and vertical position (12 bits), energy, and a time stamp for each event. The detectors are normally completely stationary when the system is in use.

Table 8.1: Comparison of U-SPECT-I to U-SPECT-II features.

Detectors	**U-SPECT-I**	**U-SPECT-II**
Crystal dimensions L × W × Th (mm)	410 × 250 × 9.5	508 × 381 × 9.5
Number of detectors	3	3
Number of PMTs per detector	49	55
PMT readout method	Analogue, resistor network	Each PMT signal digitized
Data collection	Planar pixelized image	List mode data
Pinhole collimator configuration		
Number of rings and pinholes per ring	5 × 15	5 × 15
Mouse single position FOV diameter (mm)	10.5	12
Mouse single position FOV axial (mm)	5	7
Rat single position FOV diameter (mm)	N/A	27
Rat single position FOV axial (mm)	N/A	11
Mouse collimator bore diameter (mm)	39	44
Mouse coll. radial position of pinholes (mm)	22	24
Rat collimator bore diameter (mm)	N/A	98
Rat coll. radial position of pinholes (mm)	N/A	53
Mouse pinhole material and diameters (mm)	Au, 0.3, 0.6	Au, 0.35, 0.6
Rat pinhole material and diameters (mm)	N/A	W, 0.7–1.5, Au optional
Mouse pinhole tube material	W	W
Mouse shielding tube material	Pb	W
Rat collimator tube material	N/A	W
Other shielding material	Pb	Pb
General features		
Mouse collimator 0.6 mm pinholes peak efficiency (%)	0.22	0.18
Mouse collimator 0.3(5) mm pinholes peak efficiency (%)	0.07	0.07
Rat collimator 1.0 mm pinholes peak efficiency (%)	N/A	0.09
Gating possible	no	yes
Dead time between measurements (s)	12	0.5–1
Dynamic sequence imaging	manual start	automatic
Coordination of scan sequence with acquisition	manual	automatic
GUI based navigator available	no	yes

8.2.3 Performance characterization

Sensitivity

The sensitivity of the system along the axial and trans-axial directions was measured by scanning a Tc-99m point source of known activity through the field-of-view.

Reconstructed spatial resolution

The reconstructed spatial resolution was characterized by using Derenzo phantoms consisting of configurations of differently sized capillary hot-rods, in which the center-to-center distance is twice the diameter of the rods. The phantoms contained approximately 300 MBq/ml Tc-99m. The phantoms were placed in the center of the scanner and an acquisition of 45 minutes was performed.

8.2.4 Scanning Focus Mode

In case the animal is moved through the focus during acquisition, the reconstruction algorithm needs to combine the data acquired at multiple positions of the animal with respect to the collimator tube. A method was developed to take the data from all positions into account simultaneously, rather than reconstructing each animal position separately and subsequently "stitching together" the results [45]. This method was validated experimentally in [38].

8.2.5 Initial animal experiments

Animal studies were conducted following protocols as approved by the Animal Research Committee of the University Medical Center Utrecht. To emulate either a proportionally shorter scan time or lower activity without having to scan more animals the data were reconstructed using the full scan time, and also using 33% and 10% of the counts from the list mode data. This method saves animals and allows a comparison of images of different acquisition times or doses with the animal in exactly the same position.

A mouse bone scan

A male 28 g C57Bl/6 mouse was injected intravenously with 370 MBq of Tc-99m-hydroxy methylene diphosphonate (HDP). It was anesthetized using ketamine- medetomidine-atropine (KMA) anesthesia. 2.5 hours after radioligand injection, the mouse was imaged for 1.5 hours in the U-SPECT-II system covering the entire body except for the tail followed by a scan with

the U-CT (MILabs, The Netherlands). The reconstructed U-SPECT-II and U-CT images were co-registered using PMOD software (PMOD Technologies, Zurich, Switzerland).

Mouse dopamine transporter study

A male 26 g C57BL/6 mouse was injected intraperitoneally with 40 MBq of I-123-FP- CIT (Ioflupane). It was anesthetized with KMA anesthesia. 1.5 hours after radioligand injection, it was scanned for 2 hours in the U-SPECT-II.

Rat bone scan

A 350 g male Wistar rat was injected with 900 MBq of Tc-99m hydroxy-methylene diphosphonate (HDP), and anesthetized with KMA anesthesia. Two hours after radioligand injection it was imaged for 1 hour in the U-SPECT-II scanner using the rat collimator tube with 1 mm pinholes.

8.3 Results

8.3.1 Sensitivity measurements

For Tc-99m, the sensitivity is shown in figure 8.4 for the mouse collimator with 0.6 and 0.35 mm pinholes and for the rat collimator with 1.0 mm pinholes. The z-axis is the axis parallel to the long axis of the cylinder, the x- and y-axes lie in the radial plane perpendicular to it. For the mouse collimators, the sensitivity is nearly constant within an ellipsoidal shaped area, the central field-of-view, with a diameter of around 12 mm in the x and y direction and 7 mm in the z direction (along the axis of the cylinder). For the rat collimator, this ellipsoid is approximately twice as large in the x and y direction and more than twice as large in the z direction. The sensitivities in the central field-of-view area for a Tc-99m point source are 1500 cps/MBq (0.18% geometric) for the mouse collimator with 0.6 mm pinholes, 525 cps/MBq (0.07%) for the mouse collimator with 0.35 mm pinholes, and around 700 cps/MBq (0.09%) for the rat collimator with 1.0 mm pinholes.

8.3.2 Resolution measurements

Figure 8.5 shows reconstructions of the Derenzo phantom for an indication of the spatial resolution. The smallest visually distinguishable rod sizes are 0.45 mm for the 0.6 mm pinholes mouse collimator, 0.35 mm for the 0.35 mm pinholes mouse collimator, and 0.8 mm for the 1.0 mm pinholes rat collimator.

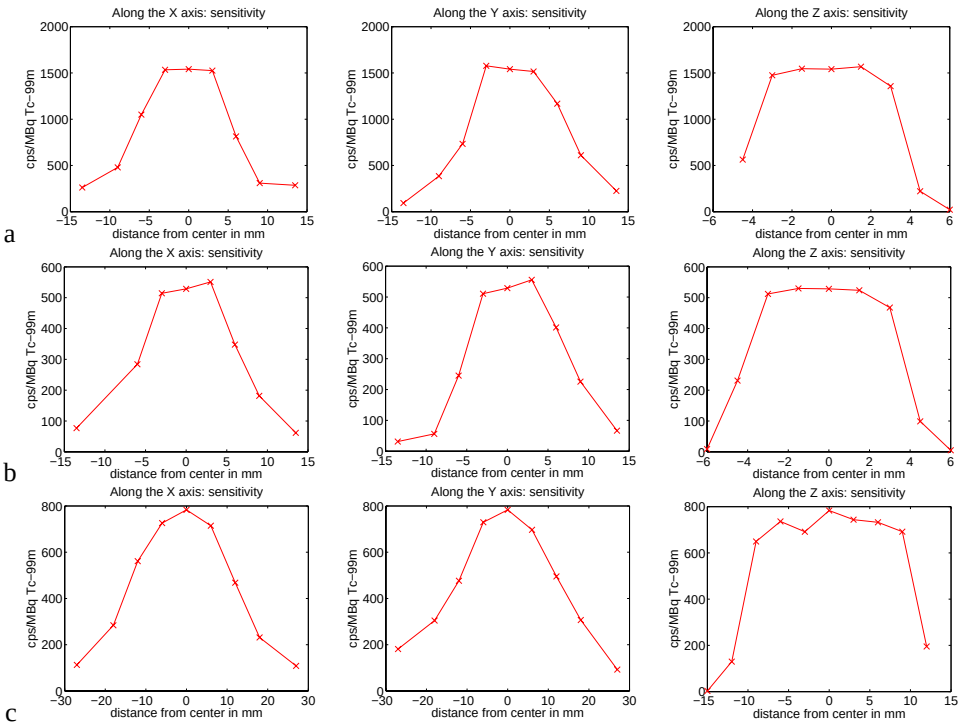

Figure 8.4: The measured sensitivity for a Tc-99m point source along the x-, y-, and z-axes of the system, expressed in cps/MBq. The z-axis is the axis of the cylindrical collimator. Note the different horizontal scales of the plots. a) the mouse collimator with 0.6 mm pinholes. b) the mouse collimator with 0.35 mm pinholes. c) the rat collimator with 1.0 mm pinholes.

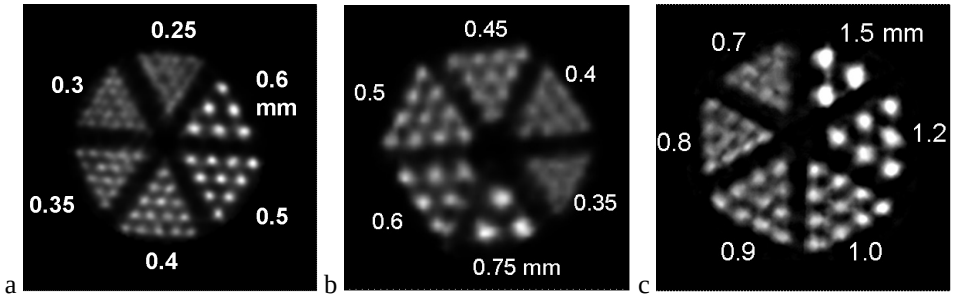

Figure 8.5: a) Reconstruction of a hot-rod Derenzo phantom showing 0.35 mm resolution, obtained using the mouse collimator with 0.35 mm pinholes. b) Reconstruction like a), showing 0.45 mm resolution, obtained using the mouse collimator with 0.6 mm pinholes. c) Reconstruction like a), showing 0.8 mm resolution, obtained using the rat collimator with 1.0 mm pinholes.

8.3.3 Initial animal experiments

Mouse bone scan

Figure 8.6 shows the results of the mouse bone scan, combining SPECT and CT. After registration, the same slice is shown for a) CT only, b) SPECT only, and c) SPECT and CT fused. The data from the SPECT scan were reconstructed using all data, one third of the data and one tenth of the data. Maximum intensity projections (MIPs) from these reconstructed volumes are shown in figure 8.7. They emulate an injected activity of 370 MBq and scan times of 90 minutes, approximately 30 minutes, and approximately 9 minutes. The 3D Gaussian blurring applied to the reconstructed data was increased for lower dose to deal with increasing noise: the FWHMs used were of 0.28, 0.41 and 0.61 mm respectively.

Mouse dopamine transporter study

Figure 8.8 shows coronal and horizontal slices of the dopamine transporter distribution in the brain of a mouse. Dopamine transporter is present in the striatum, but also in the retina and the harder glands. Parts of the eyes are therefore visible as spherical shells in the horizontal slice (figure 8.8, right). The left and right striatum are clearly separated.

Rat bone scan

The rat study with the bone tracer HDP was reconstructed using all recorded photons, one third of the photons, and one tenth of the photons. This emulates a scan time of one hour

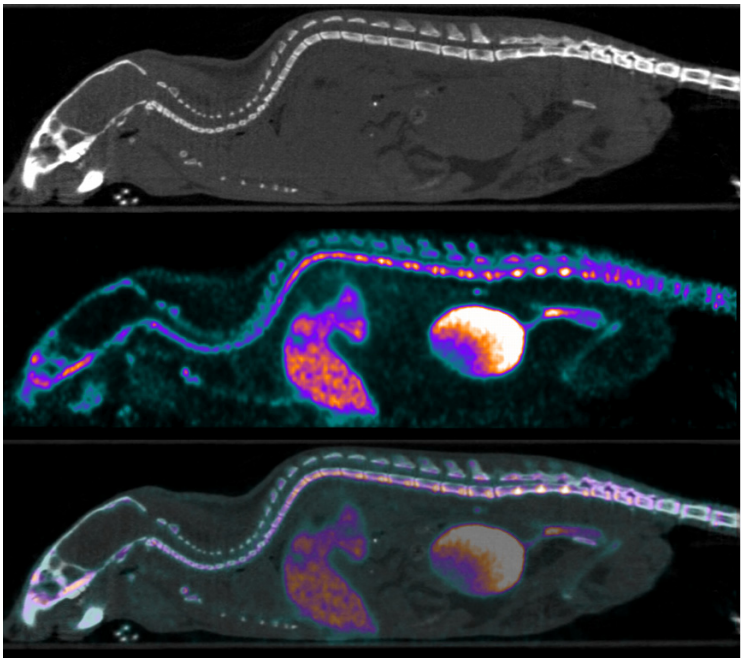

Figure 8.6: SPECT-CT saggital slice of a mouse. Top: CT only, middle: SPECT only, bottom: SPECT-CT fused. SPECT was a ^{99m}Tc-HDP bone scan on the U-SPECT-II system. Registration was done by the method of Chow et al [40]. In color print in the appendix.

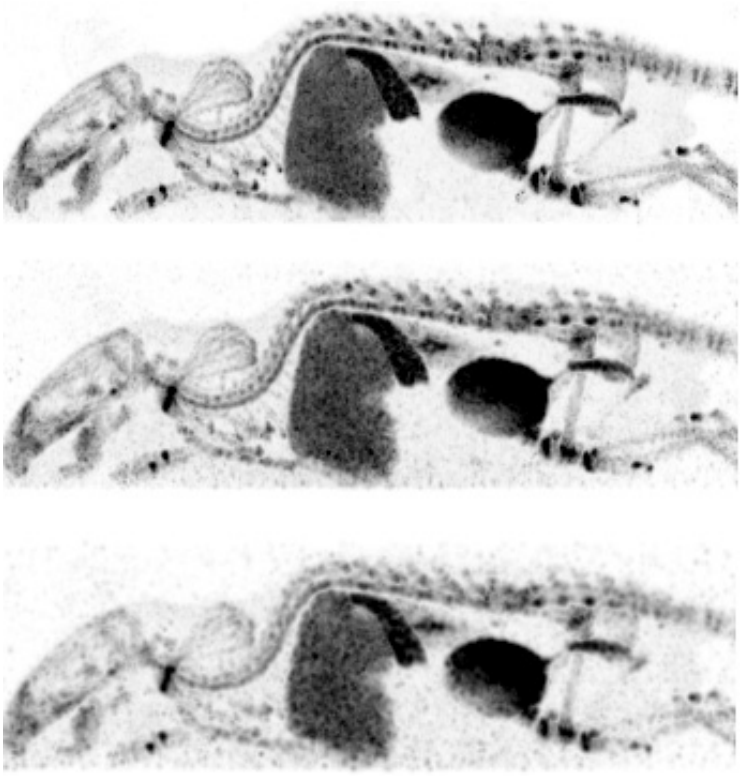

Figure 8.7: Maximum Intensity Projections (MIPs) of the SPECT data from the same mouse bone study as in figure 8.6. The top image is based on all, the middle image on one third, and the bottom image on one tenth of the available data.

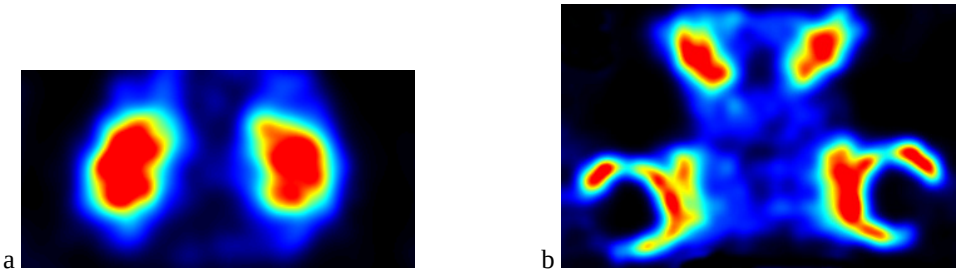

Figure 8.8: Mouse dopamine transporter study showing a coronal slice (a) through the striatum and a horizontal slice (b) through the striatum and eyes. In color print in the appendix.

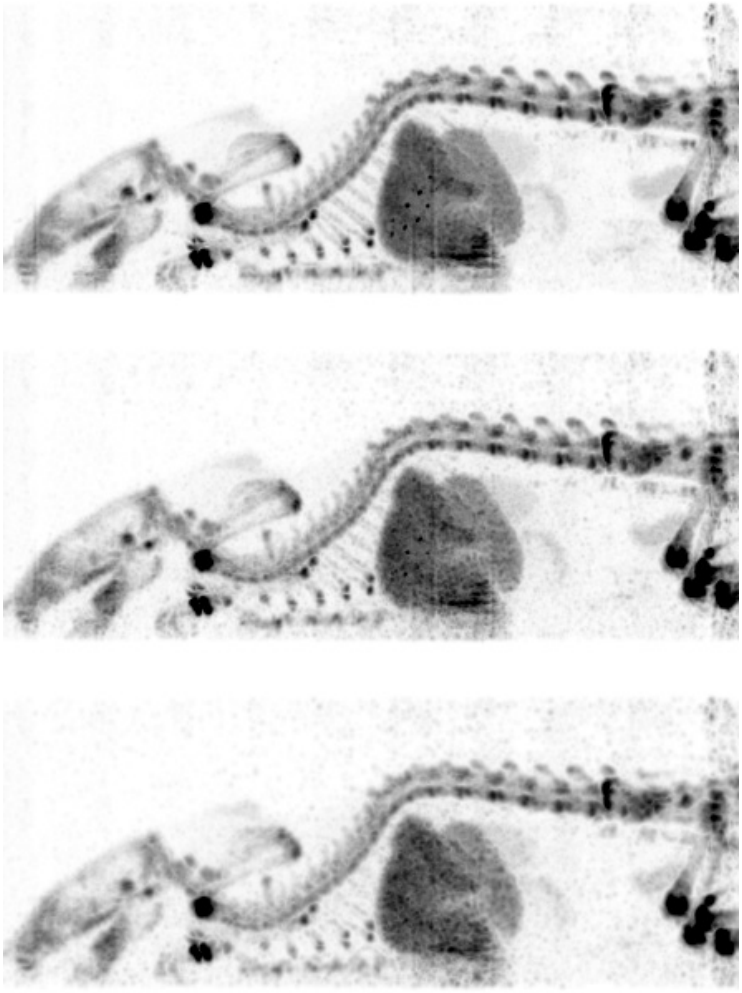

Figure 8.9: Maximum Intensity Projection (MIP) image of a ^{99m}Tc-hydroxy-methylene diphosphonate study in a rat. The reconstruction was done using all of (top image), one third of (middle image), and one tenth of (bottom image) the counts from the list mode data.

with 900 MBq, 300 MBq and 90 MBq injected activity (resp.) or alternatively, acquisition times of one hour, approximately 20 minutes and approximately 6 minutes. Figure 8.9 shows maximum intensity projections (MIPs) of those three reconstructions. The system sensitivity of the 1.0 mm rat collimator tube lies in between the sensitivities of the 0.6 and 0.35 mm mouse collimators. The size of the tube has been designed to be more than twice as large as the mouse collimator at the cost of resolution. The net result is that relative to the animal's size, approximately the same level of anatomical detail seems to be visible in the mouse (figure 8.7) as in the rat.

8.4 Discussion

We built a versatile SPECT system with an advanced user interface that can be used for conducting molecular imaging in both mice and rats. Its resolution is unmatched by any existing SPECT or PET system. With the focusing design currently applied U-SPECT-II, it is possible to perform focused imaging, only studying a single organ of interest, as well as imaging larger volumes up to total-body imaging, with a single collimator tube. We expect that it is possible to improve significantly on the performance in specific cases with collimator tubes dedicate to specific tasks. For example, a dedicated collimator for extremities could have a much smaller diameter and the same amount of pinholes. The resulting increase of sensitivity and magnification factor may improve the resolution to about 0.1 mm for legs and possibly to 0.25 mm for the mouse brain. However the first improvements may be possible by simply optimizing the pinhole diameters for different types of studies.

The algorithm that calculates the scan sequence from the boundaries drawn by the user is currently fairly straight forward. There is ongoing research to optimize the scan sequence by means of experiments and advanced simulation studies. This may lead to improvements in either image quality or reconstruction time for U-SPECT-II in the future using the same hardware.

Today, the advantages and disadvantages of using overlapping versus non- overlapping projections is actively being researched at several labs worldwide. Overlap increases system sensitivity but one has too keep in mind that this increase is at least partly artificial, since a significant amount of information per photon can be lost due to the overlap. Therefore, sensitivity of systems based on overlapping projections can not be compared to systems with non-overlapping projections. Moreover, overlap can lead to increasing reconstruction time due to slow convergence of iterative algorithms for these cases, and completely misplace the activity in the reconstruction when activity is present outside the area that is sufficiently sampled.

Projected future versions of U-SPECT may be based on detectors with a higher intrinsic resolution [22]. Higher resolution detectors suitable for gamma imaging are being developed [46–48]. Detectors with a very high intrinsic resolution are currently still too much in a prototype stage or too expensive, despite the fact that a much smaller detector ring can be used [39, 49].

8.5 Conclusions

The introduction of U-SPECT defines a new front line in ultra-high resolution small- animal radio-molecular imaging. U-SPECT-II is flexible and user friendly with regard to selection of optimal collimators and field-of-view for different animals and imaging tasks. An outstanding volumetric resolution of 0.04 μl has been obtained with the highest resolution collimators tested in here. Results show that U-SPECT-II provides a significant resolution improvement over current state-of-the-art small-animal SPECT and PET systems. As a result, the system allows for assessing tracer dynamics in sub- compartments of organs, as was illustrated by in vivo images with sub-mm details of tracer uptake in rodent brains and bone.

The high resolution and high sensitivity together with exchangeable collimator tube, animal bed and a user-friendly web-cam based interface should now allow detailed molecular imaging to be applied successfully to a wide range of study types, thus creating a broad range of new experimental opportunities. Significant improvements in the image quality of U-SPECT-II can be expected when collimation parameters are optimized for specific tasks. It is expected that high-resolution gamma detectors and dedicated collimators will play an important role in the future improvement of SPECT instruments.

Acknowledgements

This work was sponsored by the Netherlands Organization for Scientific Research (NWO), grant 917.36.335. We thank Norbert Gehéniau, Bert Westra, Henk te Biesebeek and Kees Ligtvoet for instrumental support, the staff at Inter Medical Medizintechnik and Gijs van der Wilt for technical assistance, Carmen van Vilsteren, Paul Hermans for fruitful discussions, Mart Rentmeester for registration of the SPECT and CT images, and Jan Heemskerk for proof-reading the manuscript.

Bibliography

[1] S. S. Gambhir, J. R. Barrio, L. Wu, M. Iyer, M. Namavari, N. Satyamurthy E. Bauer, C. Parrish, D. C. MacLaren, A. R. Borghei, L. A. Green, S. Sharfstein, A. J. Berk, S. R. Cherry, M. E. Phelps, and H. R. Herschman. Imaging of adenoviral-directed herpes simplex virus type 1 thymidine kinase reporter gene expression in mice with radiolabeled ganciclovir. *J. Nucl. Med.*, 39:2003–2011, 1998.

[2] A. Bogdanov Jr. and R. Weissleder. The development of in vivo imaging systems to study gene expression. *Trends in Biotechnology*, 16:5–10, 1998.

[3] R. F. Service. New probes open windows on gene expression, and more. *Science*, 280:1010–1011, 1998.

[4] S. S. Gambhir, H. R. Herschman, S. R. Cherry, J. R. Barrio, N. Satyamurthy, T. Toyukuni, M. E. Phelps, S. M. Larson, J. Balatoni, R. Finn, M Sadelain, J. Tjuvajev, and R. Blasberg. Imaging transgene expression with radionuclide imaging technologies. *Nature Neoplasia*, 2(1):118–138, 2000.

[5] M. E. Phelps. Inaugural article: positron emission tomography provides molecular imaging of biological processes. *Proc. Natl. Acad. Sci. USA*, 97:6226–6233, 2000.

[6] H. R. Herschman, D. C. MacLaren, M. Iyer, M. Namavari, K. Bobinski, L. A. Green, L. Wu, A. J. Berk, T. Toyokuni, J. R. Barrio, S. R. Cherry, M. E. Phelps, E. P. Sandgren, and S. S. Gambhir. Seeing is believing: Non-invasive, quantitative and repetitive imaging of reporter gene expression in living animals, using positron emission tomography. *J. Neuroscience research*, 59:699–705, 2000.

[7] A. Jacobs, J. Voges, R. Reszka, M. Lercher, A. Gossmann, L. Kracht, C. Kaestle, R. Wagner, K. Wienhard, and W. Heiss. Positron-emission tomography of vector-mediated gene expression in gene therapy for gliomas. *The Lancet*, 358:727–729, 2001.

[8] R. Weissleder. Scaling down imaging: molecular mapping of cancer in mice. *Nat. Rev. Cancer*, 2(1):11–18, Jan. 2002.

[9] R. Blasberg. PET imaging of gene expression. *Eur. J. Canc.*, 38:2137–2146, 2002.

[10] M. Rudin and R. Weissleder. Molecular imaging in drug discovery and development. *Nat. Rev. Drug Discov.*, 2(2):123–31, Feb. 2003.

[11] K. Shah, A. Jacobs, X. O. Breakefield, and R. Weissleder. Molecular imaging of gene therapy for cancer. *Gene Ther.*, 11(15):1175–1187, Aug. 2004.

[12] J. C. Wu, F. M. Bengel, and S. S. Gambhir. Cardiovascular molecular imaging. *Radiology*, 244:337–355, 2007.

[13] M. A. Rueger, L. W. Kracht, R. Hilker, A. Thiel, J. Sobesky, A. Winkeler, A. V. Thomas, M. T. Heneka, R. Graf, K. Herholz, W. D. Heiss, and A. H. Jacobs. Role of in vivo imaging of the central nervous system for developing novel drugs. *Q. J. Nucl. Med. Mol. Imaging*, 51:164–181, 2007.

[14] S. R. Cherry, Y. Shao, R. W. Silverman, K. Meadors, S. Siegel, A. F. Chatziioannou, J. W. Young, W. F. Jones, J. C. Moyers, D. Newport, A. Boutefnouchet, T. H. Farquhar, M. Andreaco, M. J. Paulus, D. M. Binkley, R. Nutt, and M. E. Phelps. MicroPET: A high resolution PET scanner for imaging small animals. *IEEE Trans. Nucl. Sci.*, 44:1161–1166, 1997.

[15] A. F. Chatziioannou, S. R. Cherry, Y. P. Shao, R. W. Silverman, K. Meadors, T. H. Farquhar, M. Pedarsani, and M. E. Phelps. Performance evaluation of microPET: A high-resolution lutetium oxyorthosilicate pet scanner for animal imaging. *J. Nucl. Med.*, 40:1164–1175, 1999.

[16] A. P. Jeavons, R. A. Chandler, and C. A. R. Dettmar. A 3D HIDAC-PET camera with sub-millimetre resolution for imaging small animals. *IEEE Trans. Nucl. Sci.*, 46:468–473, 1999.

[17] A. F. Chatziioannou. Molecular imaging of small animals with dedicated PET tomographs. *Eur. J. Nucl. Med. Mol. Imaging*, 29:98–114, 2002.

[18] Y. C. Tai, A. F. Chatziioannou, Y. Yang, R. W. Silverman, K. Meadors, S. Siegel, D. F. Newport, J. R. Stickel, and S. R. Cherry. MicroPET II: design, development and initial performance of an improved microPET scanner for small-animal imaging. *Phys. Med. Biol.*, 48(11):1519–1537, June 2003.

[19] Y. Yang, Y. C. Tai, S. Siegel, D. F. Newport, B. Bai, Q. Li, R. M. Leahy, and S. R. Cherry. Optimization and performance evaluation of the microPET II scanner for in vivo small-animal imaging. *Phys. Med. Biol.*, 49(12):2527–2545, June 2004.

[20] M. A. King, P. H. Pretorius, T. Farncombe, and F. J. Beekman. Introduction to the physics of molecular imaging with radioactive tracers in small animals. *J. Cell. Biochem.*, Suppl. 39:221–230, 2002.

[21] S. R. Meikle, P. Kench, M. Kassiou, and R. B. Banati. Small animal SPECT and its place in the matrix of molecular imaging technologies. *Phys. Med. Biol.*, 50(22):R45 – R61, 2005.

[22] F. J. Beekman and F. van der Have. The pinhole: gateway to ultra-high resolution three-dimensional radionuclide imaging. *Eur. J. Nucl. Med. Mol. Imaging*, 34:151–161, 2007.

[23] R. J. Jaszczak, J. Li, H. Wang, M. R. Zalutsky, and R. E. Coleman. Pinhole collimation for ultra-high-resolution small-field-of-view SPECT. *Phys.Med.Biol.*, 39:425–37, 1994.

[24] K. Ishizu, T. Mukai, Y. Yonekura, M. Pagani, T. Fujita, N. Tamaki, H. Shibasaki, and J. Konishi. Ultra-high-resolution SPECT system using four pinhole collimators for small animal studies. *J. Nucl. Med.*, 26:2282–2289, 1995.

[25] D. P. McElroy, L. R. MacDonald, F. J. Beekman, Y. Wang, B. E. Patt, J. S. Iwanczyk, B. M. W. Tsui, and E. J. Hoffman. Performance evaluation of A-SPECT: A high resolution desktop pinhole SPECT system for imaging small animals. *IEEE Trans. Nucl. Sci.*, 49:2139–2147, 2002.

[26] N. U. Schramm, G. Ebel, U. Engeland, T. Schurrat, M. Béhé, and T. M. Behr. High-resolution SPECT using multipinhole collimation. *IEEE Trans. Nucl. Sci.*, 50(3):315–320, June 2003.

[27] S. Walrand, F. Jamar, M. de Jong, and S. Pauwels. Evaluation of novel whole-body high-resolution rodent SPECT (linoview) based on direct acquisition of linogram projections. *J. Nucl. Med.*, 46:1872–1880, 2005.

[28] S. D. Metzler, R. J. Jaszczak, N. H. Patil, S. Vemulapalli, G. Akabani, and B. B. Chin. Molecular imaging of small animals with a triple-head SPECT system using pinhole collimation. *IEEE Trans. Med. Im.*, 24(7):853–862, July 2005.

[29] S. C. Moore, R. E. Zimmerman, A. Mahmood, R. Mellen, and C. B. Lim. A triple-detector multi-pinhole system for SPECT imaging of rodents. *J. Nucl. Med.*, 45:97P, 2005.

[30] J. Y. Hesterman, M. A. Kupinski, L. R. Furenlid, D. W. Wilson, and H. H. Barrett. The multi-module, multi-resolution system (M^3R): A novel small-animal SPECT system. *Med. Phys.*, 34:987–993, 2007.

[31] G. K. Kastis, H. B. Barber, H. H. Barrett, H. C. Gifford, I. W. Pang, D. D. Patton, G. Stevenson, and D. W. Wilson. High resolution SPECT imager for three-dimensional imaging of small animals (abstract). *J. Nucl. Med.*, 39:9P, 1998.

[32] Z. Liu, G. A. Kastis, G. D. Stevenson, H. H. Barrett, L. R. Furenlid, M. A. Kupinski, D. D. Patton, and D. W. Wilson. Quantitative analysis of acute myocardial infarct in rat hearts with ischemia-reperfusion using a high-resolution stationary SPECT system. *J. Nucl. Med.*, 43(7):933–939, 2002.

[33] L. R. Furenlid, D. W. Wilson, Y. C. Chen, H. Kim, P. J. Pietraski, M. J. Crawford, and H. H. Barrett. FastSPECT II: A second-generation high-resolution dynamic SPECT imager. *IEEE Trans. Nucl. Sci.*, 51(3):631–635, June 2004.

[34] F. J. Beekman, F. van der Have, B. Vastenhouw, A. J. A. van der Linden, P. P. van Rijk, J. P. H. Burbach, and M. P. Smidt. U-SPECT-I: A novel system for sub-millimeter resolution tomography of radiolabeled molecules in mice. *J. Nucl. Med.*, 46:1194–1200, 2005.

[35] T. Funk, P. Després, W. C. Barber, K. S. Shah, and B. H. Hasegawa. A multipinhole small animal SPECT system with submillimeter spatial resolution. *Med. Phys.*, 33:1259–1267, 2006.

[36] M. A. Kupinski and editors H. H. Barrett. *Small-Animal SPECT imaging*. Springer, New York, Science+Business Media Inc., 2005.

[37] B. Vastenhouw B, F. van der Have, A. J. A. van der Linden, L. von Oerthel, J. Booij, J. P. H. Burbach, M. P. Smidt, and F. J. Beekman. Movies of dopamine transporter occupancy with ultra-high resolution focusing pinhole SPECT. *Mol. Psych.*, page (accepted), 2007.

[38] B. Vastenhouw and F. J. Beekman. Sub-mm total-body murine imaging with U-SPECT-I. *J. Nucl. Med.*, pages 487–493, 2007.

[39] M. C. M. Rentmeester, F. van der Have, and F. J. Beekman. Optimizing multi-pinhole SPECT geometries using an analytical model. *Phys. Med. Biol.*, 52:2567–2581, 2007.

[40] P. L. Chow, D. B. Stout, E. Komisopoulou, and A. F. Chatziioannou. A method of image registration for small animal, multi-modality imaging. *Phys. Med. Biol.*, 51:379–390, 2006.

[41] F. J. Beekman and B. F. Hutton. Multi-modality imaging on track. *Eur. J. Nucl. Med. Mol. Imaging*, page (in press), 2007.

[42] F. J. Beekman. Stralingsdetectieinrichting. *Dutch patent application, NL-1030168—Oktober 2005*, 2005.

[43] F. J. Beekman. Radiation detection device, scintillation device and detection method, as well as multiple image-forming device. *PCT application PCT/NL2006/000513, October 2006*, 2006.

[44] F. van der Have, B. Vastenhouw, M. C. M. Rentmeester, and F. J. Beekman. System calibration and statistical image reconstruction for sub-mm stationary pinhole SPECT. *Conference Record of the 2005 Nuclear Science Symposium and Medical Imaging Conference, Puerto Rico*, pages M11–291, 2005.

[45] F. J. Beekman, B. Vastenhouw, and F. van der Have. Towards 3D nuclear microscopy using locally focusing many-pinhole SPECT. *Proceedings of the 2003 International Meeting on Fully Three-Dimensional Image Reconstruction in Radiology and Nuclear Medicine, Saint-Malo, France*, 2004.

[46] G. A. de Vree, A. H. Westra, I. Moody, F. van der Have, C. M. Ligtvoet, and F. J. Beekman. Photon-counting gamma camera based on an electron-multiplying CCD. *IEEE Trans. Nucl. Sci.*, 52(3):580 – 588, June 2005.

[47] L. J. Meng, N. H. Clinthorne, S. Skinner, R. V. Hay, and M. Gross. Design and feasibility study of a single photon emission microscope system for small animal i-125 imaging. *IEEE Trans. Nucl. Sci.*, 53:1168–1178, 2006.

[48] J. W. T. Heemskerk, A. H. Westra, P. M. Linotte, C. M. Ligtvoet, W. Zbijewski, and F. J. Beekman. Front-illuminated versus back-illuminated photon-counting CCD-based gamma camera: important consequences for spatial resolution and energy resolution. *Phys. Med. Biol.*, 52:N149–N162, 2007.

[49] F. J. Beekman and B. Vastenhouw. Design and simulation of a high-resolution stationary SPECT system for small animals. *Phys. Med. Biol.*, 49:4579–4592, 2004.

Chapter 9

Summary

The main subject of this thesis is the development of the first two in a series of dedicated ultra-high-resolution Single Photon Emission Computed Tomography (SPECT) systems (U-SPECT-I and II) for the imaging of distributions of radio-isotope labeled tracers in small laboratory animals such as mice and rats.

One key technique that helps to obtain high resolution SPECT images is the use of pinholes, which were also applied in early optical cameras. **Chapter 2** provides a brief history of pinhole imaging and explains the basics of pinhole radionuclide imaging. It also introduces modern image reconstruction methods required for obtaining tomographic images from pinhole projections, including the statistical algorithms used in U-SPECT. The recent developments in high-resolution small-animal SPECT instruments are discussed, as well as ways to improve their performance, such as the use of higher resolution detectors. Chapter 2 additionally presents a possible design for a clinical cardiac SPECT scanner based on focusing pinhole gamma cameras. Calculations demonstrate that it would be possible to image the human heart an order of magnitude faster, or with much more detail than is possible with parallel-hole collimation which is currently used in clinical SPECT.

The image quality in SPECT is degraded by the effects of penetration (gamma photons that pass through the collimator material instead of being stopped) and collimator scatter (gamma photons that have an interaction with the collimator material and suffer from change of direction or energy). Both these effects add uncertainty to the apparent direction from which detected photons originated, and therefore negatively influence the quality of the resulting images. The first designs for the U-SPECT system assumed smaller pinhole diameters than had been used in any multi-pinhole system before, and it was unknown at the time to what extent penetration and scatter effects would affect the projection images. By means of

Monte Carlo computer simulations, **chapter 3** characterizes the effects of penetration and scatter when using micro-pinholes made in lead, tungsten, gold and platinum. The simulations were carried out for two isotopes which are used for labeling of SPECT tracers: I-125 (27–35 keV) and Tc-99m (140 keV). The pinhole diameters that were investigated range from 0.05 to 0.5 mm. The conclusions of the work presented in chapter 3 are that for the case of a Tc-99m point source and gold or platinum pinholes with the smallest diameter used in U-SPECT-I and II (0.3 mm), 55% of the photons detected resulted from penetration and approximately 3% from scatter. Furthermore, the use of tungsten or lead pinholes results in a scatter fraction up to 1.8 times higher than the more expensive materials like gold and platinum. Finally, the amount of penetrated and scattered photons varied approximately linearly with respect to the pinhole diameter. If these results are viewed with respect to the U-SPECT system in particular, scatter does not appear to be a major issue. Collimator penetration is modeled and accounted for during reconstruction, and collimator scatter can be neglected if it amounts to only a few percent of the detected photons. **Chapter 4** is an extension of the work in chapter 3. An additional isotope with high-energy contributions (I-123) is investigated and the focus is shifted to the shape of the pinhole. The effect of a channel shape versus a knife-edge shape is studied, as well as the effect of the pinhole opening angle. At perpendicular incidence, a channel pinhole shape reduces the penetration and scatter fractions. However, this advantage disappears at higher angles of incidence. A significant drawback of channel pinholes is that they have a substantially lower total sensitivity (the fraction of emitted photons that can be detected) than knife-edge pinholes and for reproducibly detecting contrast they are also less suitable. The results in chapter 4 further indicate that the opening angle of a pinhole plays a more important role in reducing penetration and scatter than whether or not the pinhole has a channel or knife-edge shape. For the U-SPECT project, channel pinholes seem to offer little advantages.

An important part of the design of a small-animal SPECT system is the imaging geometry: how many pinholes will be used, and what is their placement with respect to the animal and the detector? It is not straightforward to create an “optimal” system, since there are many parameters which need to be considered and most, if not all, are interrelated. Performing ray-tracing or even Monte Carlo simulations of complete systems to optimize performance may become too time-consuming because of the large number of trials required. **Chapter** 5 presents a mathematical model which can be used to quickly compare the projected performance in terms of resolution or sensitivity of systems with varying design parameters. The model assumes that the multi-pinhole collimator and the detector both have the shape of a spherical layer, and uses analytical expressions for effective pinhole diameters, sensitivity, and spatial resolution. For a fixed field-of-view size, the pinhole diameter is adjusted in order

to compare the system resolution of different systems at equal system sensitivity and vice versa. The model predicts that for optimal resolution or sensitivity the collimator layer with pinholes should be placed as closely as possible around the animal given a fixed detector layer. When high-resolution detectors become available, a resolution improvement of 30% would be achievable for an optimized system with a geometry similar to that of U-SPECT-I. High-resolution detectors can be placed close to the collimator without significant system resolution loss. In combination with high-resolution detectors, systems with a physical pinhole diameter of 0 mm, where all photons detected must penetrate the pinholes' edge material, can have an excellent resolution.

For multi-pinhole SPECT, iterative reconstruction algorithms are preferred over analytical methods. Iterative algorithms require knowledge of the position-dependent point spread functions (PSFs, also known collectively as "the system matrix") which specify the response of the detectors to a point source at every position in the instrument. The more accurately the PSF tables describe the real system, the better the reconstructed images will reflect the true distribution of radioactivity. Obtaining these PSF tables purely by measurement with a physical point source would be ideal in the sense that the resulting PSFs would best describe reality, but it is unfeasible to do for high-resolution instruments because of the prohibitively large number of measurement positions. **Chapter** 6 presents the calibration method that was developed to obtain the complete PSF tables for the U-SPECT systems. This method is based on generalization over the entire object space, of some defining properties of point source responses obtained at a limited number of measurement positions. The full shape of measured point source responses can almost be preserved in the created PSF tables created by the method. It is shown that the generated PSF tables can be used to obtain high-resolution SPECT reconstructions on the U-SPECT-I system: the reconstructed resolutions judged by rod visibility in a micro capillary phantom are 0.45 mm with 0.6 mm pinholes and below 0.35 mm with 0.3 mm pinholes. Chapter 6 also shows that approximations, such as truncating the PSF kernel at different diameters, result in significant reduction of reconstruction time while maintaining acceptable reconstructions. Reconstructions of capillary phantoms based on different acquisition times allow us to conclude that the spatial resolution of the U-SPECT-I system remains below 1 mm even if very short acquisition times (in the order of a minute) are used.

The first prototype small-animal SPECT system built in Utrecht is called U-SPECT-I, described in **chapter 7**. This stationary system is capable of acquiring the necessary projection data for tomographic imaging of mouse organs, without the need for mechanical movement of the detectors or collimator. The performance of U-SPECT-I in terms of achievable resolution and sensitivity is characterized and examples of measurements with mice are presented.

With 0.6 mm diameter pinholes, the maximum fraction of detected photons emitted by a point source (peak sensitivity) is 0.22% and remains above 0.12% in the central 12 mm of the central plane. The reconstructed resolution, judged by rod visibility in a micro capillary phantom, is < 0.5 mm. Images of a mouse spine show uptake of Tc-99m-hydroxy-methylene diphosphonate (HDP) down to the level of tiny parts of vertebral processes. These are clearly separated from the vertebral and inter-vertebral foramina. Using another tracer, myocardial perfusion in the left and right ventricular wall, and even in structures as small as the papillary muscles, can be monitored. U-SPECT-I allows discrimination of molecule concentrations between adjacent volumes as small as about 0.1 micro-liter, significantly smaller than any previous SPECT or PET system.

A next generation system called U-SPECT-II, is described in **chapter 8**. U-SPECT-II can be used for imaging of both mice and rats. It has a significantly larger detector surface than U-SPECT-I and its detectors have fully digital electronics. The data is read out in list mode, which provides flexibility in choosing energy windows and performing multi-isotope imaging, and allows to perform gated imaging. Furthermore it has an automated method to expand the field-of-view up to the scale of total body imaging using a specially designed graphical user interface. Chapter 8 describes the design, development, and initial measurements to characterize the performance. It also demonstrates some of its capabilities in imaging animals. The reconstructed resolution (judged by rod visibility in a micro capillary phantom) is 0.35 mm using the mouse collimator with 0.35 mm pinholes, 0.45 mm using the mouse collimator with 0.6 mm pinholes, and 0.8 mm using the rat collimator with 1.0 mm pinholes. The geometric sensitivity is 0.07% for the mouse collimator with 0.35 mm pinholes, 0.18% for the mouse collimator with 0.6 mm pinholes, and 0.09% for the rat collimator with 1.0 mm pinholes. U-SPECT-II allows discrimination of molecule concentrations between adjacent volumes as small as about 0.04 micro-liter (mice) and 0.5 micro-liter (rats). Our initial *in vivo* brain and bone images obtained with different injected activities of the tracer show that U-SPECT-II can be used for novel applications in the study of dynamic biological systems and (radio) pharmaceuticals. Its user-friendly graphical user interface and new imaging capabilities make it a versatile system for conducting molecular imaging studies.

Samenvatting

Het onderwerp van dit proefschrift is de ontwikkeling van een serie *Single Photon Emission Computed Tomography* (SPECT) systemen (U-SPECT-I en -II) met een ultra-hoge resolutie die zijn toegesneden op het afbeelden van de ruimtelijke verdeling van met radionucliden (radioactieve stof) *gelabelde tracer* moleculen in kleine proefdieren zoals muizen en ratten.

Pinholes, zoals die in de vroege fotografie ook gebruikt werden (*camera obscura*), leveren een belangrijke bijdrage aan het verkrijgen van SPECT beelden met een hoge resolutie. In **hoofdstuk 2** worden de geschiedenis van het maken van afbeeldingen met behulp van pinholes en de grondbeginselen van het afbeelden van radionucliden met pinholes uiteengezet. In het hoofdstuk worden ook de moderne beeldreconstructiemethoden beschreven die nodig zijn voor het verkrijgen van *tomografische beelden* (een serie 2D plakken die samen een 3D beeld vormen) uit de projectiebeelden die door de pinholes worden gevormd. Ook worden er de statistische algoritmen behandeld die in U-SPECT gebruikt worden. Het hoofdstuk bevat verder een bespreking van de recente ontwikkelingen in hoge-resolutie SPECT instrumenten voor kleine dieren, met de mogelijkheden om hun prestaties te verbeteren, zoals het gebruik van detectoren met een hogere resolutie. In het laatste deel van hoofdstuk 2 wordt een mogelijk ontwerp voor een klinische SPECT-scanner voor het hart gepresenteerd die gebaseerd is op gefocusseerde pinhole-gammacamera's. Een berekening laat zien dat het mogelijk is om een opname van het menselijk hart ofwel een factor tien sneller te kunnen maken, ofwel om veel meer detail zichtbaar te maken dan mogelijk is met de nu vaak gebruikte techniek, *parallel hole* SPECT.

Randpenetratie (gamma fotonen die door de collimator gaan in plaats van gestopt te worden) en verstrooiing (gamma fotonen die een interactie hebben met het collimatormateriaal en daarbij van richting veranderen of een andere energie krijgen) hebben een negatieve invloed op de beeldkwaliteit in SPECT. Dit komt, omdat deze twee effecten zorgen voor extra onzekerheid over de richting waar de gedetecteerde fotonen vandaan komen. De eerste versies van het ontwerp van het U-SPECT systeem gingen uit van pinholes met een kleinere

diameter dan er tot dan toe was gebruikt in enig multi-pinhole systeem en het was in die fase niet bekend in welke mate randpenetratie en collimatorverstrooiing de projectiebeelden zouden beïnvloeden. Door middel van *Monte Carlo*-computersimulaties worden in **hoofdstuk 3** de effecten van randpenetratie en verstrooiing in kaart gebracht voor micro-pinholes gemaakt van lood, wolfraam, goud en platina. Deze simulaties zijn gedaan voor twee isotopen die relevant zijn voor SPECT bij dieren: I-125 (27–35 keV) en Tc-99m (140 keV). De pinholediameter variëert daarbij van 0,05 tot 0,5 mm. De conclusie voor het geval van een Tc-99m puntbron en gouden of platina pinholes met de kleinste diameter die in U-SPECT-I en -II gebruikt wordt (0,3 mm), is dat 55% van de gedetecteerde fotonen door de pinholerand komen en ongeveer 3% is verstrooid. Wolfraam of loden pinholes hebben een verstrooiingspercentage tot 1,8 maal zo hoog als goud of platina. Tenslotte wordt geconcludeerd dat het aantal fotonen dat door de rand gaat en het aantal dat verstrooid wordt, bij benadering lineair afhangt van de pinholediameter. Wanneer deze conclusies worden bezien in het licht van het U-SPECT systeem, is vooral belangrijk dat verstrooiing geen grote rol van betekenis speelt. Tijdens de reconstructie wordt voor randpenetratie gecorrigeerd door deze te modelleren. Verstrooiing in de pinhole collimator kan worden verwaarloosd als het verantwoordelijk is voor niet meer dan een paar procent van de gedetecteerde fotonen. **Hoofdstuk 4** is een uitbreiding van hoofdstuk 3. Er wordt een extra isotoop onderzocht dat ook fotonen met een hoge energie uitzendt (I-123) en het zwaartepunt komt te liggen bij de vorm van de pinhole. Het effect van een kanaaltje (buisvormig stukje) in het hart van de pinhole versus een pinhole met een scherpe rand wordt onderzocht, net als het effect van pinholes met verschillende openingshoeken. Een pinhole met een kanaaltje in plaats van een scherpe rand, zorgt in het geval van loodrechte inval van de straling voor lagere fracties van fotonen die door de rand komen en die verstrooid worden. Dit voordeel verdwijnt echter bij hogere invalshoeken. Een nadeel van pinholes met een kanaaltje is dat ze een aanzienlijk lagere totale gevoeligheid (het deel van de uitgezonden fotonen dat gedetecteerd kan worden) hebben dan pinholes met een scherpe rand en dat ze slechter presteren als het gaat om het reproduceerbaar meten van een contrast. De resultaten in hoofdstuk 4 geven verder aan dat de openingshoek van de pinhole belangrijker is voor het terugdringen van randpenetratie en verstrooiing dan de invloed van een keuze tussen pinholes met een kanaaltje en met een scherpe rand. Voor het U-SPECT-project lijken pinholes met een kanaaltje weinig voordelen te bieden.

Een belangrijk onderdeel van het ontwerp van een SPECT-systeem voor kleine dieren is de geometrie: hoeveel pinholes worden er gebruikt en waar worden ze precies geplaatst ten opzichte van het dier en de detector? Het is niet eenvoudig om een “optimaal” systeem te bedenken, omdat er vele parameters zijn die invloed hebben op het totale systeem en de meeste daarvan, zo niet alle, met elkaar verweven zijn. Het doen van *ray-tracing* of

zelfs *Monte Carlo* simulaties van complete systemen om de prestaties te optimaliseren, kan té tijdrovend worden omdat er zoveel verschillende situaties moeten worden gesimuleerd. **Hoofdstuk 5** presenteert een mathematisch model dat kan worden gebruikt om de verwachte prestaties, met betrekking tot resolutie en gevoeligheid van systemen met verschillende ontwerpparameters, snel met elkaar te vergelijken. Het model gaat ervan uit dat de multi-pinhole collimator en de detector beide de vorm hebben van een deel van een bolschil. Er worden analytische uitdrukkingen gebruikt voor de effectieve pinhole diameters, de gevoeligheid en de ruimtelijke resolutie. Voor een gegeven grootte van de *field-of-view* (het gebied dat door alle pinholes tegelijk gezien wordt), wordt steeds de pinhole diameter aangepast om de systeemresolutie van verschillende systemen met elkaar te vergelijken bij gelijke gevoeligheid en vice versa. Het model voorspelt dat de optimale resolutie en/of gevoeligheid wordt bereikt als de pinholes zo dicht mogelijk bij het dier worden geplaatst. Wanneer detectoren met een hoge resolutie beschikbaar komen, dan zou een verbetering in systeemresolutie van 30% mogelijk zijn, vergeleken met een geoptimaliseerd systeem dat een geometrie heeft zoals U-SPECT-I. Detectoren met een hoge resolutie kunnen dichtbij de collimator worden geplaatst zonder merkbare verliezen in systeemresolutie. Samen met detectoren met een hoge resolutie, kunnen systemen met pinholes met een fysieke diameter van 0 mm, waar alle gedetecteerde fotonen dus door de rand van de pinhole moeten gaan, een uitstekende systeemresolutie opleveren.

Bij multi-pinhole SPECT gaat de voorkeur uit naar iteratieve reconstructie-algoritmen boven analytische. Iteratieve methoden vereisen dat de positie-afhankelijke puntspreidingsfuncties (PSF's, tezamen ook bekend als "de systeemmatrix") bekend zijn. Deze specificeren de respons van de detectoren op een puntbron op elke positie in het instrument. Hoe nauwkeuriger de PSF tabellen het werkelijke systeem beschrijven, des te beter zullen de gereconstrueerde beelden de werkelijke verdeling van radioactiviteit weerspiegelen. Het puur empirisch meten van de PSF tabellen met een fysieke puntbron zou ideaal zijn in de zin dat de PSF's in dat geval de realiteit het best zouden beschrijven. Helaas is het, vanwege het enorm grote aantal meetposities, niet praktisch haalbaar om dit te doen voor systemen met een hoge resolutie. **Hoofdstuk 6** beschrijft de calibratiemethode die is ontwikkeld om de complete PSF tabellen voor de U-SPECT systemen te verkrijgen. Deze methode is gebaseerd op het generaliseren van een klein aantal eigenschappen van de puntbronresponsen of PSF's die worden opgenomen op een beperkt aantal meetposities, naar de hele meetruimte. De volledige vorm van de gemeten puntbronresponsies kan bijna worden behouden in de aangemaakte PSF-tabellen. Er wordt aangetoond dat met behulp van de op deze wijze gemaakte PSF-tabellen SPECT-reconstructies met een hoge resolutie kunnen worden gemaakt op het U-SPECT-I systeem. De gereconstrueerde resolutie, bepaald aan de hand van de zichtbaar-

heid van staafjes in een micro-capillairfantoom, is 0,45 mm met 0,6 mm pinholes, en onder de 0,35 mm met 0,3 mm pinholes. Hoofdstuk 6 laat ook zien dat verschillende benaderingen zoals de truncatie van de staart van de PSF's op verschillende diameter, resulteren in een aanzienlijke reductie van de reconstructietijd, terwijl nog steeds acceptabele reconstructies worden verkregen. Reconstructies van capillairfantomen, gebaseerd op verschillende acquisitietijden, leiden tot de conclusie dat de ruimtelijke resolutie van het U-SPECT-I systeem beneden 1 mm blijft, zelfs bij zeer korte acquisitietijden (rond een minuut).

Het eerste prototype SPECT-systeem voor kleine dieren dat is gebouwd in Utrecht, genaamd U-SPECT-I, wordt beschreven in **hoofdstuk 7**. Dit stationaire systeem kan de, voor het tomografisch afbeelden van de organen van een muis benodigde, projectiedata opnemen zonder dat daarbij de detectoren hoeven te bewegen. De met U-SPECT-I bereikbare resolutie en gevoeligheid worden gekarakteriseerd en er worden voorbeelden gegeven van metingen aan muizen. Met 0,6 mm pinholes, is de maximale fractie van detecteerbare fotonen die door een puntbron zijn uitgezonden (de piekgevoeligdheid), 0,22% en de gevoeligheid blijft boven 0,12% in de middelste 12 mm van het centrale vlak. De gereconstrueerde resolutie, bepaald aan de hand van de zichtbaarheid van staafjes in een micro-capillairfantoom, is $<$ 0,5 mm. Beelden van de wervelkolom van een muis laten de opname van Tc-99m-hydroxy-methyleendifosfonaat zien tot op het niveau van kleine onderdelen van de uitsteeksels van de wervels. Deze worden duidelijk onderscheiden van het wervelgat en de openingen tussen de wervels. Met een andere *tracer*, kan de perfusie van het myocard in de wanden van de linker- en rechterventrikels, en zelfs in structuren zo klein als de papillairspieren, worden gevolgd. U-SPECT-I kan de concentraties van moleculen in aangrenzende volumina ter grootte van 0,1 micro-liter onderscheiden, aanmerkelijk kleiner dan enig eerder SPECT- of PET-systeem.

Een tweede generatie van het systeem, genaamd U-SPECT-II, wordt beschreven in **hoofdstuk 8**. U-SPECT-II kan zowel voor het afbeelden van muizen als ratten worden gebruikt. Het detectoroppervlak is significant groter dan dat van U-SPECT-I en de detectoren hebben volledig digitale elektronica. Gegevens worden uitgelezen in *list mode* (de positie en energie van elk afzonderlijk gedetecteerd foton worden opgeslagen), hetgeen flexibiliteit oplevert in het kiezen van energie *windows* en het simultaan meten met meerdere isotopen. Dankzij deze manier van gegevens uitlezen kunnen ook *gated* opnamen worden gemaakt, dat wil zeggen dat de reconstructie kan worden uitgesplitst naar de fase van bijvoorbeeld de hart- of ademhalings-cyclus, zodat bewegingsartefacten worden verminderd. Bovendien heeft U-SPECT-II een geautomatiseerd proces om de de *field-of-view* uit te breiden, zodat ook opnamen van een gehele muis of rat gemaakt kunnen worden. Op de grafische gebruikersinterface kan de gebruiker aangeven welk deel van het dier gescand dient te worden. In hoofdstuk 8 worden het ontwerp, de ontwikkeling en een eerste serie metingen beschreven en worden de

prestaties in kaart gebracht en gedemonstreerd. De gereconstrueerde resolutie (bepaald aan de hand van de zichtbaarheid van staafjes in een micro-capillairfantoom), is 0,35 mm met de 0,35 mm pinhole muizencollimator, 0,45 mm met de 0,6 mm pinhole muizencollimator en 0,8 mm met de 1,0 mm pinhole rattencollimator. De geometrische gevoeligheid met de 0,35 mm pinholes (muis) is 0,07%, met de 0,6 mm pinholes (muis) 0,18% en met de 1,0 mm pinholes (rat) 0,09%. Met U-SPECT-II kunnen de concentraties van moleculen in aangrenzende volumina tot 0,04 microliter (muis) en 0,5 microliter (rat) worden onderscheiden. Onze eerste *in vivo* brein- en bot-scans met verschillende doses laten zien dat U-SPECT-II kan worden gebruikt voor nieuwe toepassingen in het bestuderen van dynamische biologische systemen en (radioactieve) farmaca. De gebruikersvriendelijke grafische interface en nieuwe mogelijkheden maken het tot een veelzijdig systeem om *molecular imaging* mee te bedrijven.

Dankwoord

Een proefschrift en zeker het werk wat erin beschreven staat, is het resultaat van de inzet van veel verschillende mensen. Ik kan niet iedereen bij naam noemen. In het kort komt het neer op: iedereen die in het groot of in het klein heeft bijgedragen aan dit onderzoek, bedankt!

De ontwikkeling van de U-SPECT was team-werk. Dit avontuur begon met de bouw van de U-SPECT-I, waar ik samen met Brendan Vastenhouw en mijn promotor prof. Freek "allesziener voor de wetenschap" Beekman zo intensief aan werkte. Markante momenten in de vroege U-SPECT ontwikkeling waren wat mij betreft het maken van schetsen op het vliegveld van Minneapolis en het gieten van loden afschermingsdelen in Freeks keuken; en natuurlijk de resultaten van de eerste beeldreconstructies. Freek, ik heb veel geleerd in de paar jaar dat ik in je groep rondloop. Dank voor de mogelijkheden die ik in die tijd heb gekregen. Jij bent iemand met meer ideeën dan een groep van 14 mensen uit kan voeren (ik ben erg benieuwd of dat blijft gelden voor een nog grotere groep in Delft) en het ontbrak daarbij niet aan financiën. En je verliest naast het harde werken de mensen in je groep niet uit het oog. En ook zonder de inzet van Brendan, variërend van voorbereidingen op scans ("nog even één ding checken") en snelle reparatie-acties tijdens diezelfde scans ("helemaal top, niets meer aan doen") tot het uitgebreide en lastige programmeerwerk dat komt kijken bij de software, was het in elk geval geen succes geworden. Veel dank daarvoor!

Hierbij bedank ik ook mijn andere promotor, prof. Max Viergever. Max, ik heb met veel plezier en zonder problemen bij het Image Sciences Institute gewerkt, omdat daar alles onder jouw leiding goed georganiseerd is. Dank ook voor de hulp in de laaste fase bij het maken van het proefschrift.

De mensen van de groep van Freek: Gerralt, Auke-Pieter, Brendan, Marcia, Renée, Wojtek, Jianbin, Sebastiaan, Peter (Kumpel!), Tim, Mart, Matthieu, Steven, Jan, Cynthia, Norbert, Eelco, Woutjan, Marc, Roger, Paul, Chao, Anne-marie, Ellis, Mariëtte, Samira: dank voor jullie collegialiteit, samenwerking en gezelligheid naast het werk. Het wordt weer tijd voor een groeps-etentje…

De afdeling Farmacologie en Anatomie, tegenwoordig Neurowetenschappen en Farmacologie, bedankt voor de leuke werk-omgeving die ik op jullie afdeling heb gehad en bedankt voor alle activiteiten naast het werk, zoals vele borrels, labdagen, Sinterklaasvieringen, paaslunches. En inhoudelijk hebben we ook samengewerkt: in het bijzonder bedank ik Annemarie voor het regelen en uitvoeren van de biotechnische kant van onze scans, waarbij we soms record-werktijden haalden. Jan Brakkee, bedankt voor het opzetten van een dierstal bij de U-SPECT (hij wordt eindelijk gebruikt) en voor handige tips en praktische ondersteuning.

Bij de afdeling Nucleaire Geneeskunde speciaal dank voor de analisten en later MNW-ers van de radionuclidenapotheek voor het maken van standaard en soms wat minder standaard spuiten en epjes. En Oane, Fred, Remmert en anderen die in het lab werken, dank voor hulp bij het werken met activiteit en het gebruikt van het B-lab om puntbronnen te maken.

De Instrumentele Dienst, Medische Technologie met of zonder Multimedia en/of klinische fysica: kan ik niet beter “Kees Ligtvoet & co” zeggen? Zowel de mensen bij mechanica als bij electronica ontwikkeling, dank voor het meedenken, ontwerpen, bestellen en maken van allerlei grote en kleine onderdelen van het U-SPECT systeem.

Gijs van der Wilt, Gijs Ockeloen en Willem ter Kuile: dank voor jullie bijdragen aan het design en het maken van belangrijke onderdelen van de binnen- en buitenkant van de U-SPECT.

Herr Stockmann, Herr Osiek, und Herr Staubach (Inter Medical) und Professor Krah: vielen Dank. Thank you for your support and collaboration to get our detectors ready for production use.

Fons, Henk, Richard en in het bijzonder Huub, bedankt voor het ondersteunende werk om het doen van radioactieve experimenten in het Stratenum mogelijk te maken.

Freek en Carmen, dank voor het opzetten van de business-kant van MILabs. Ik had bij het begin van de ontwikkeling van de U-SPECT-I niet gedacht dat ik iets meer dan drie jaar later ook voor een bedrijf zou werken dat de U-SPECT-II al op de markt zou brengen. ’t Is allemaal best snel gegaan als ik nu terugkijk.

Mart, dank voor LaTeX-hulp bij het maken van dit proefschrift. En voor het aanvoeren van bulk-hoeveelheden pepernoten en paaseitjes… Straks krijgen we de noodzaak tot invoering van een “balans maand” tussen het sinterklaas- en paaseitjes-seizoen.

Peter en Brendan, dank dat jullie mijn paranimfen willen zijn en Brendan dank voor het renderen van de plaatjes voor het omslag. Tenslotte wil ik mijn ouders ervoor danken dat ze me altijd gesteund hebben en dat ik altijd bij hen terecht kon.

Publications

International journals:

- F van der Have and F J Beekman, Photon penetration and scatter in micro-pinhole imaging: a Monte Carlo investigation, *Phys. Med. Biol.* 2004; 49: 1369–1386.
- G A de Vree, A H Westra, I Moody, F van der Have, C M Ligtvoet, and F J Beekman, Photon-Counting Gamma Camera based on an Electron-multiplying CCD, *IEEE Trans. Nucl. Sci.* 2005; 52(3): 580–588.
- F J Beekman, F van der Have, B Vastenhouw, A J A van der Linden, P P van Rijk, J P H Burbach, and M P Smidt, U-SPECT-I: A Novel System for Submillimeter-Resolution Tomography with Radiolabeled Molecules in Mice, *J. Nucl. Med.* 2005; 46(7): 1194–1200.
- F van der Have and F J Beekman, Penetration, Scatter and Sensitivity in Channel Micro-pinholes for SPECT: a Monte Carlo investigation, *IEEE Trans. Nucl. Sci.* 2006; 53(5): 2635–2645.
- F J Beekman and F van der Have, The Pinhole: Gateway to Ultra-high Resolution Three-Dimensional Radio-Nuclide Imaging, *Eur. J. Nucl. Med. Mol. Im.* 2007; 34(2): 151–161.
- M C M Rentmeester, F van der Have, and F J Beekman, Optimizing multi-pinhole SPECT geometries using an analytical model, *Phys. Med. Biol.* 2007; 52(9): 2567–2581.
- B Vastenhouw, F van der Have, A J A van der Linden, L von Oerthel, J Booij, J P H Burbach, M P Smidt, and F J Beekman, Movies of dopamine transporter occpancy with ultra-high resolution focusing pinhole SPECT, *Mol. Psych.* 2007 (accepted).
- F van der Have, B Vastenhouw, M C M Rentmeester, and F J Beekman, System Calibration and Statistical Image Reconstruction for Stationary Pinhole SPECT systems, *IEEE Trans. Med. Imaging.* (submitted)
- B Vastenhouw, F van der Have, A J A van der Linden, L von Oerthel, J Booij, J P H Burbach, M P Smidt, and F J Beekman, Movies of dopamine transporter occupancy with ultra-high resolution focusing pinhole SPECT, *Mol Psych* 2007 (accepted).
- F van der Have, B Vastenhouw, A J A van der Linden, J O Krah, and F J Beekman, Design and initial performance of U-SPECT-II (in preparation).

Conference proceedings:

- F van der Have and F J Beekman, Characterisation of photon penetration and scatter in Pb, W, Au and Pt micro pinholes, *IEEE Nuclear Science Symposium Conference Record*; 2003: M10-262.
- F J Beekman, B Vastenhouw, F van der Have, Towards 3D Nuclear Microscopy using locally focusing many-pinhole SPECT, *Proceedings of the 2003 International Meeting on Fully Three-Dimensional Image Reconstruction in Radiology and Nuclear Medicine*; 2004.
- G A de Vree, A H Westra, I Moody, F van der Have, F J Beekman, Electronics for a Photon-counting Gamma Camera based on an Electron-multiplying CCD, *IEEE MIC Conference Record*; 2004.
- G A de Vree, F van der Have, F J Beekman, EMCCD-based Photon-counting mini Gamma Camera with a Spatial Resolution $<$ 100 mm, *IEEE MIC Conference Record*; 2004.
- M C M Rentmeester, F van der Have, F J Beekman, Continuous Model of Multi-Pinhole SPECT Devices, *Conference Record of the 2005 IEEE Nuclear Science Symposium and Medical Imaging Conference* 2005; M03-283.
- F van der Have, B Vastenhouw, M C M Rentmeester, F J Beekman, System Calibration and Statistical Image Reconstruction for Sub-mm Stationary Pinhole SPECT, *Conference Record of IEEE 2005 Nuclear Science Symposium and Medical Imaging Conference* 2005; M11-291.

Curriculum Vitae

Frans van der Have werd geboren op 13 december 1977 in Ede. Hij bracht zijn jeugd door in Ede en ging vanaf 1990 naar de christelijke scholengemeenschap “Het Streek” in Ede, waar hij in 1996 zijn gymnasiumdiploma behaalde. In augustus 1996 begon hij aan de studie Technische Natuurkunde aan de Universiteit Twente. Tijdens die studie werd zijn belangstelling voor het doen van biofysisch en biomedisch onderzoek steeds groter. De wetenschappelijke stage voor zijn studie heeft hij ingevuld met het door middel van ellipsometrie onderzoek doen naar de mogelijkheden om moleculen (bijvoorbeeld medicijnen) te adsorberen aan en gecontroleerd los te laten van een poreus silicium oppervlak. Het stage-onderzoek vond plaats aan de universiteit van Linköping (Zweden). De keuze voor de afstudeervakgroep Biofysische Technieken lag ook in de lijn van het toepassen van optische technieken in biofysisch onderzoek. In het afstudeeronderzoek werd een fluorescentiemicroscoop ontworpen en ingebouwd in een bestaande opstelling met een optisch pincet en een methode ontwikkeld om nauwkeurig de positie van een fluorescente bead te kunnen volgen. Na het afronden van de studie Technische Natuurkunde in 2002, werd in januari 2003 begonnen bij de afdeling Nucleaire Geneeskunde en het Image Sciences Institute van het UMC Utrecht aan het onderzoek dat is beschreven in dit proefschrift.

Appendix: Color figures

a  b 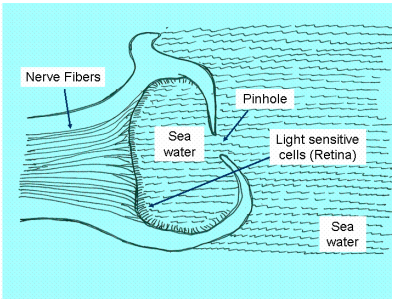

Figure 2.1. The *Nautilus Pompilius* (a, image courtesy of Artis Zoo, Amsterdam) with pinhole eyes (b).

a 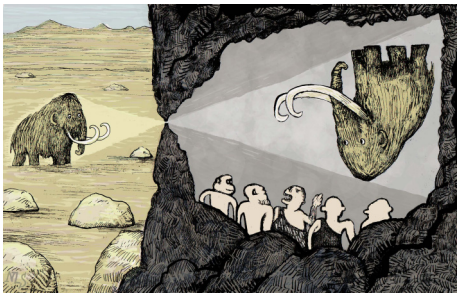 b 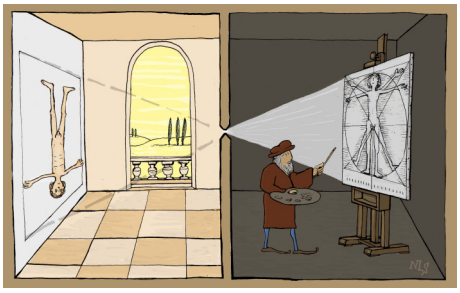

Figure 2.2.a) An artist's impression of possible early pinhole imaging: the film-less movie theatre was born when surrealistic "upside down movies" were displayed on the wall of a cave. b) Was this how Leonardo painted the Vitruvian Man? A trade-off between "patient" discomfort and artist discomfort could be found by changing the angular position of the model. Illustrations by Niels de Hoog.

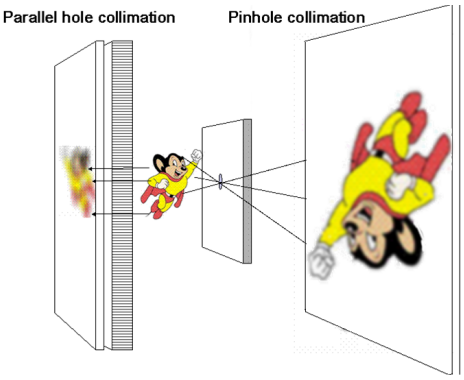

Figure 2.3. With parallel hole collimation (*left*) image resolution can be degraded significantly due to intrinsic camera blurring. With pinhole imaging (*right side of the mouse*), magnification of the projection suppresses information loss that is due to intrinsic camera blurring.

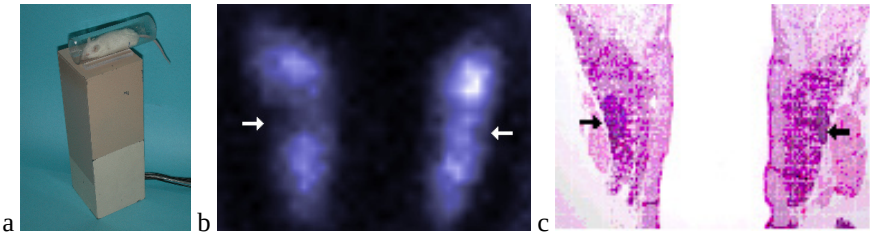

Figure 2.5. (a) Desktop mouse pinhole imaging system. b) I-125 scan of a mouse thyroid provides details of a few hundred micrometers such as the parathyroid gland which does not take up any iodine (arrows, also shown in frame c). (from [20])

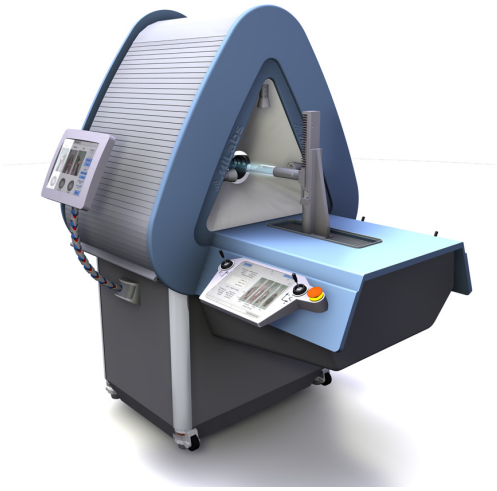

Figure 2.7. The U-SPECT-II system based on ultra-large NaI detectors and interchangeable collimator tubes.

a 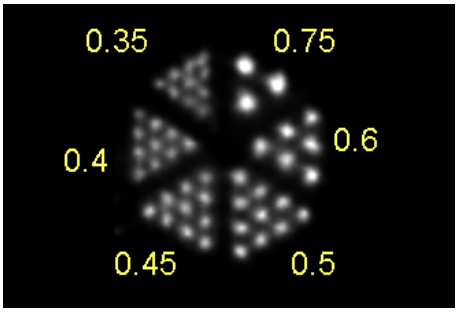

b 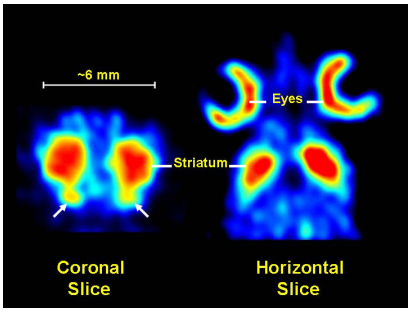

Figure 2.8. U-SPECT images; Frame a) Derenzo resolution phantom image obtained with U-SPECT (0.3 mm pinholes) shows a section with 0.35 mm capillaries clearly separated. Frame b) Two mutual perpendicular cross-sections of a 3D sub-mm resolution FP-CIT image of the distribution of dopamine transporters in a mouse head obtained with U-SPECT-I fitted with 0.6 mm pinholes. Dynamics of tracer concentrations in tiny structures in sub-compartments of mouse organs such as the Olfactory Tubercle (arrows) and the retina can be monitored.

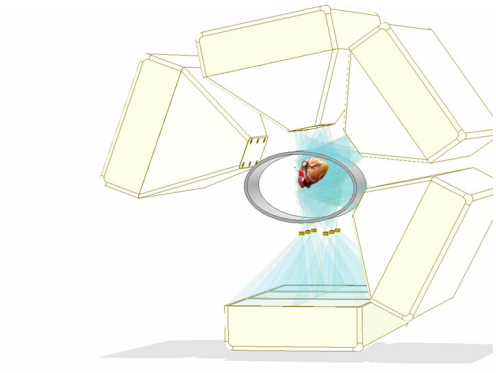

Figure 2.9. Cardiac SPECT system model with pinholes focusing to the heart. In the picture the shielding was removed from one multi-pinhole collimator to show how the heart is projected onto the detector without overlap. Means to avoid projection overlap (baffles) are not shown. This system has a significantly better resolution-sensitivity trade-off than a dual head parallel-hole SPECT system.

Figure 4.1. Cylindrical collimator of the U-SPECT-I system, equipped with 75 gold micro-pinholes with an acceptance angle of 30 °.

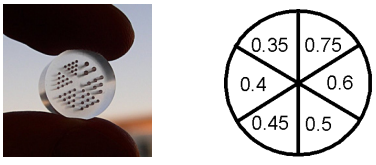

Figure 6.7. Photograph and drawing of the capillary hot rod phantom used in the experiments. The minimum distance between capillaries is equal to the diameter. Capillary sizes of this phantom range from 0.35 to 0.75 mm.

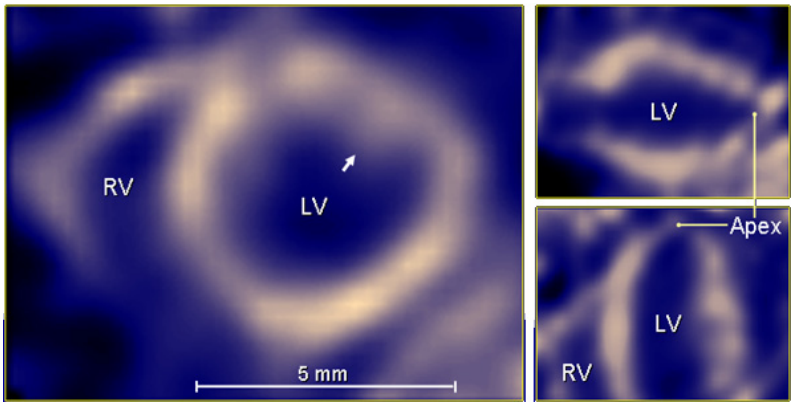

Figure 7.5. Mutual perpendicular cross sections through submillimeter- resolution 3-dimensional myocardial perfusion image volume of living mouse (named Animal Co-Image of the Year at the annual meeting of the Society of Nuclear Medicine, Philadelphia, 2004). Image data were acquired during 30 min, starting 30 min after administration of 222 MBq (6 mCi) of Tc-99m-tetrofosmin. On left is a short-axis slice showing myocardial perfusion in right ventricular (RV) and left ventricular (LV) walls. Perfusion in anterior papillary muscle (arrow) can be distinguished from other parts of left ventricular wall. At top right is a vertical long-axis slice; at bottom right, a horizontal long-axis slice.

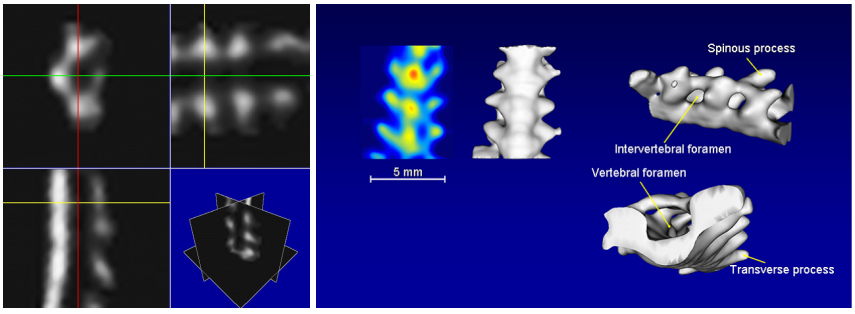

Figure 7.6. Different representations of reconstructed image volume of lumbar spine, acquired during 22 min, 2 h after injection of 148 MBq (4 mCi) of Tc-99m-HDP. (A) Three different orthogonal cross sections. (B) Projection of local image maxima (far left) and 3 isosurface renderings of tracer concentrations in same spinal section (named Animal Co-Image of the Year at the annual meeting of the Society of Nuclear Medicine, Philadelphia, 2004)

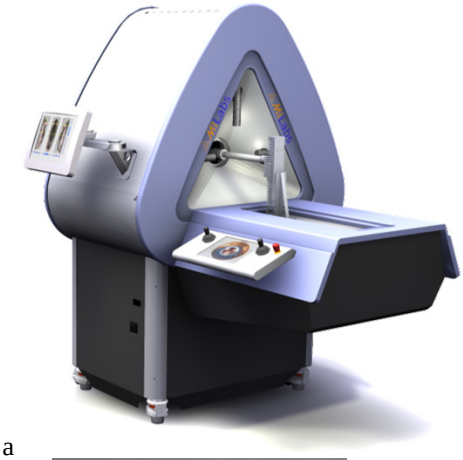

a

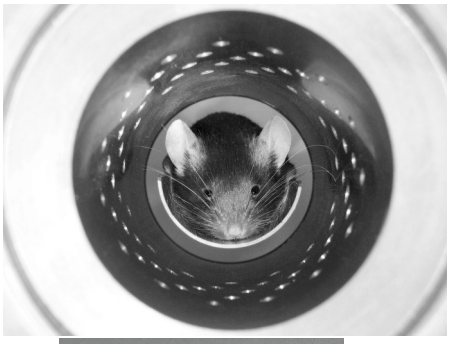

b

c

d

Figure 8.1. a) The U-SPECT-II system. b) The collimator tube surrounding a mouse. c) The mouse collimator and shielding tube. d) The rat collimator and shielding tube. The different tubes as shown in frames c) and d) can be exchanged easily from the posterior of the system.

a  b 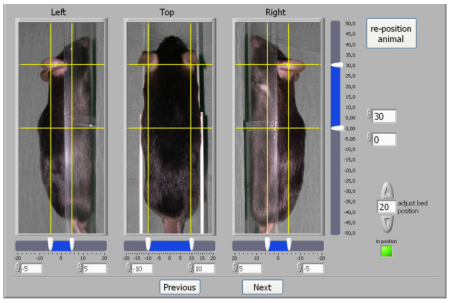

Figure 8.3. a) Mouse observed with three optical cameras for region-of-interest selection. b) User interface allows to select the volume to be scanned.

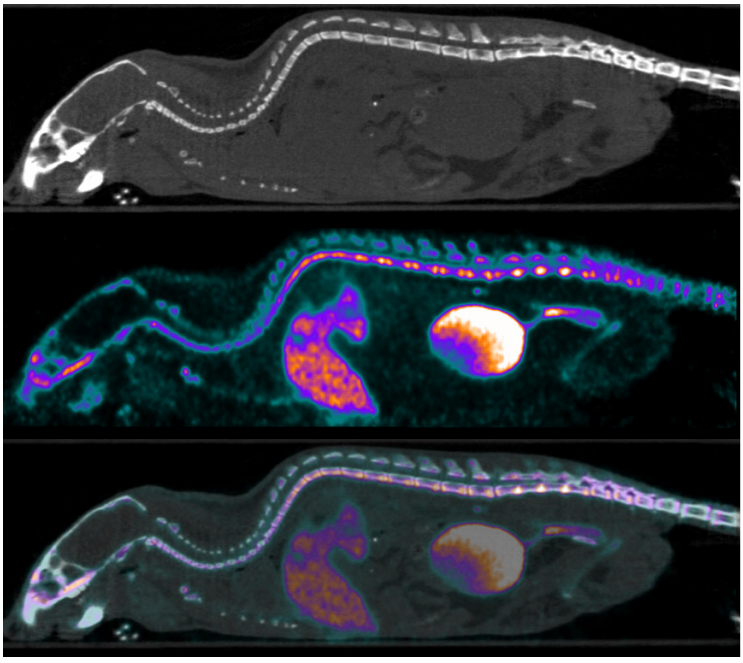

Figure 8.6. SPECT-CT saggital slice of a mouse. Top: CT only, middle: SPECT only, bottom: SPECT-CT fused. SPECT was a ^{99m}Tc-HDP bone scan on the U-SPECT-II system. Registration was done by the method of Chow et al.

a 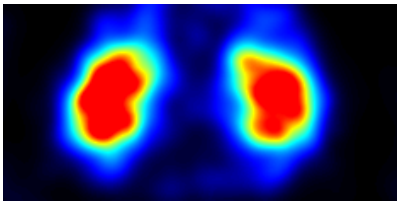 b 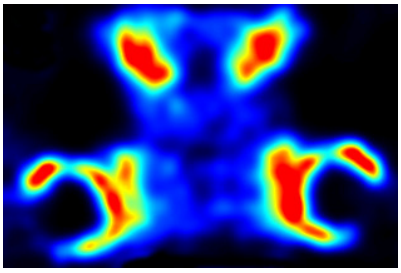

Figure 8.8. Mouse dopamine transporter study showing a coronal slice (a) through the striatum and a horizontal slice (b) through the striatum and eyes.